MICROSTRUCTURAL EVOLUTION OF EPITAXIAL DIELECTRIC FILMS DERIVED FROM CHEMICAL PRECURSORS

by

Man Fai Ng

B.S., Materials Science and Engineering
University of California, Berkeley, 1988

S.M., Ceramics
Massachusetts Institute of Technology, 1990

Submitted to the Department of Materials Science and Engineering in
Partial Fulfillment of the Requirements for the Degree of

Doctor of Philosophy
in Materials Science and Engineering

at the

Massachusetts Institute of Technology

February 1995

Signature of Author.....
Department of Materials Science and Engineering
January 13, 1995

Certified by.....
Michael J. Cima
Norton Associate Professor of Ceramics
Thesis Supervisor

Accepted by.....
Carl V. Thompson II
Professor of Electronic Materials
Chair, Departmental Committee on Graduate Students

ABSTRACT

MICROSTRUCTURAL EVOLUTION OF EPITAXIAL DIELECTRIC FILMS DERIVED FROM CHEMICAL PRECURSORS

by

Man Fai Ng

Submitted to the Department of Materials Science and Engineering
on January 13, 1995
in Partial Fulfillment of the Requirements for the Degree of
Doctor of Philosophy

This study examines epitaxial lanthanum aluminate ($LaAlO_3$) and magnesium aluminate ($MgAl_2O_4$) thin films deposition on single-crystal substrates by a spin-on process. These films are candidates as dielectric layers for $Ba_2YCu_3O_{7-x}$ (BYC) superconductor thin film devices. Film fabrication was by pyrolysis of spin-on chemical precursors. Mixed metal nitrates were used for both the $LaAlO_3$ and $MgAl_2O_4$ films. Magnesium aluminum isopropoxide was also used for the $MgAl_2O_4$ films.

The precursors first decompose into an amorphous mixture. Heterogeneous nucleation occurs on the lattice-matched single-crystal substrates. The epitaxial films grow upward and consume the amorphous regions. The crystallization temperature of both $LaAlO_3$ and $MgAl_2O_4$ are lower for thin films than for bulk samples due to the substrate seeding. The transformation of $LaAlO_3$ is not linear growth as in typical homoepitaxy. The Johnson-Mehl-Avrami exponent of growth is between 1.4 to 1.5. This deviation from the linear growth model (n = 1) can be attributed to continuous nucleation on the substrate/film interface. The transformation activation energy for $LaAlO_3$ on $SrTiO_3$ is approximately 5.1 eV.

The films are epitaxial without any second phase. The nitrates-derived $MgAl_2O_4$ films have similar qualities as those derived from magnesium aluminum isopropoxide. TEM micrographs show that all of these films have faceted pores with sizes ranging from 5 to 30 nm. Grain boundaries are not observed. Selected area diffraction shows that they are single-crystal-like despite the porosity. All of these films are smooth and crack-free. The average surface roughness is < 1 nm. Study of the processing conditions leads to a novel approach of using a humid pyrolysis atmosphere to eliminate crack formation in nitrates-derived $MgAl_2O_4$ films.

BYC films have been deposited on the epitaxial $LaAlO_3$ films. The resultant films have $T_c > 92$ K and $J_c(77K) > 2 \times 10^6$ A/cm^2 at zero magnetic field. Until this study, there is not any chemically derived films with qualities good enough for subsequent epitaxial BYC deposition. These $LaAlO_3$ and $MgAl_2O_4$ films also show the potential to epitaxially planarize trenched substrates.

Thesis Supervisor: Professor Michael J. Cima
Title: Norton Associate Professor of Ceramics

TABLE OF CONTENTS

LIST OF FIGURES

Chapter 2

Chapter 3

Chapter 4

Chapter 5

Chapter 6

Chapter 7

Appendix C

LIST OF TABLES

Chapter 1

Chapter 3

Chapter 6

Appendix A

Appendix B

ACKNOWLEDGMENTS

First, I would like to express my gratitude to Prof. Michael Cima for his guidance and support throughout the entire course of this work. I also thank Prof. Samuel Allen and Prof. Donald Sadoway to be in my thesis committee. In addition, Prof. Manuel Oliveria has served as a member of my committee prior to his departure from MIT. Prof. Ken Russell provided me valuable insight.

I acknowledge the financial support from E-Systems Corporation and Advanced Research Projects Agency for this work.

Many people in the CPRL have helped me tremendously. Simone Peterson cheerfully encouraged and helped me. Paul McIntyre imparted me his wisdom in MOD process and TEM sample preparation. Jack Smith, who always come up with better ways to tackle problems, taught me how to look at things in different perspectives. Bertha Chang never refused my requests for help, no matter how time-consuming the tasks were or how busy she was. Lenny Rigione, who was always willing to give a helping hand in any situation, made life easy in the lab. John Centorino made the laboratory ran smoothly. Barbara Layne patiently handled all the paperwork I created. Wendell Rhine provided me with valuable advice in chemistry. Zhiping Jiang's chemistry expertise and Neville Sonnenberg's computer expertise smoothed the way. Kevin Ressler assisted me in the spectrophotometry study. I will always remember the wonderful people I met in the CPRL.

Others who have made my six years graduate study at MIT enjoyable include Jennifer Lewis, Raymond Chiu, Anne Hardy, Shiaoming Chu, Yuying Tang, Hidehiro Endo, Anacleto de Figueredo, Sabtir Khanuja, Jaedeok Yoo, Matt Galla, Tae-hyun Sung,....the list goes on and on.

People in other laboratories and facilities assisted me in many ways: Libby Shaw and the late John Martin Surface Analytical Facility, Mike Frongillo in the TEM Facility; Joe Adario and Peter Klouman in the X-ray Facility, and Rich Perilli and Tim McClure in the Microelectronic Facility.

I also thank many who offered their prayer support and friendship throughout my graduate study.

I thank my mom and my late father for everything. They have let me choose my own path and never put any pressure on me.

Finally, I praise God for He is my refuge and strength, an ever-present help in trouble.

CHAPTER 1
INTRODUCTION

1.1 TECHNOLOGICAL IMPORTANCE

Production of practical high temperature superconductor (HTSC) multichip modules (MCM) requires both high quality superconductor and dielectric films. One of the requirements for the high temperature superconductor films is the capability to carry high current densities ($> 10^6$ A/cm^2). Only epitaxial high temperature superconductor films have so far demonstrated the capability to carry such high current densities. This limitation on the film microstructure requires the underlying dielectric films to be epitaxially deposited also in order for the subsequent superconductor films to grow epitaxially. This constrains the dielectric films to be lattice-matched. Epitaxial films of $Ba_2YCu_3O_{7-x}$ (BYC), one of the HTSC materials, have been routinely reported to carry critical current densities over 1 x 10^6 A/cm^2 at 77 K. The dielectric materials used for BYC devices must be lattice-matched to the a-axis of BYC crystals because typical BYC epitaxial films are c-axis oriented. Practical devices also require that these dielectric layers to have low dielectric constant and low dielectric losses. Cubic dielectric materials are preferable because of their isotropic dielectric properties. Finally, the dielectric materials must be chemically inert with respect to BYC during high temperature processing. These constraints limit the number of dielectric materials choices. Table 1.1 is a list of potential dielectric materials for BYC devices.

Two promising materials for dielectric layers are lanthanum aluminate ($LaAlO_3$) and $MgAl_2O_4$ (magnesium aluminate, or commonly referred to as spinel). $LaAlO_3$ has a dielectric constant of 23. The lattice mismatch between (100) $LaAlO_3$ and (100) BYC is only 2%. High quality BYC films have routinely been deposited on single-crystal (100) $LaAlO_3$ (Hwang, 1989; Koren, 1989; Xiong, 1989; Siegel, 1990). The other candidate, $MgAl_2O_4$, has a low dielectric constant of 8.3. The lattice mismatch between (100) $MgAl_2O_4$ and (100) BYC is about 5.6%. Spinel has been shown to react with BYC at high temperatures. It is, however, possible to take advantage of spinel's low dielectric constant by inserting another barrier layer between spinel and BYC. Therefore, it is worthwhile to investigate the deposition of epitaxial films of (100) $MgAl_2O_4$ and (100) $LaAlO_3$.

This study uses pyrolysis of spin-on liquid precursors to deposit epitaxial $MgAl_2O_4$ and $LaAlO_3$ films. This method offers several advantages over other prevalent vapor

deposition methods. It is demonstrated in this work that high quality spinel and lanthanum aluminate epitaxial films can be deposited by the spin-on method. These films have smooth surfaces and single-crystal-like qualities. Both magnesium aluminum isopropoxide ($Mg[Al(OC_3H_7)_4]_2$) precursor and mixed magnesium-aluminum nitrate precursor are used for $MgAl_2O_4$ thin films deposition. Mixed lanthanum-aluminum nitrate precursor is used for depositing epitaxial $LaAlO_3$ films.

Table 1.1 Potential Dielectric Materials and Their Physical Constants

Material	dielectric constant	mismatch with BYC*
$LaAlO_3$ (perovskite)	23	-2.2%
$LaGaO_3$	25	1.5
$NdGaO_3$	20.2	-1.3
Y-ZrO_2 (110)	27.5	-8.2
$CaNdAlO_4$	20	5.1
MgO	9.6	9.2
$MgAl_2O_4$	8.3	-5.3
$SrTiO_3$	277	2.0
CeO_2 (110)	25	1.4

*The a-axis lattice parameter of BYC is different from that of the b-axis. In addition, some dielectric materials do not have cubic structure. The larger values for the lattice mismatch are listed in this table.

Data are compiled from Giess *et al.*, 1990; and Berkowski *et al.*, 1990.

1.2 SCIENTIFIC IMPORTANCE

This study also addresses some scientific issues in pyrolysis of chemical precursors for thin films. Until this study, all spin-on techniques for multi-cation oxide film depositions have used precursors with complicated molecular structures or by the sol-gel method. The prevalent thinking is that only precursors with molecular structures which link together the different metal cations can preserve the stoichiometry at the molecular level during decomposition and oxide formation. Examples of these precursors are alkoxides-based and other sol-gel precursors. Mixed metal salts, because of their different solubilities and decomposition temperatures/rates, are believed to lead

to local cationic segregation. This perception, however, has not been adequately tested in thin films. It may be advantageous in many cases to use precursors such as mixed metal salts. This study demonstrates that mixed metal salt precursors can produce multi-cation oxide films with qualities similar to those derived from alkoxide precursors.

There is little literature available on heteroepitaxial growth of multi-cation ceramics from amorphous materials despite the increased awareness of spin-on or other *ex situ* deposition methods. Kinetic data of heteroepitaxial growth are particularly scarce. The other area that deserves attention is the porosity due to the inevitable volume change during pyrolysis on epitaxial growth. These issues are examined in this work.

The materials chosen for this study, spinel and $LaAlO_3$, are good candidates to study multi-cation oxide heteroepitaxy. They are cubic systems, which simplify the study. ($LaAlO_3$ is cubic above 500°C.) They also belong to spinel and perovskite structures, to which many important electroceramics belong. The approach is to examine the microstructures of the decomposed product before and during epitaxial growth to determine the mechanism. The kinetics of epitaxial growth is also studied. The understanding gained in this work can lead to deposition of other epitaxial films by similar spin-on techniques as well as insight in solid-phase heteroepitaxy.

1.3 SCOPE AND ORGANIZATION OF THESIS

This thesis is a processing study which tries to cover the major aspects of the film deposition: from decomposition of precursors to epitaxial growth to final film microstructures and performance. The topic of spin-on spinel and lanthanum aluminate thin films derived from nitrates and alkoxides itself is a broad subject. It cannot be covered comprehensively in one thesis. Mixed nitrate precursors are the main focus of this study because this is the first time that the spin-on approach using nitrate precursors has demonstrated the capability to deposit epitaxial multi-cation oxide films. More effort is devoted to $LaAlO_3$ films in this study because lanthanum aluminate substrate has been used extensively as substrate material for BYC. Less emphasis is on the alkoxide-derived thin films because other researchers have made headway in this area. Films from magnesium aluminum isopropoxide precursor are used in this study mainly to compare with those from magnesium-aluminum nitrate precursor. There is no double alkoxide precursor route for $LaAlO_3$ films because a double metal alkoxide of lanthanum-aluminum does not provide the desired cationic ratio.

The thesis is divided into eight short chapters because of the broad range of topics addressed in this work. The background literature is reviewed in Chapter 2. The background information on barium yttrium cuprate, magnesium aluminate spinel, and lanthanum aluminate is first introduced. Various methods of $LaAlO_3$ and spinel thin films deposition are reviewed. Nitrates and alkoxides as precursors are discussed. There is also a brief review of the different mechanisms in solid-phase heteroepitaxy.

Chapter 3 concentrates on the chemistry of decomposition of the different precursors prior to the formation of the epitaxial phase. All three precursor systems are examined. Data from experiments either supplement or verify the available information from literature. This chapter mainly provides the necessary information for the chapters in surface properties and in epitaxial growth.

Chapter 4 concentrates on the surface features of the chemically derived films. Processing conditions that are influential to the surface properties are discussed. A novel approach of using a humid pyrolysis atmosphere to eliminate cracking is discussed.

Chapter 5 discusses the crystallographic properties of the films. The orientation and the porosity of these films are examined. The qualities of spinel films made from nitrates and from alkoxides are compared.

Chapter 6 discusses the epitaxial growth process itself. The mechanism and the kinetics of the film growth on lattice-matched substrates are the main focus. The effect of heterogeneous nucleation is discussed.

Chapter 7 covers the application aspects of this spin-on technique in multichip modules. The viability of using these spin-on films in epitaxial planarization on trenched substrates and as underlying dielectric layers for BYC films is addressed.

Chapter 8 concludes the thesis and suggests direction for future work.

Appendices A and B list the manufacturers/suppliers of the equipment and supplies used. Appendix C discusses the theories and calculations for the index for refraction and density measurement of the spinel films.

CHAPTER 2
BACKGROUND

2.1 MULTICHIP MODULES

The continuous drive for higher performance in electronic devices calls for improvement in microelectronic designs. The design of the microelectronic packaging is often as important as the design of the integrated circuitry (IC) chips in determining the performance of a device. Microelectronic packaging provides a suitable, protective operating environment for the chips. It allows signals to be transmitted from and to different chips and devices. It distributes electric power and dissipates the heat generated by the chips. There are typically three levels of packaging in a typical vintage early 1980's mainframe computer. Individual IC chips are housed in a chip carrier. The chip carriers and other components are bonded to a printed-circuit card. Many cards are mounted on a larger printed circuit board.

Multichip module (MCM) is an emerging packaging technology that offers several advantages over conventional packaging assemblies. A multichip module is a subassembly which contains more than one chip. A simple two-dimensional multichip module is illustrated in Fig. 2.1. The MCM design is complicated, but it allows short interconnect paths and high circuitry density. It is possible to use MCM to hold many IC chips and thus eliminates the printed circuit card level.

The drive for miniaturization in MCM also pushes for more and more circuits in a given region. The cross sectional area of interconnects decreases as the number density of interconnects increases. Normal metal conductors used in interconnects can lead to signal losses. For an interconnect line with diameter d, the resistance R_{dc} varies with $1/d^2$ at low frequencies; the resistance R_{ac} varies with $1/d$ at high frequencies. The characteristic impedance Z_o of a conductor trace can be expressed as

$$Z_o = \sqrt{\frac{R + i\omega L}{G + i\omega C}} \text{ ohm} \tag{2.1}$$

where R is the resistance; G is the conductance; L is the inductance; C is the capacitance of the conductor; and ω is the angular frequency. High resistance increases the impedance of the trace. Signal degradation occurs when the impedance of the trace does not match that of the output (typically 50 Ω).

Superconductors can be used as interconnect materials because the R_{dc} is zero and the R_{ac} values are very low. Superconductors can reduce the number of interconnection layers. Other advantages of superconductor include reduction in forward wave crosstalk between adjacent lines with the use of a superconductor ground plane (Kroger, 1989). It is possible to achieve interconnect densities of up to 10^4 inches/in^2 for a simple superconductor MCM.

A BYC MCM requires dielectric layers which serve the purpose of insulating the different superconductor layers and prevent cross-talk. There are many requirements, besides lattice-matching with BYC, for the dielectric layers in MCM. The materials should have low dielectric constant and loss, low electrical conductivity, high dielectric strength, good mechanical strength, and compatibility with BYC. The deposited films must be smooth, uniformly thick, crack-and pinhole-free. The superconductor transmission lines on the substrate typically do not cover the entire substrate surface. This leads to crossovers in devices as illustrated in Figure 2.2. This necessitates epitaxial planarization in order to deposit the next level of BYC. The temperatures used in the dielectric deposition process must be low to prevent potential chemical reactions between BYC and the dielectric materials. These are issues that must be dealt with for BYC MCM.

2.2 MATERIALS

2.2.1 Barium Yttrium Cuprate

The barium yttrium cuprate ($Ba_2YCu_3O_{7-x}$) [BYC] was discovered in 1987 to be superconducting with a transition temperature (T_c) of 94 K (Wu, 1987). It was the first material discovered to exhibit superconductivity above the boiling temperature of nitrogen (77 K). Its potential use in multichip module depends on the transport electrical properties of the BYC interconnect lines.

The crystal structure of BYC, as shown in Fig. 2.3, can be viewed as three distorted perovskite structures stacking on one another. The lattice parameters for the a-, b- and c- axis are 3.83 Å, 3.88 Å, and 11.7 Å, respectively. The electrical properties depend on the orientation of the crystal due to the crystal structure anisotropy. The theoretical critical current density for single-crystal BYC has been determined by magnetization hysteresis at 4.5 K and an applied field of 40 kG to be 1.7×10^6 A/cm^2 and 9.2×10^4 A/cm^2 for fields perpendicular and parallel to the Cu-O planes, respectively (Dinger, 1987). Thin films can have higher critical current densities because pinning sites increase the J_c by flux pinning. The electrical properties in polycrystalline BYC depend

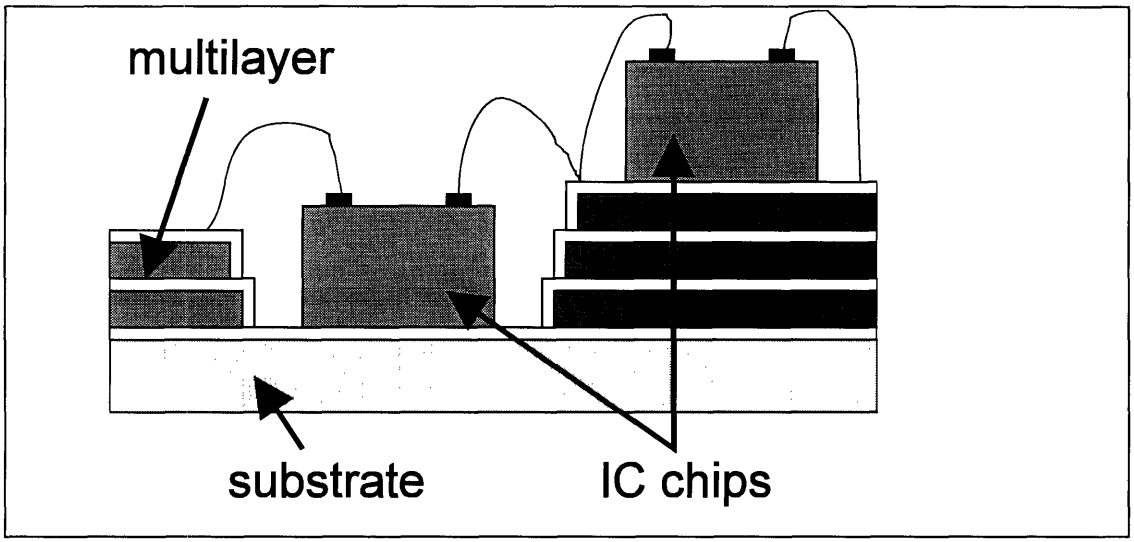

Figure 2.1 A simple multichip module.

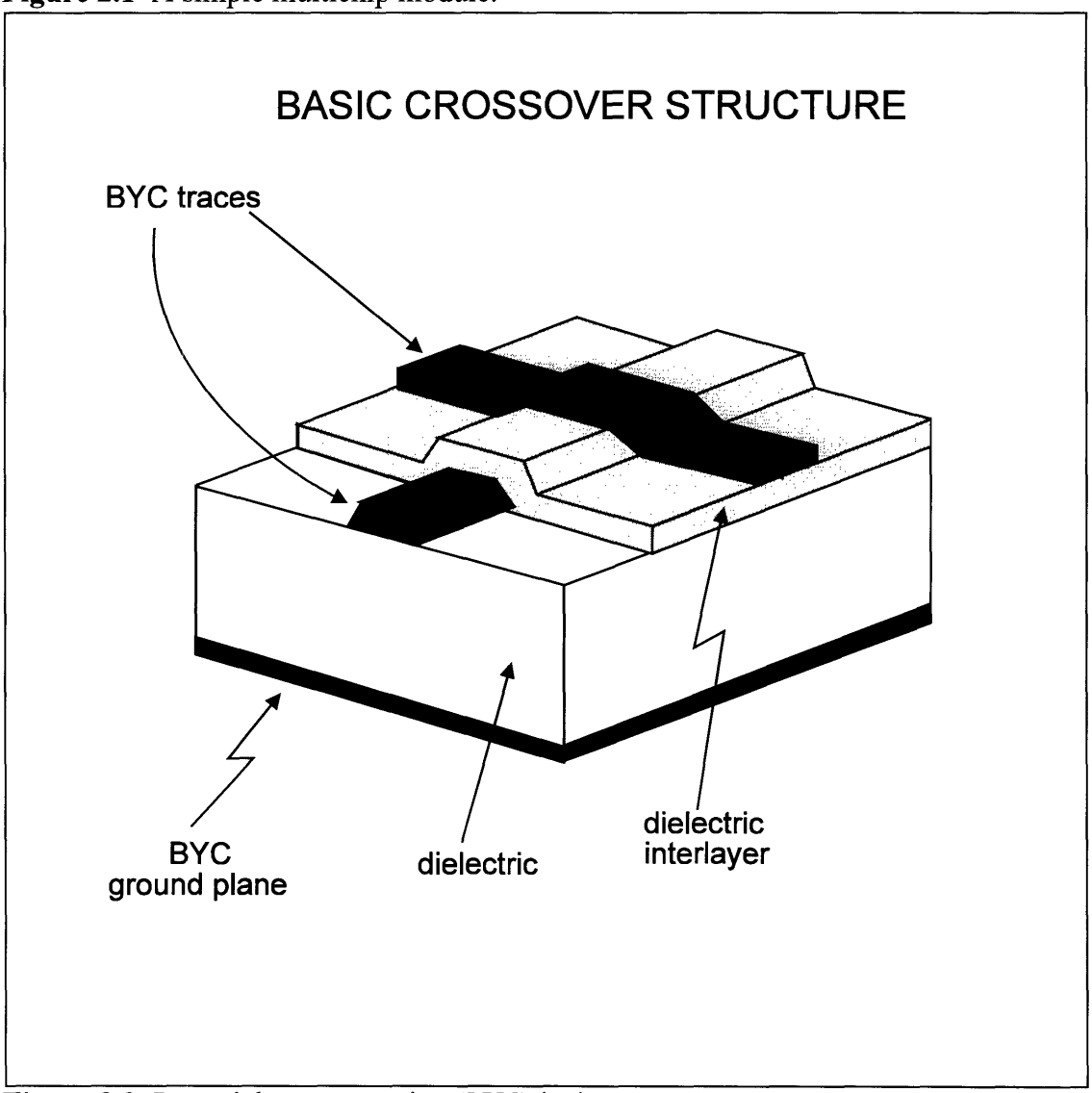

Figure 2.2 Potential crossovers in a BYC device.

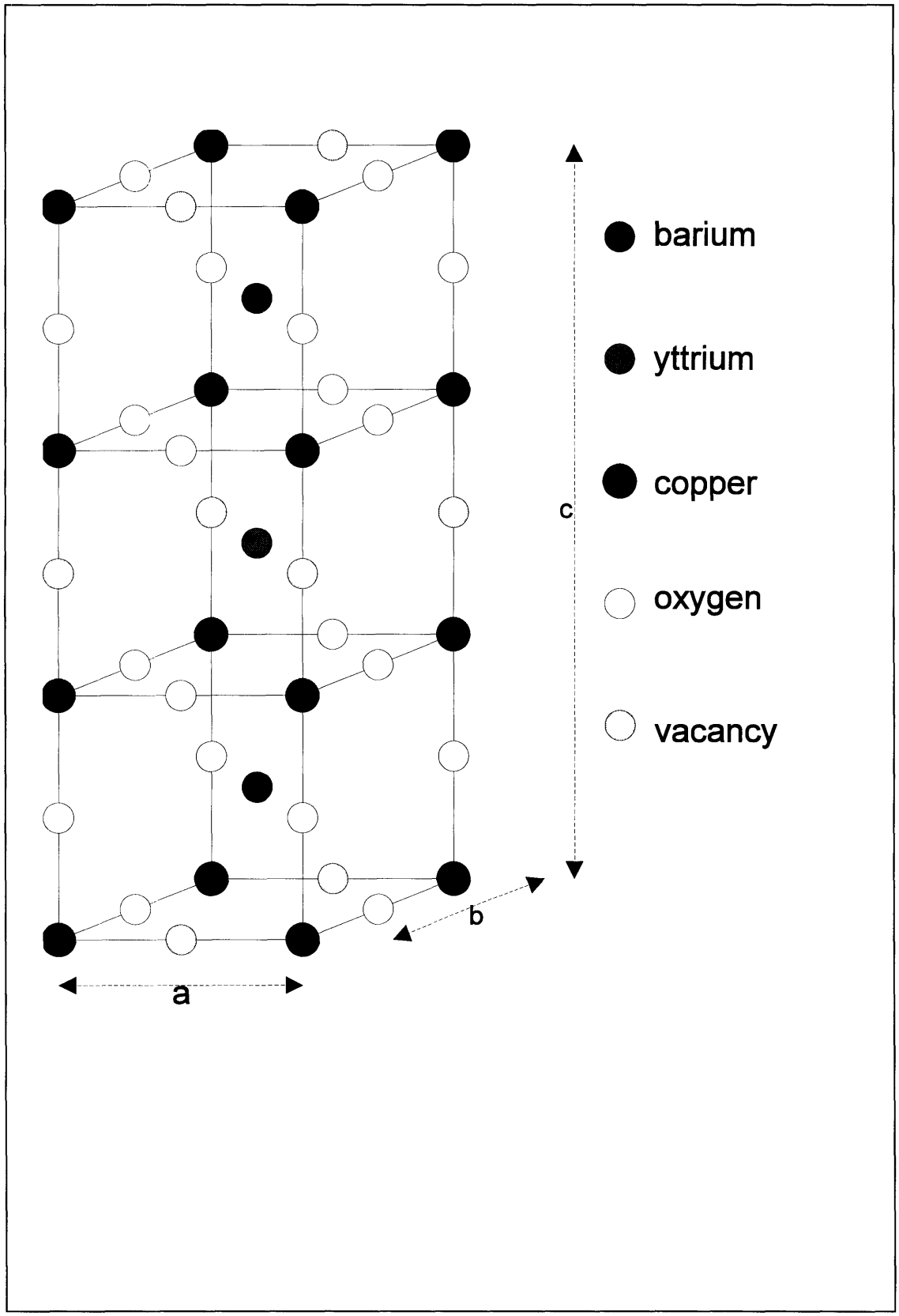

Figure 2.3 $Ba_2YCu_3O_{7-x}$ unit cell.

on the weak links in the grain boundaries. The mismatch of Cu-O planes at grain boundaries, along with the anisotropy of the BYC crystal structure, causes a redistribution of current between the Cu-O planes at grain boundaries and limits the critical current density (Ekin, 1987). It was also shown that, in BYC bicrystals, a small tilt angle about their common c-axes will reduce the J_c (Dimos, 1988). This makes in-plane alignment of BYC grains necessary to obtain high J_c.

2.2.2 Spinel

Magnesium aluminate, or commonly referred to as spinel, is a refractory material with a congruent melting temperature of 2135°C. Spinel solid solution can accommodate excess aluminum oxide (Ryshkewitch, 1960). Spinel is an excellent refractory material with desirable mechanical properties. It can be used as supports for firing sintered alumina at high temperatures. It can also be used as crucibles for melting most metals and some molten slags and salts.

Magnesium aluminate has the normal spinel structure with a lattice constant of 8.086 Å. The unit cell can be regarded as eight elementary cells. Each elementary cell has the oxygen ions in a face-centered cubic packing. The magnesium ion occupies one of the eight tetragonal interstitial sites and the two aluminum ions occupy two of the four octahedral sites (Fig. 2.4). The spinel lattice constant (8.086 Å) is about twice that of the b-axis of BYC (3.88 Å).

2.2.3 Lanthanum aluminate

Polycrystalline lanthanum aluminate has been studied mostly for its catalytic application (Wang, 1992). It has a high melting point of 2075-2110°C (Fay, 1966; Wu, 1992). Single-crystal lanthanum aluminate has become one of the favorite substrate materials for BYC films deposition because of its lattice matching properties and its chemical stability with respect to BYC. Lanthanum aluminate has two crystal structures: a rhombohedral structure at low temperatures, and a cubic perovskite structure at high temperatures (Fig. 2.5). The rhombohedral cell has unit length of approximately 5.357 Å and angle of 60.1° (Geller, 1956; O'Bryan, 1990; Berkstresser, 1991). The rhombohedral cell undergoes a second-order transition to the cubic phase (a_o = 3.793 Å). The reported transition temperature ranges from 435°C to 512°C (Geller, 1956; O'Bryan, 1990). Lanthanum aluminate is generally referred as pseudo-cubic even at room temperature because the difference between the rhombohedral and

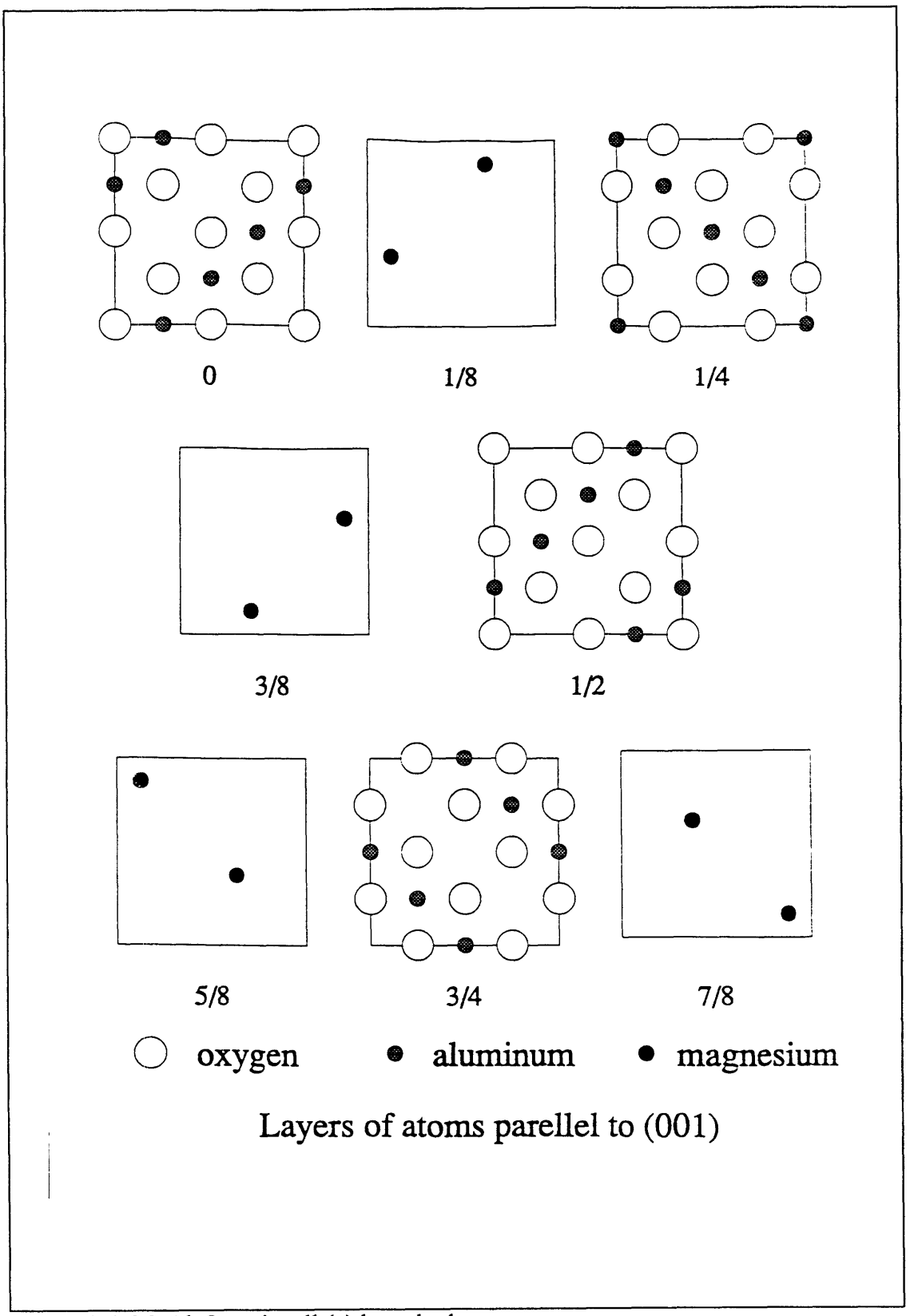

Figure 2.4 $MgAl_2O_4$ unit cell (a) layer by layer arrangement.

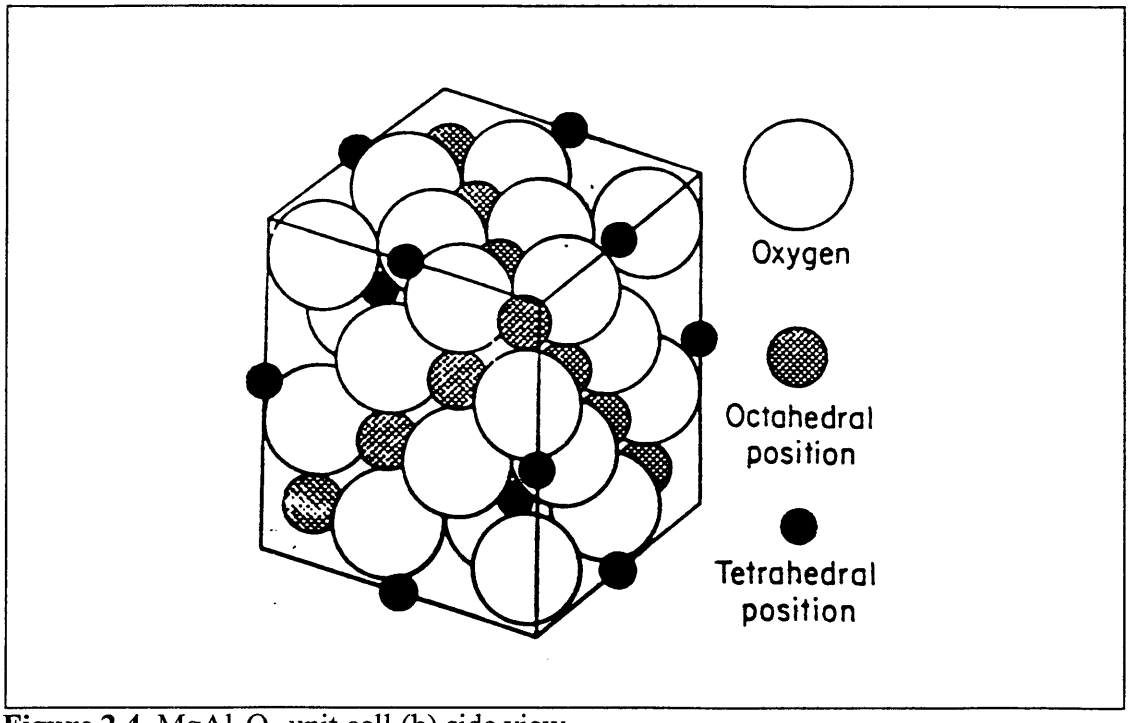

Figure 2.4 $MgAl_2O_4$ unit cell (b) side view.

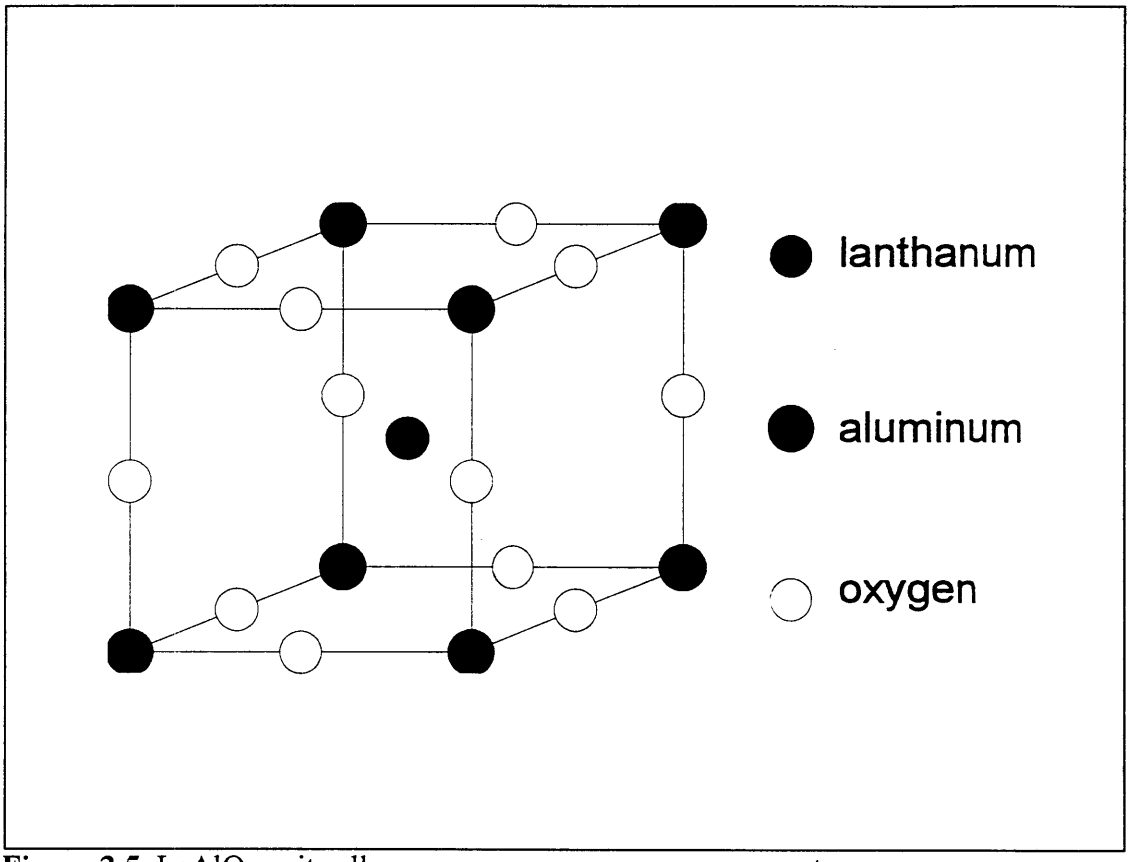

Figure 2.5 $LaAlO_3$ unit cell.

the cubic cell is very small. The cubic notation is used throughout this thesis. Cooling of the cubic $LaAlO_3$ to the rhombohedral phase produces twin planes from the (100) and (110) of the original cubic unit cell (O'Bryan, 1990; Berkstresser, 1991; Yao, 1992). There is no abrupt volume change associated with the cubic-to-rhombohedral transition because the transition is second order. This avoids one additional source of stress in the BYC films when they are cooling from high temperature processing.

2.3 CURRENT DEPOSITION METHODS FOR SPINEL AND $LaAlO_3$ THIN FILMS

2.3.1 Spinel

Epitaxial spinel thin films were deposited by chemical vapor deposition (CVD) on silicon (Matsubara, 1989). $MgCl_2$ and $AlCl_3$ gas were used as the precursors in this type of CVD reaction. Perovskite-type oxide thin films could be subsequently deposited on these CVD spinel films. The temperature used for CVD spinel films was 980°C. This is too high for making BYC multilayer devices, as it approaches the melting point of BYC. Therefore, this method is not suitable for BYC devices.

Studies have been done to deposit epitaxial spinel film by metalorganic chemical vapor deposition (MOCVD) on silicon and (100) MgO substrates (Zhang, 1994). This was done by flash-vaporization of magnesium aluminum isopropoxide dissolved in isopropanol. MOCVD spinel films were deposited at 800°C. Close examination of the SEM micrographs of the MOCVD spinel films, however, revealed rough surfaces. This will cause problems for subsequent deposition of epitaxial BYC films. Therefore, MOCVD spinel films cannot be used in actual devices. CVD or MOCVD methods, in addition, have the disadvantage of having to handling toxic byproducts/reactants.

Radio-frequency sputtering was used to deposit spinel on silicon substrate with a 200 nm thick layer of SiO_2 (Gusmano, 1993; Mattogno, 1994). This technique, however, has yet to demonstrate the feasibility to deposit epitaxial films. The SEM micrographs of the sputtered films also revealed very rough microstructures.

2.3.2 Lanthanum aluminate

Epitaxial lanthanum aluminate thin films were deposited by using off-axis rf sputtering (Lee, 1990) and rf-magnetron sputtering (Sader, 1993). Lee *et al.* reported that $LaAlO_3$ films were deposited at 760°C on either single-crystal $SrTiO_3$ or $LaAlO_3$

substrates. Epitaxial BYC films were subsequently deposited on the sputtered $LaAlO_3$ layer. Sader *et al.* also deposited $LaAlO_3$ on (100) silicon.

There are still many limitations in using physical vapor deposition methods to deposit dielectric layers. The deposition rate is often slow. The deposition areas tend to be small. These methods also need line-of-sight with the vapor source, which makes deposition difficult on nonplanar surfaces. Physical vapor deposition techniques, in addition, require high-vacuum chambers and sophisticated apparatus.

There is some recent work on using a sol-gel approach to deposit $LaAlO_3$ film (Peshev, 1994). The precursors have been lanthanum isopropoxide and aluminum isopropoxide with acetylacetone as a chelate agent. The precursors were spin-coated on sapphire and silica-glass substrates and calcined at 900°C. This chemical method has not yet demonstrated the ability to produce epitaxial films.

2.4 CHEMICAL PRECURSOR APPROACH

Pyrolysis of chemical precursors can be an alternative approach to deposit epitaxial films. Metal salts or metalorganic compounds of controlled stoichiometry are dissolved in volatile solvents. The liquid is applied to the substrate surface by spin coating, dip coating, or spraying. Spin coating is particularly useful in making thin films. After the precursor solution is loaded on the substrate surface, the substrate spins rapidly to remove the excess solution. Only a thin, flat, layer of precursor material is left (Fig. 2.6). The solvent is then allowed to evaporate. Pyrolysis of the precursors forms the desired inorganic phases. Epitaxial films from BYC (McIntyre, 1990) to $SrTiO_3$ (Braunstein, 1994a) to $LiNbO_3$ (Partlow, 1987; Braunstein, 1994b; Nashimoto, 1995) to $Pb(Zr_xTi_{1-x})O_3$ (Peng, 1992) have been deposited by pyrolysis of chemical precursors. This approach has the potential of deposition over large and non-planar surfaces. It also has the potential to planarize trenched surfaces, as in steps planarization in semiconductor devices by spin-on glass. It can produce films that are chemically homogeneous. The process is relatively simple compared to physical or chemical vapor deposition methods.

2.4.1 Double Alkoxide Precursors

A metal alkoxide is a compound where the metal M with valence n is bonded to an alkyl group R with oxygen. The general formula is $M(OR)_n$. Metal alkoxide is first hydrolyzed into metal hydroxide and then converted to metal oxide.

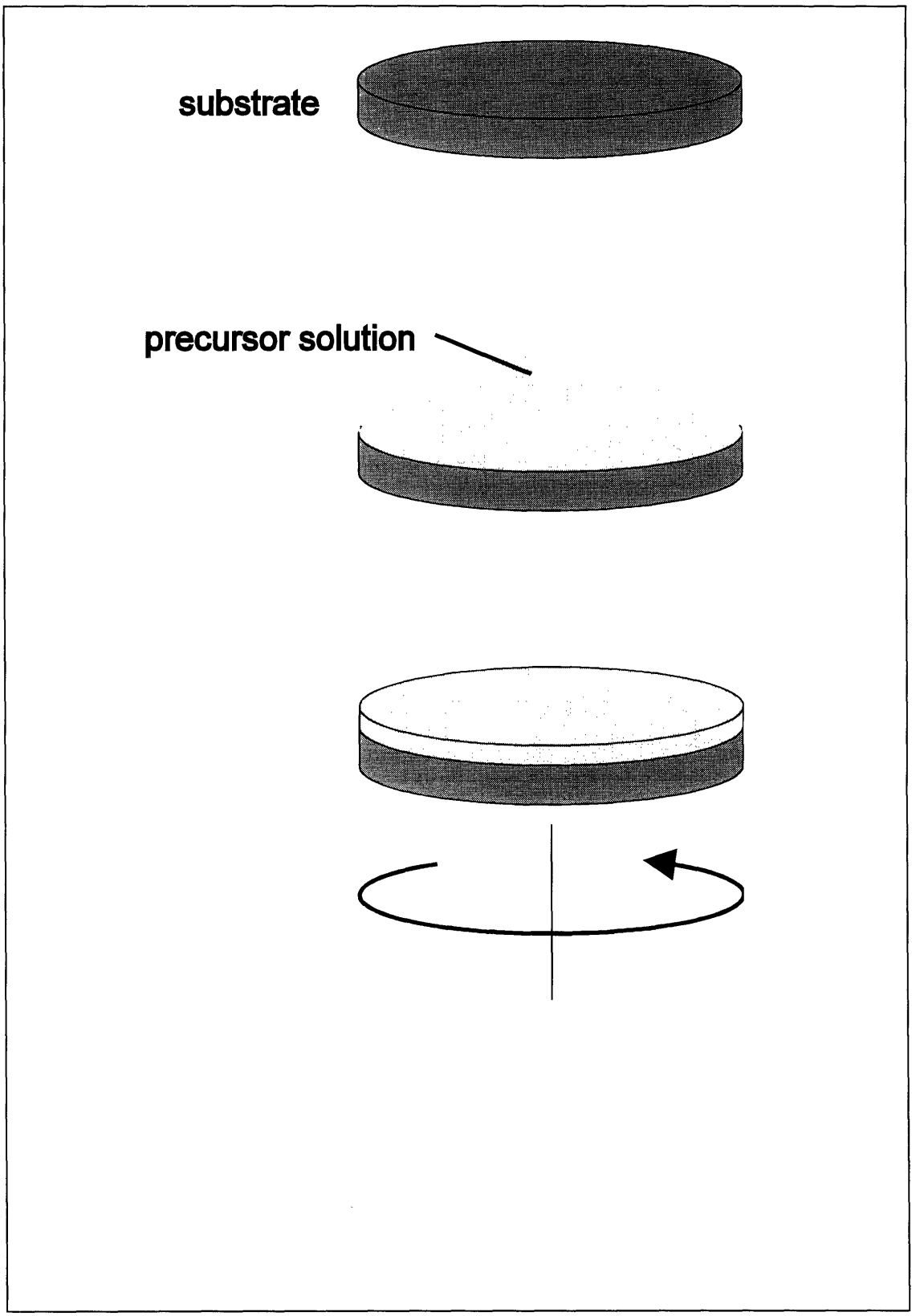

Figure 2.6 Spin-coating process.

$$M(OR)_n + n\,H_2O \rightarrow M(OH)_n + n\,ROH \quad (2.2)$$

$$M(OH)_n \rightarrow MO_{n/2} + n/2\,H_2O \quad (2.3)$$

A double alkoxide is formed when an oxygen atom which is bonded to one metal atom donates a lone pair of electrons to the empty orbital of a neighboring different metal cation (Fig. 2.7). One advantage of using double alkoxide as the precursor is the homogeneity on a molecular level because different cations are bound together. The other advantage is that there is only one decomposition temperature/rate instead two different rates when using two different components. Studies were conducted on double alkoxide as precursors for epitaxial thin films such as $KNbO_3$ (Endo, 1993) and $PbTiO_3$ (Chen, 1989).

Magnesium aluminum isopropoxide ($Mg[Al(OC_3H_7)_4]_2$) has been used as precursor to synthesize $MgAl_2O_4$ powders (Sugiura, 1984), and very recently, in metalorganic chemical vapor deposition of spinel film (Zhang, 1994). $Mg[Al(OC_3H_7)_4]_2$ is extremely moisture sensitive such that it will undergo hydrolysis reaction (Reaction 2.2) in a normal atmosphere. It is soluble in isopropanol and can be distilled at high temperatures under vacuum without dissociating. It has a boiling point of 114°C at 0.2 mm Hg (Mehrotra, 1978).

2.4.2 Nitrate Precursors

The other precursor system used in this study is derived from nitrates. The advantages of using nitrates include simplicity of the process, avoidance of carbon contamination, and low decomposition temperatures when compared to other inorganic salts. Mixed nitrates were used to produce multi-cation ceramic powders, including spinel and $LaAlO_3$ (Kingsley, 1988; Wang, 1992; Lux, 1993). Kingsley *et al.* mixed the nitrates and urea together for combustion at 500°C. The exothermic nature of these combustions often led to actual temperatures that reached 2000°C.

There were attempts to produce epitaxial thin films of multi-cation oxide from mixed nitrates. One potential drawback for using mixed nitrates is the difference in solubilities of different nitrates. This makes it difficult to prepare a precursor solution. One method to get around the problem is by using mostly spray pyrolysis method to avoid segregation. Researchers have used spray pyrolysis to produce BYC films to counter the low solubility of barium nitrate (Blanchet, 1991; Jergel, 1992). Blanchet *et al.* used an aqueous-based precursor solution of yttrium nitrate, barium nitrate, and copper nitrate. The solution was sprayed on MgO at 600°C. The samples were fired at

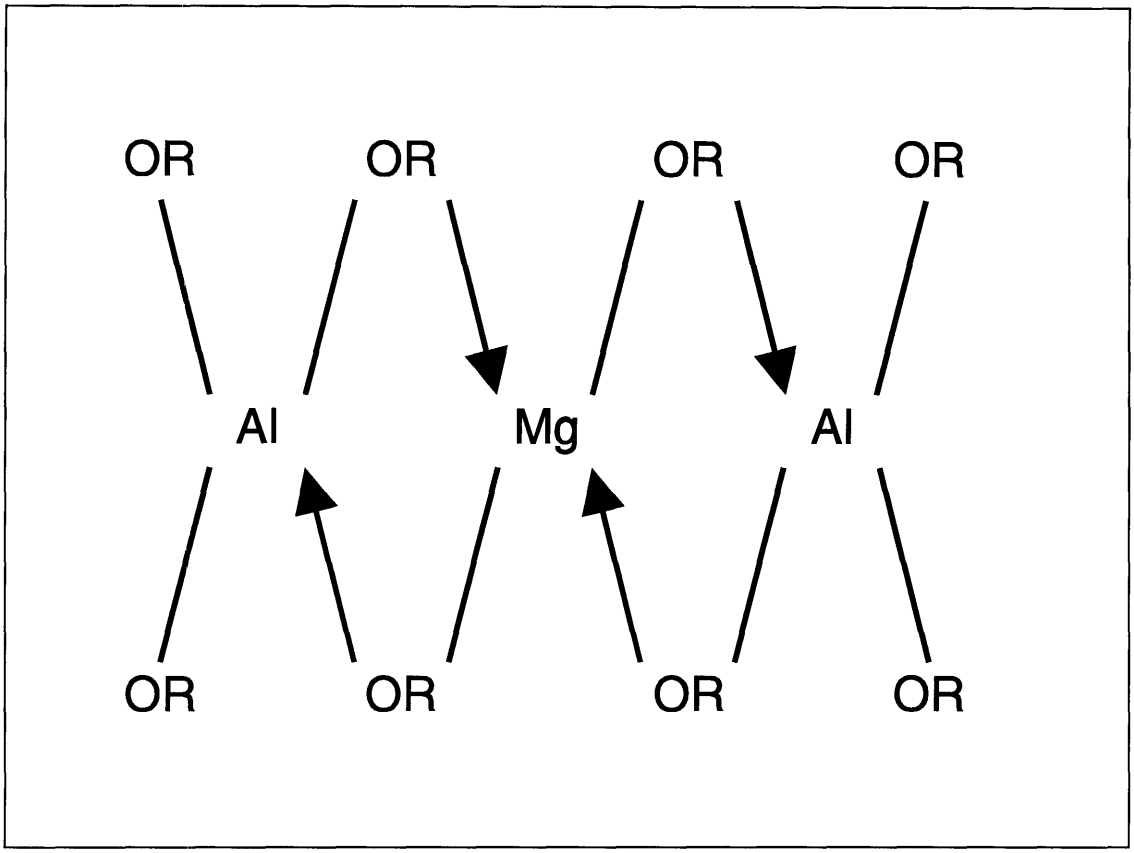

Figure 2.7 Magnesium aluminum double alkoxide molecular structure.

temperatures up to 925°C. The films were epitaxial. The surface roughness measured by profilometry, however, was in the range of 10^3 to 10^5 Å. Jergel *et al.* also used an aqueous-based mixed nitrate precursor that was sprayed onto hot substrate surfaces (between 140°C and 160°C). A partial heating up to 500°C was used to produce intermediate films. Final annealing and oxidizing were performed in vacuum. These BYC films have very rough surfaces, as observed from SEM micrographs, even though they are textured.

A study was done to use nitrate as precursors for homoepitaxy of doped zirconia. Yttrium nitrate was mixed in an aqueous zirconium acetate precursor for making yttrium-doped zirconia film (Miller, 1993). Zirconia single-crystal was used as the substrate. The film first formed small crystallites, and the single-crystal substrate "grew" into the polycrystalline thin film.

Another study has been done to investigate the possibility of using nitrate precursors for multi-cation oxide (Vaidya, 1994). This used gadolinium nitrate or neodymium nitrate and aluminum nitrate aqueous solution to produce polycrystalline $NdAlO_3$ or $GdAlO_3$. Afterwards the polycrystalline $NdAlO_3$ or $GdAlO_3$ reacted with the sapphire substrate to produce $NdAl_{11}O_{18}$ or $GdAl_{11}O_{18}$ epitaxial thin films.

2.5 HETEROEPITAXY

This section will briefly introduce a few terms and general information related to heteroepitaxy. Epitaxy is generally defined as when the film and the substrate share an interface with a highly coincident atomic structure. Homoepitaxy occurs when the film and the substrate are of the same materials. Heteroepitaxy is when the film and the substrate are of different materials. Heteroepitaxy introduces a mismatch between the film and the substrate because the two have different lattice parameters. The mismatch is commonly defined by

$$\text{mismatch} = (a_o - a_s)/a_s \tag{2.4}$$

where a_o and a_s are the stress-free lattice parameters for the substrate and film, respectively.

There are three models for the initial epitaxial film formation in vapor deposition. They are the Frank-Van der Merwe (FM) growth mode which is a layer-by layer growth; the Volmer and Weber (VW) growth mode which is formation and growth from discrete nuclei; and the Stranski and Krastanov (SK) growth mode which is initial

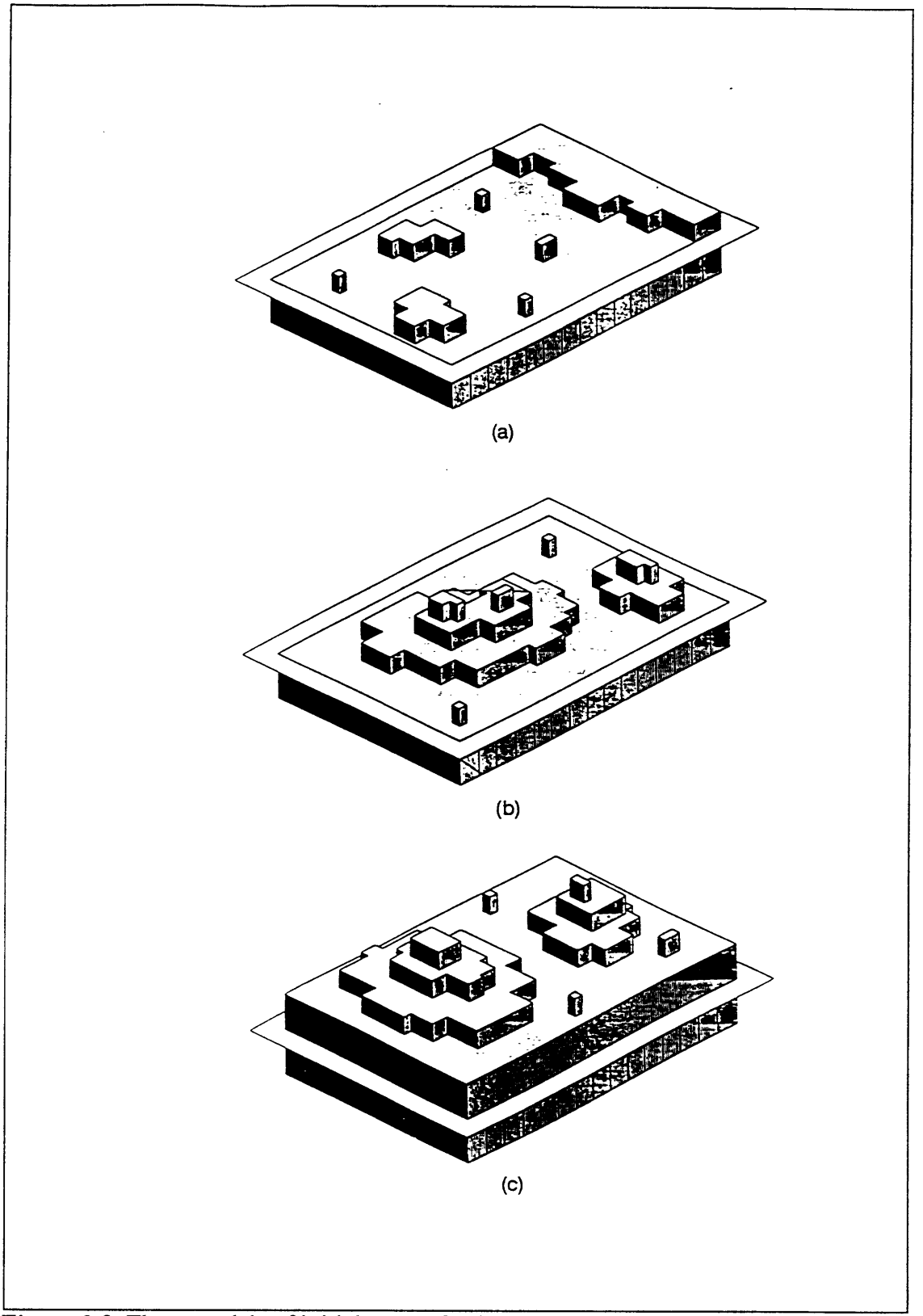

Figure 2.8 Three models of initial stage of epitaxial growth. (a) Frank-van der Merwe, (b) Volmer-Weber, and (c) Stanski-Krastanov (Peercy, 1990).

formation of a tightly bound layer followed by nucleation and growth. The three modes are illustrated in Fig. 2.8.

The actual growth mode depends on the film/substrate lattice mismatch and the relative surface energies of the film and substrate. The surface energy term S is defined as

$$S = \gamma_s - \gamma_i - \gamma \tag{2.5}$$

where γ_s is the substrate-vacuum interface specific surface free energy; γ_i is the substrate/film interface specific surface free energy; and γ is the film/vacuum interface specific surface free energy. SK or FM mode occurs when $S < 0$; VW mode occurs when $S > 0$ (Bruinsma, 1987). SK mode typically replaces FM mode unless the misfit is small or the film can elastically accommodate the misfit caused by heteroepitaxy. These models are developed for vapor deposition epitaxial growth.

Solid-phase homoepitaxy has been studied extensively in semiconductor recrystallization. A well-known example is growing of silicon. Typically a layer of amorphous or polycrystalline film is deposited on a single-crystal substrate. Then the substrate grows into the amorphous layer during annealing (von Allmen, 1979; Schins, 1980; Tsaur, 1980). A similar mechanism was reported in epitaxy of yttrium-stabilized zirconia films on zirconia substrate. The zirconia substrate grew into the nanopolycrystalline intermediate film. The yttrium-stabilized zirconia layer was of the same structure as the substrate except for the lattice strain (Miller, 1993).

The substrate cannot grow into the intermediate layer in heteroepitaxial film growth. There are four different mechanisms in which heteroepitaxial films can be grown from solid intermediate films. They are illustrated schematically in Fig. 2.9. The first mechanism involves the nucleation of epitaxial grains at the film/substrate interface (Fig. 2.9a). These epitaxial grains grow by consuming the intermediate film. This mechanism is similar to solid-state homoepitaxial growth of amorphous silicon on silicon substrate. This is also observed in heteroepitaxy of $LaAlO_3$ films derived from metalorganic deposition (MOD) on $SrTiO_3$ substrate (Braunstein, 1994a).

The kinetics of epitaxial growth from amorphous phase has mainly been investigated in the homoepitaxial growth of silicon. The growth is typically layer-by-layer and the fraction of crystallization is linear with time. There have not been many studies in heteroepitaxial growth from amorphous intermediate film on the other hand. The only study done was on barium ferrite ($BaFe_{12}O_{19}$) film on sapphire (Parker, 1993). Different orientations grew at different rate in barium ferrite because its crystal structure is hexagonal. The Johnson-Mehl-Avrami exponent of transformation ranged from 2.3

to 3.1 within a growth temperature range from 675°C to 725°C. The reported data suggested that the kinetic route of epitaxial growth changed with temperature. There has been hardly any other kinetics study on heteroepitaxy from amorphous materials, even in a simple cubic system.

The second mechanism is a multiple-step process (Fig. 2.9b). A polycrystalline film is formed initially. Subsequent grain growth produces grains with size on the order of the film's thickness. The difference in the surface and interfacial energies of the grains is the driving force promoting grain growth. Once the size of the grains approaches the thickness of the film, grains with certain orientation grow at the expense of grains of other orientation. Epitaxial grains, which generally have lower energy, grow and consume other grains. It is, nonetheless, not required that it is lattice-matched. For as long as there is one orientation with minimum surface energy, grains with that orientation will eventually dominate. This phenomenon has been observed in metallic films (Thompson, 1990).

The third mechanism is the formation of a transient liquid in which the epitaxial phase precipitates (Fig. 2.9c). One example is in MOD BYC films derived from metal trifluoroacetate precursors (McIntyre, 1993). A melt was formed that helped to dissolve the intermediate films and precipitated BYC grains. Another example was in MOD derived Bi-based superconductor (Golden, 1992). This system also exhibited partial melting that directly led to formation of the superconductor phases during the high temperature process.

The fourth mechanism is the reaction between the substrate with the intermediate film to produce a new layer at the interface (Fig. 2.9d). This reaction requires the diffusion of species from either the intermediate film or the substrate to continue the growth. This has been observed in the formation of epitaxial Mg_2TiO_4 layer from deposition of TiO_2 on MgO (Hesse, 1983); epitaxial $GdAl_{11}O_{18}$ layer from $GdAlO_3$ film and sapphire substrate (Vaidya, 1994); epitaxial $NiSi_2$ and $CoSi_2$ films on silicon substrate (Grimberg, 1993; Vantomme, 1994); and epitaxial $BaZrO_3$ layer from $Ba_2YCu_3O_{7-x}$ film on YSZ substrate (Shapiro, 1991).

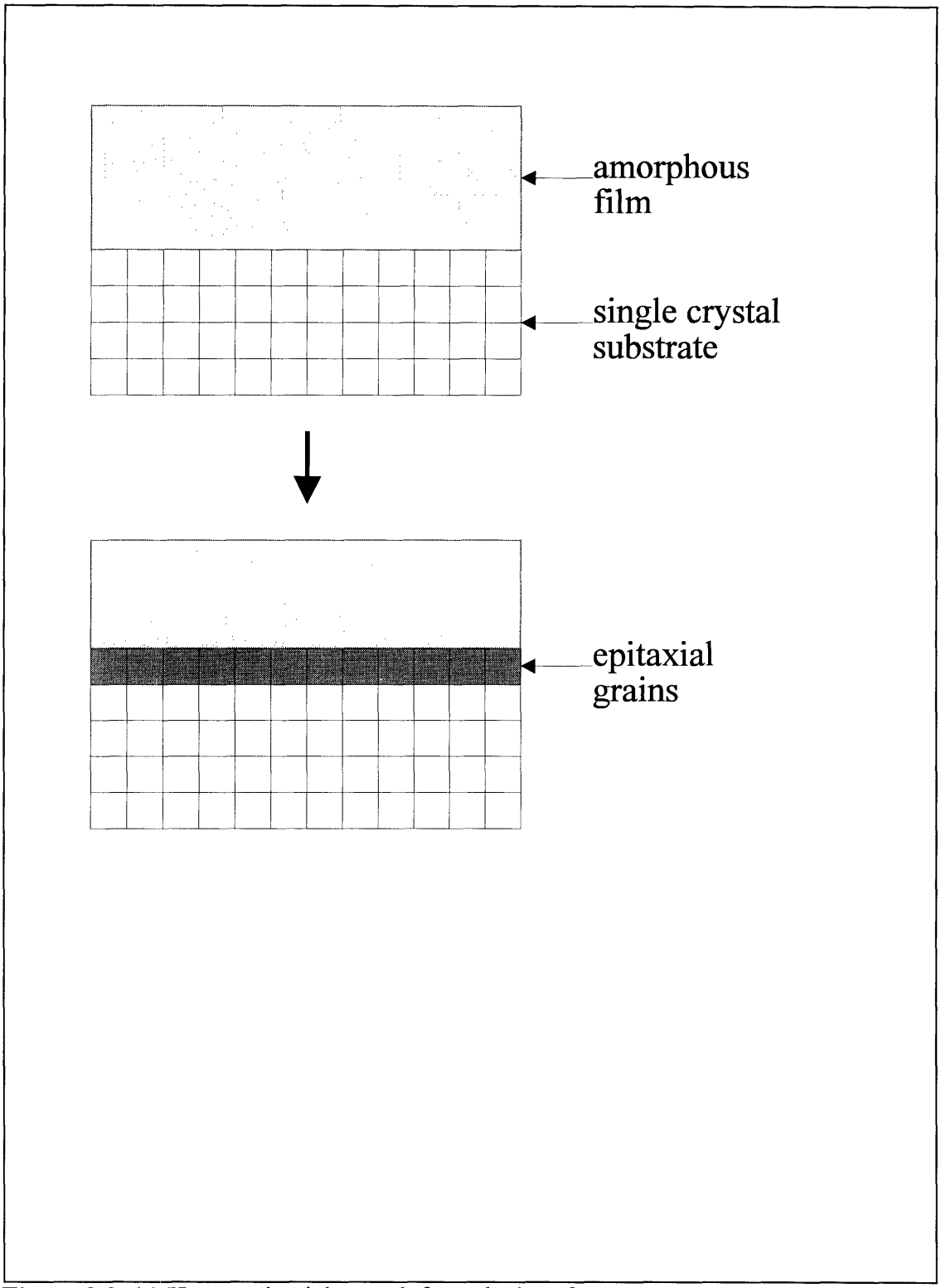

Figure 2.9 (a) Heteroepitaxial growth from the interface.

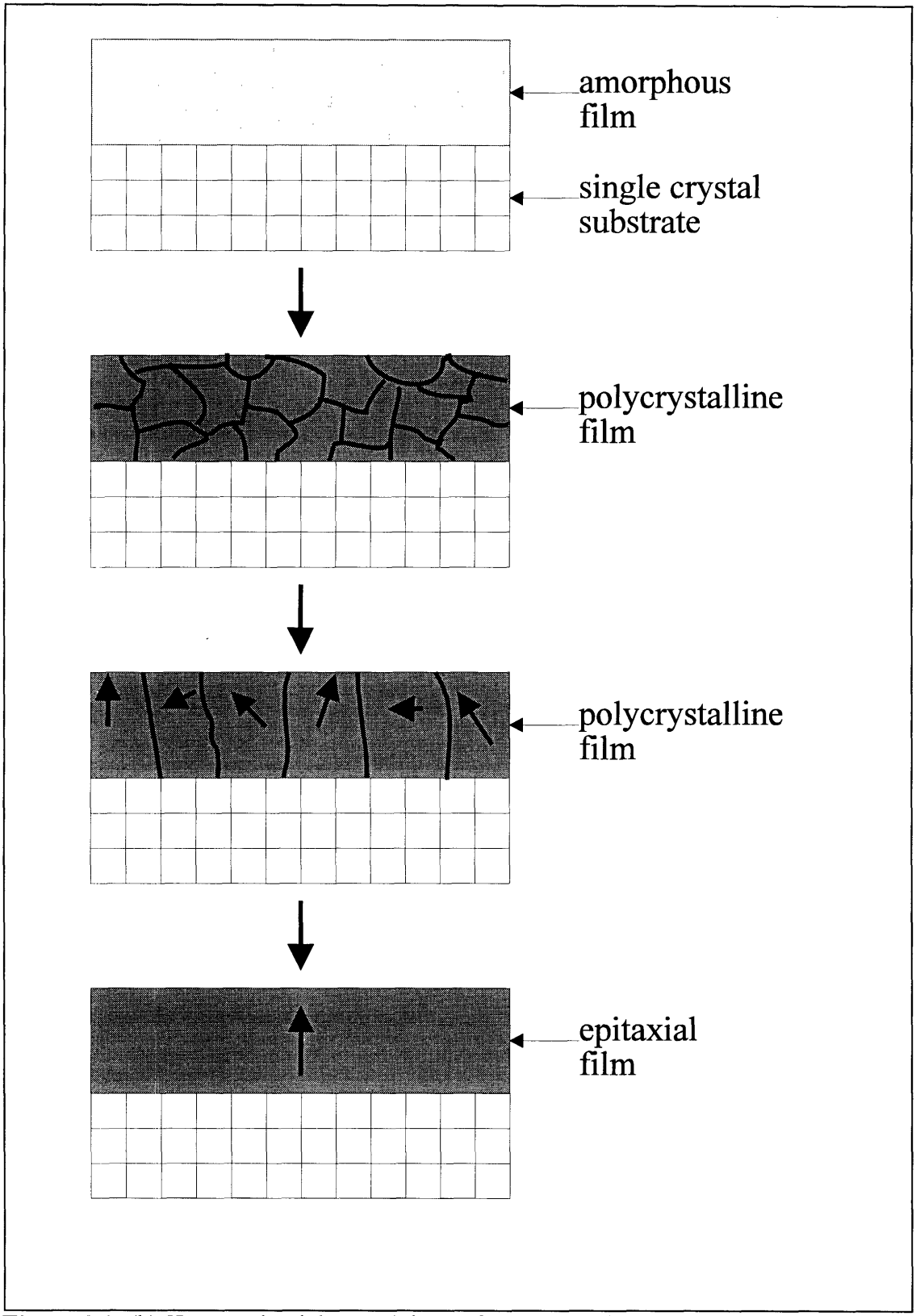

Figure 2.9 (b) Heteroepitaxial growth by surface energy driven secondary grain growth.

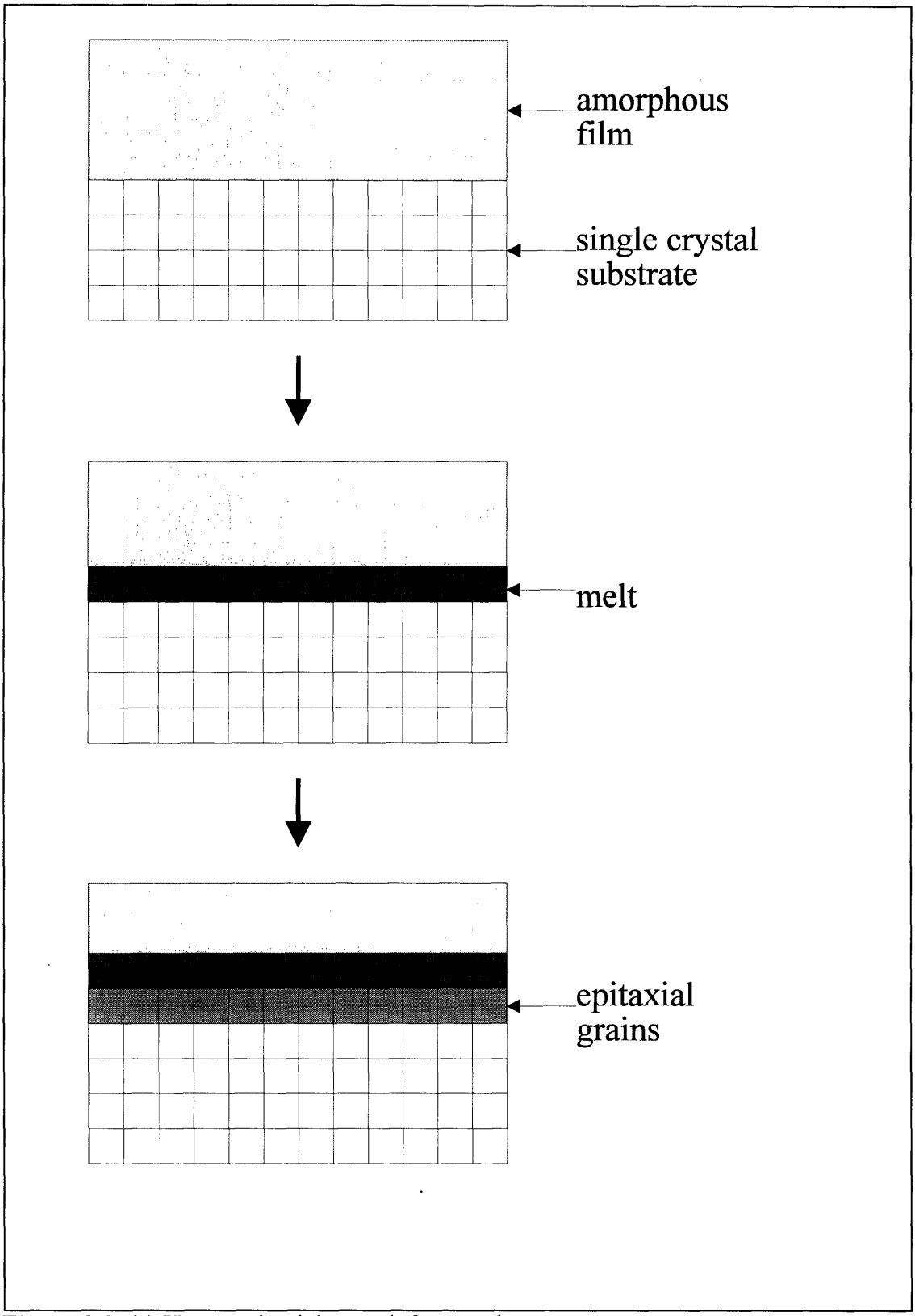

Figure 2.9 (c) Heteroepitaxial growth from melt.

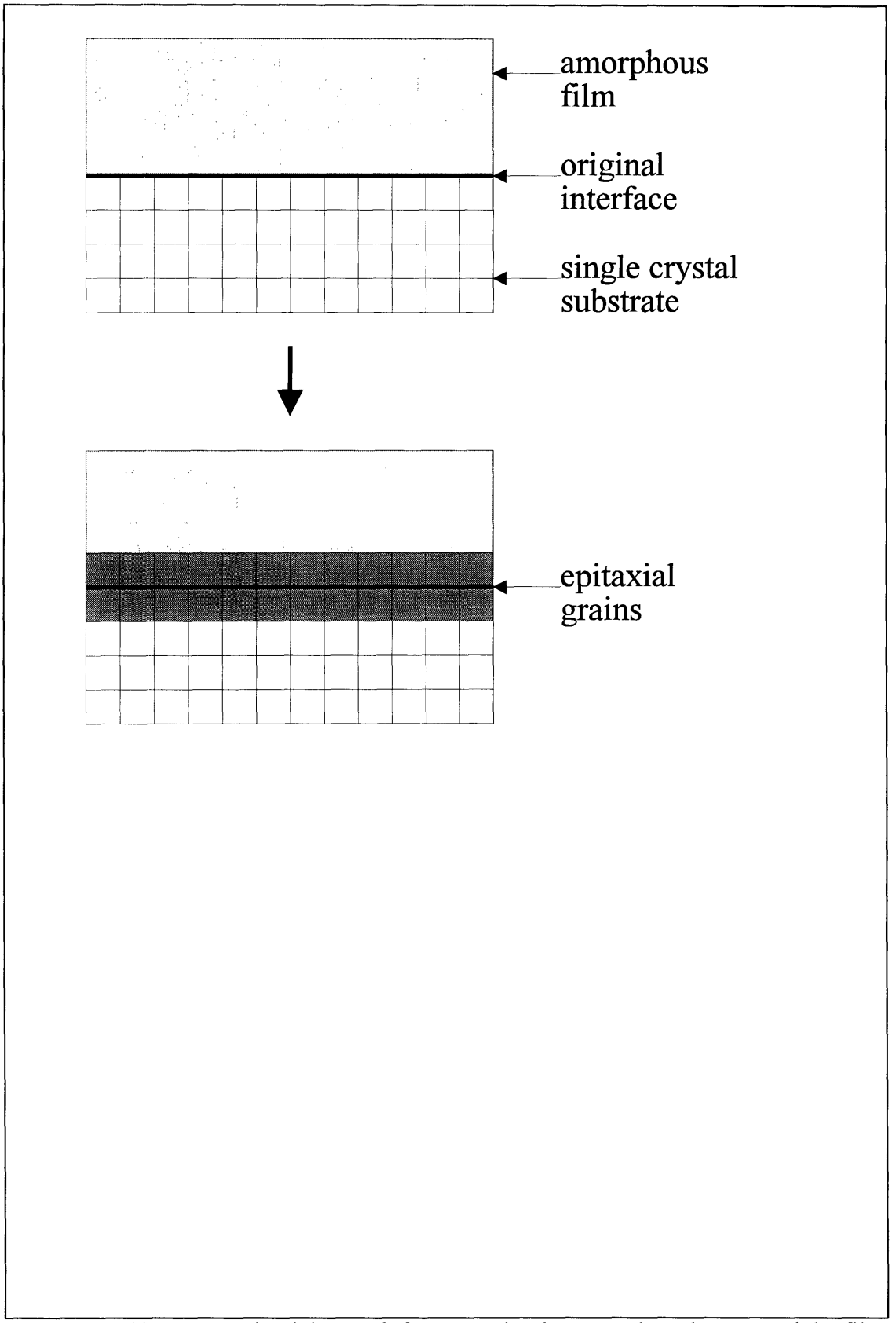

Figure 2.9 (d) Heteroepitaxial growth from reaction between the substrate and the film.

CHAPTER 3
DECOMPOSITION OF PRECURSORS

3.1 INTRODUCTION

This chapter examines the decomposition chemistry of all three precursor systems used in this thesis: magnesium aluminum isopropoxide, magnesium-aluminum nitrates, and lanthanum-aluminum nitrates. Understanding the decomposition routes of chemical precursors is important in controlling the chemical composition, phases, porosity, and grain structures of the resultant ceramic products. Experiments were performed to either supplement or verify information available in literature. These experiments mainly investigate the chemical composition of each precursor system at various stages of decomposition prior to crystallization. They do not investigate in detail the breakdown of the complicated molecules. Powder samples, instead of thin film samples, were used in certain experiments whenever it would be easier to obtain the interested information. The understanding gained in the decomposition processes will be used in the later studies in surface structure control (Chapter 4) and in epitaxial growth (Chapter 6).

3.2 EXPERIMENTAL PROCEDURE

3.2.1 Precursor Preparation

Magnesium aluminum isopropoxide was made by a method similar to that used by others (McMahon, 1986). The overall reaction is

$$Mg + 2\ Al(OPr^i)_3 + 2\ Pr^iOH \rightarrow Mg[Al(OPr^i)_4]_2 + H_2. \qquad (3.1)$$

Figure 3.1 is a flowchart illustrating the procedure in magnesium aluminum isopropoxide synthesis. The refluxing and distillation units used were connected to a Schlenk line to ensure rapid switching from a dry nitrogen environment to vacuum without any exposure to the outside atmosphere. The isopropanol was dried by heating it with CaH_2 and was distilled before use. Extreme care was taken to avoid any introduction of moisture during each step of processing.

A round-bottom flask was loaded with magnesium metal turnings, an excess amount of aluminum isopropoxide, and a trace amount of mercuric chloride (as catalyst). The reactants and an excess amount of dried isopropanol were loaded in a dry box. A reflux

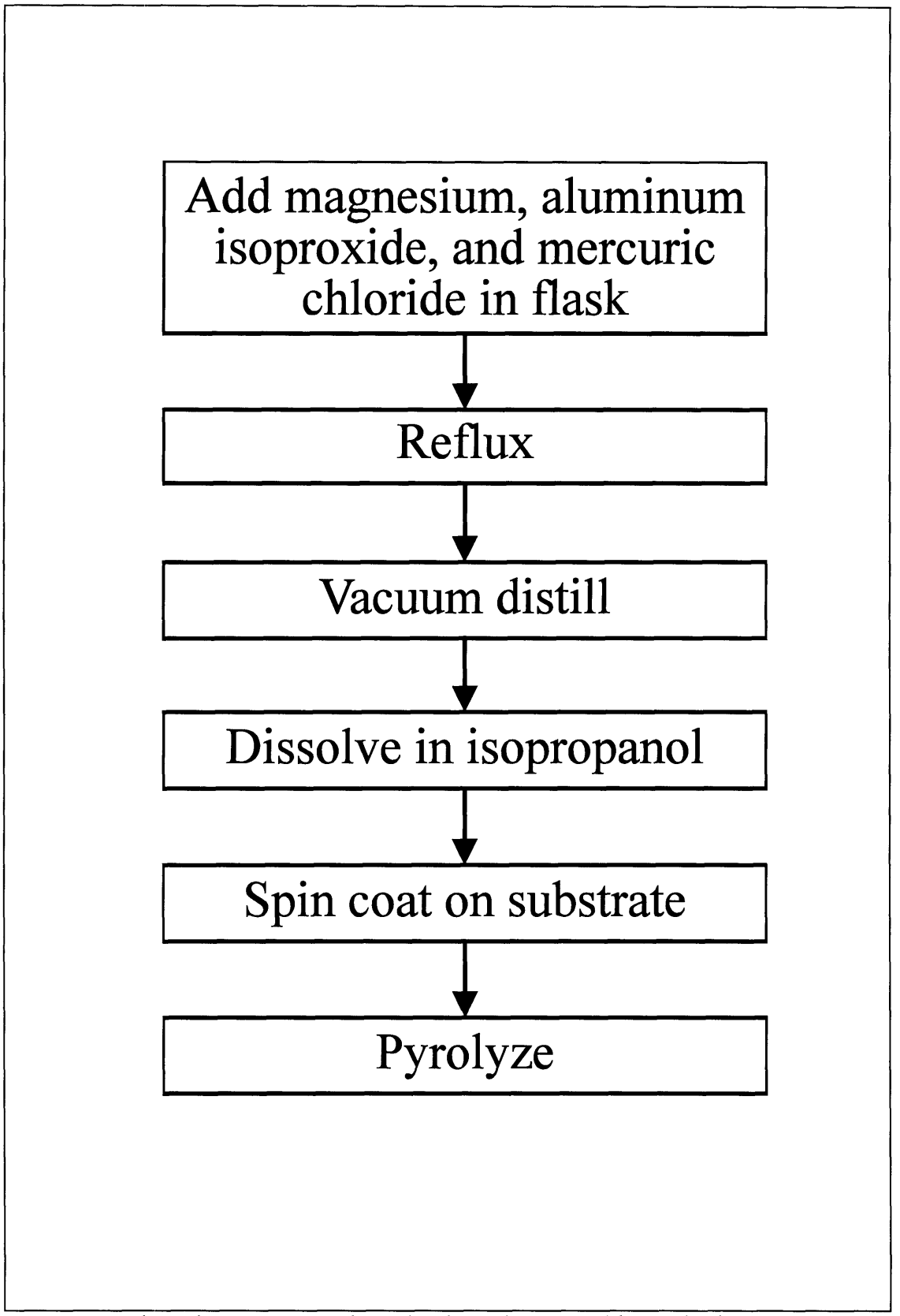

Figure 3.1 Flow chart on magnesium aluminum isopropoxide synthesis.

condenser was connected to an empty round bottom flask which had been filled with flowing nitrogen. The empty round-bottom flask was quickly replaced by the flask with reactants. The flask was refluxed for two days under a nitrogen atmosphere. The reaction flask was exposed to a mechanical pump for 24 h after refluxing to remove the solvent. The product was vacuum distilled at approximately 120°C. The resulting product, a clear, viscous liquid, was collected in a flask that had also been filled with nitrogen before distillation. The collection flask was quickly removed from the distillation unit and capped with a septum. A syringe connected to a vacuum line was used to evacuate all the gas inside the flask. The flask was then transferred to and stored in a dry box under flowing nitrogen.

A set of FTIR (Fourier Transform Infrared Spectroscopy) experiments was performed with thin film samples to determine the chemical composition at various stages of the magnesium aluminum isopropoxide decomposition. The magnesium aluminum isopropoxide precursor was diluted in a 11:1 dried isopropanol:alkoxide ratio inside a dry box. The solutions were filtered with a 0.22 μm ceramic tip filter to eliminate any large particles from the solution. The solution was coated on small pieces of (111) silicon wafer inside a dry box. The films were transported to a tube furnace which was attached to the dry box and filled with dry nitrogen without exposing to atmosphere. The furnace was switched to either dry oxygen or nitrogen gas for about 30 min before pyrolysis. The humid atmosphere was produced by first letting the furnace gas bubble through a 3-liter flask full of water before the gas entered the furnace. The relative humidity of the gas was typically > 80 %.

The mixed nitrates precursors for lanthanum aluminate and spinel were produced by dissolving stoichiometric amounts of aluminum nitrate ($Al(NO_3)_3 \cdot 9H_2O$) and lanthanum nitrate ($La(NO_3)_3 \cdot 6H_2O$) or magnesium nitrate ($Mg(NO_3)_2 \cdot 6H_2O$) in methanol or a methanol-isopropanol solution. Calculations from thermogravimetric analyses showed that the actual amounts of water of hydration for these nitrates were slightly lower than labeled. The correct stoichiometric amounts were used. The solutions were stirred with a magnetic stirrer for 30 min. Solutions of different concentration were made. Concentration is expressed in units of osmolar (mole solute/liter solvent) in this thesis. Powder samples were made by drying the methanol-based solution and pulverizing the solid.

3.2.2 Materials Identification

The as-made magnesium aluminum isopropoxide was analyzed by FTIR. The magnesium aluminum isopropoxide was sandwiched between two potassium bromide crystal disks while inside a dry box. Parafilm was wrapped around the edges of the crystals to prevent moisture from getting into the magnesium aluminum isopropoxide. The sample was then transported immediately to an IBM IR/44 spectrometer chamber that had been filled with dry nitrogen. The spectrometer was equipped with a mercury cadmium telluride detector. The sample then stayed inside the chamber for an addition 10 min to ensure an atmosphere free of carbon dioxide and moisture before analyses. Transmission FTIR spectra were acquired at a resolution of 8 cm^{-1} using 100 scans. The intermediate films from pyrolysis of magnesium aluminum isopropoxide on silicon substrate were also analyzed by the same approach.

A variant of this method to study the chemical composition at different stages of decomposition is by Diffuse Reflectance Infrared Fourier Transform Spectroscopy (DRIFTS). It was also done in the IBM IR/44 spectrometer. Electronic grade potassium bromide powder was first mixed and ground with the intermediate products. The mixture was pressed into a pellet and placed inside the spectrometer chamber. Dry gas was flowed into the chamber for 10 min before analysis to avoid contamination from atmospheric carbon dioxide or water. The spectra were acquired with 100 scans and a resolution of 8 cm^{-1}.

The intermediate products of pyrolysis of these precursors were also studied by X-ray diffraction (XRD) using the standard θ-2θ technique. This was done by a powder diffraction configuration using Cu-K_α radiation generated by a rotating anode with a 50 kV, 200 mA electron beam bombardment. The diffracted beam was measured by a scintillation detector. The configuration used a divergence slit of 1/2°, a scatter slit of 1/2°, and a receiving slit of 0.15 mm. Full scans were measured with 2θ from 20° to 70° at a rate of 5°/min with step size of 0.02° and a dwell time of 1 s.

3.2.3 Processes Determination

The decomposition processes of the precursors were analyzed by thermogravimetric analysis (TGA) and differential thermal analysis (DTA). TGA was performed only in a dry atmosphere for magnesium aluminum isopropoxide because of its moisture-sensitive nature. DTA and TGA were performed in both dry and humid atmospheres for the mixed nitrates. A Netzsch Model STA 429 thermal analyzer was used for both DTA

and TGA for a set of experiments in which both dry and humid atmospheres were involved. A Seiko Model 320 thermal analyzer or a Perkin-Elmer TGA7 thermogravimetric analyzer was used for other TGA/DTA experiments.

Supplemental melting experiments were performed to confirm the melting temperatures of the mixed nitrates with the reported values. Mixed nitrates of different cationic ratios were prepared to determine the sensitivity of temperature on composition. These were done by placing dried nitrate precursor powders inside capillary tubes and observed the melting while heating them. Small capillary tubes of size 1.5-1.8 mm in diameter were filled to about 0.5 inch with powder. The heating was done in a dry box to avoid any moisture introduced from the surrounding air. The capillary tubes were tied to a thermometer and inserted into a mineral oil bath that was heated by a hot plate. The temperature was controlled by adjusting the power to the hot plate for both heating and cooling.

Most of the available information on nitrate meltings is for bulk samples. It is easy for the molten nitrates to be deprived of their water of hydration in thin film form because of the larger surface area to volume ratio. The stability of the dehydrated nitrates was investigated. Attempts were made to produce dehydrated aluminum nitrate and magnesium nitrate by vacuum heating to separate the water loss effect from other effects.

The possibility of liquid formation at higher temperatures was investigated. The nitrate powders were pressed into pellets after an initial pyrolysis and then annealed isothermally at 500°C and 600°C for 2 h. The shapes of the pellets were observed to determine if any distortion occurs. A liquid phase would not be likely to have formed during annealing if the pellets were not distorted. This set of experiments was used to confirm the DTA results at high temperature.

3.3 RESULTS AND DISCUSSION

3.3.1 Magnesium Aluminum Isopropoxide

The FTIR spectrum of magnesium aluminum isopropoxide made in this study (Fig. 3.2) matched closely with the reported spectrum (Mehrotra, 1978). A sample of the as-made magnesium aluminum isopropoxide was sent for chemical analysis by atomic absorption (performed by E & R Microanalytical Laboratory, Inc., Corona, NY). The analyzed cationic ratio of Mg:Al was 1:2.09. The slightly Al-rich ratio suggested that small amount of aluminum isopropoxide may still be in the precursor even though any

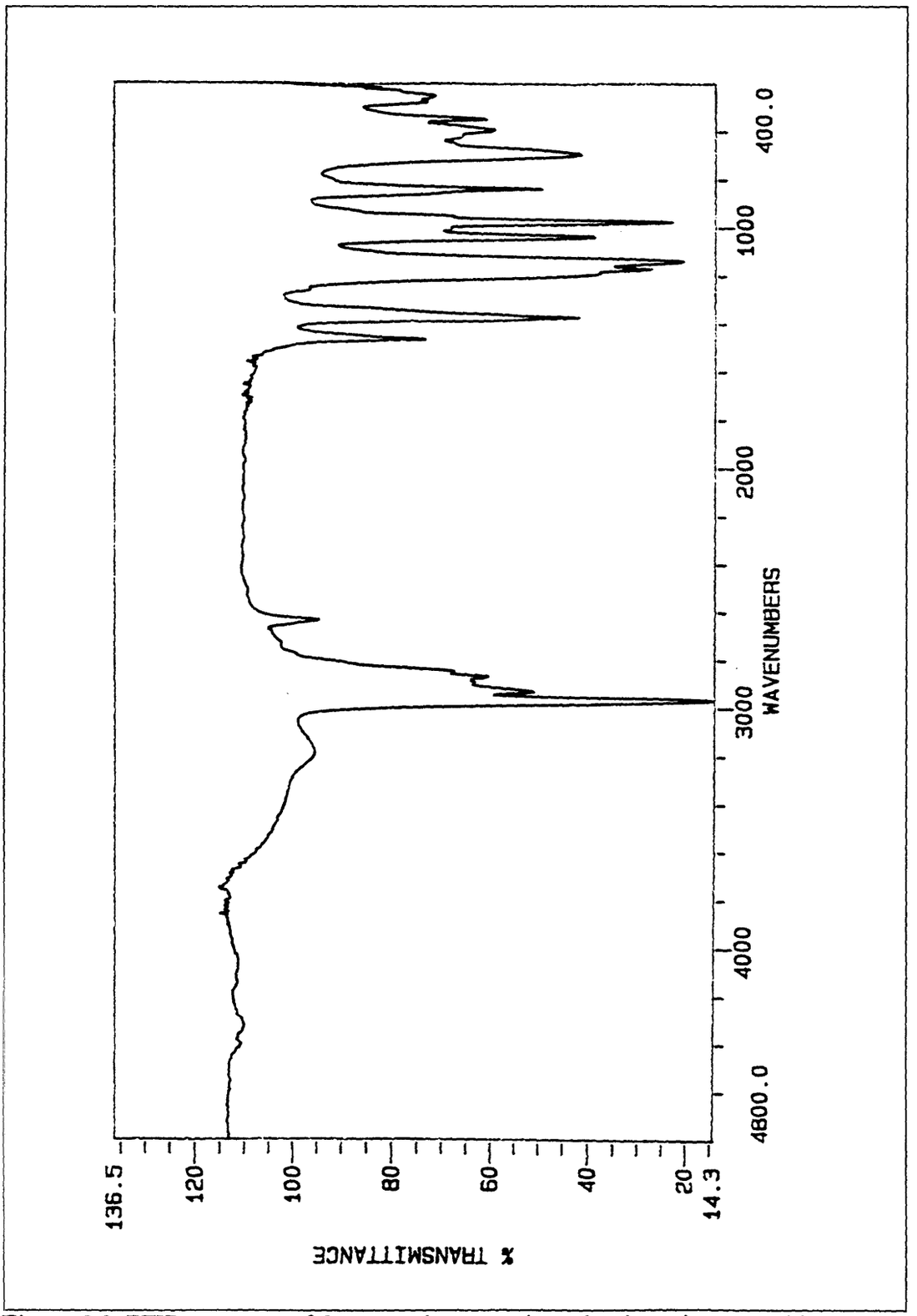

Figure 3.2 FTIR spectrum of the as-made magnesium aluminum isopropoxide.

excess amount of aluminum isopropoxide should vaporize off during distillation (Mehrotra, 1978).

The TGA curve of the precursor pyrolyzed in dry air at a rate of 1°C/min showed that while most of the weight loss occurred below 300°C, there was a small amount of weight loss persisting at up to 500°C (Fig. 3.3). FTIR spectra were obtained from magnesium aluminum isopropoxide spun on silicon substrates. In the sample which was first hydrolyzed for 1.5 h at 100°C in a moist oxygen atmosphere followed by heating to 300°C in a dry nitrogen atmosphere, the hydroxyl absorption band (O-H) was absent. Films that had been heated to 300°C in oxygen still had the O-H absorption band. Reaction (2.3) suggests that the double alkoxide precursors would become an amorphous oxide by approximately 300°C if heated in suitable conditions. XRD spectrum showed that the pyrolyzed product is amorphous at that stage. This is consistent with reported path of decomposition (Sugiura, 1984). The material remained amorphous until spinel crystallization.

3.3.2 Magnesium-Aluminum Nitrates

Most metal nitrates are known to melt at low temperature (<200°C). Aluminum nitrate is reported to melt at 73.5°C and magnesium nitrate at 89°C (CRC Handbook, 1975-1976). It is critical to know the melting temperatures of the precursor films because a melt can accommodate volume change without cracking. Thus, it is also necessary to find out the melting temperatures of the mixed nitrates and how the temperatures change with composition.

The results from melting experiments in capillary tubes are listed in Table 3.1. Magnesium nitrate liquefied at 89°C and aluminum nitrate at 74°C, as expected from the literature. The melting temperatures of the mixed nitrates were consistently at 67°C, even when the composition varied extensively. This invariant of melting temperatures had the appearance of a eutectic melting. The same samples were heated and cooled repeatedly to observe the melting. Cyclic heating and cooling would generate the same liquidius if it were a melt. The cooled samples, however, did not exhibit the same liquefaction phenomenon again.

DT/TGA results were analyzed to verify whether melting really had occurred. The TGA curves showed continuous weight loss from room temperature to beyond the "eutectic" temperature of the mixed nitrates. The TGA curves showed that significant weight loss (more than explainable by water loss alone) started at temperatures much lower than 67°C. It was difficult to interpret the TG/DTA curves due to the

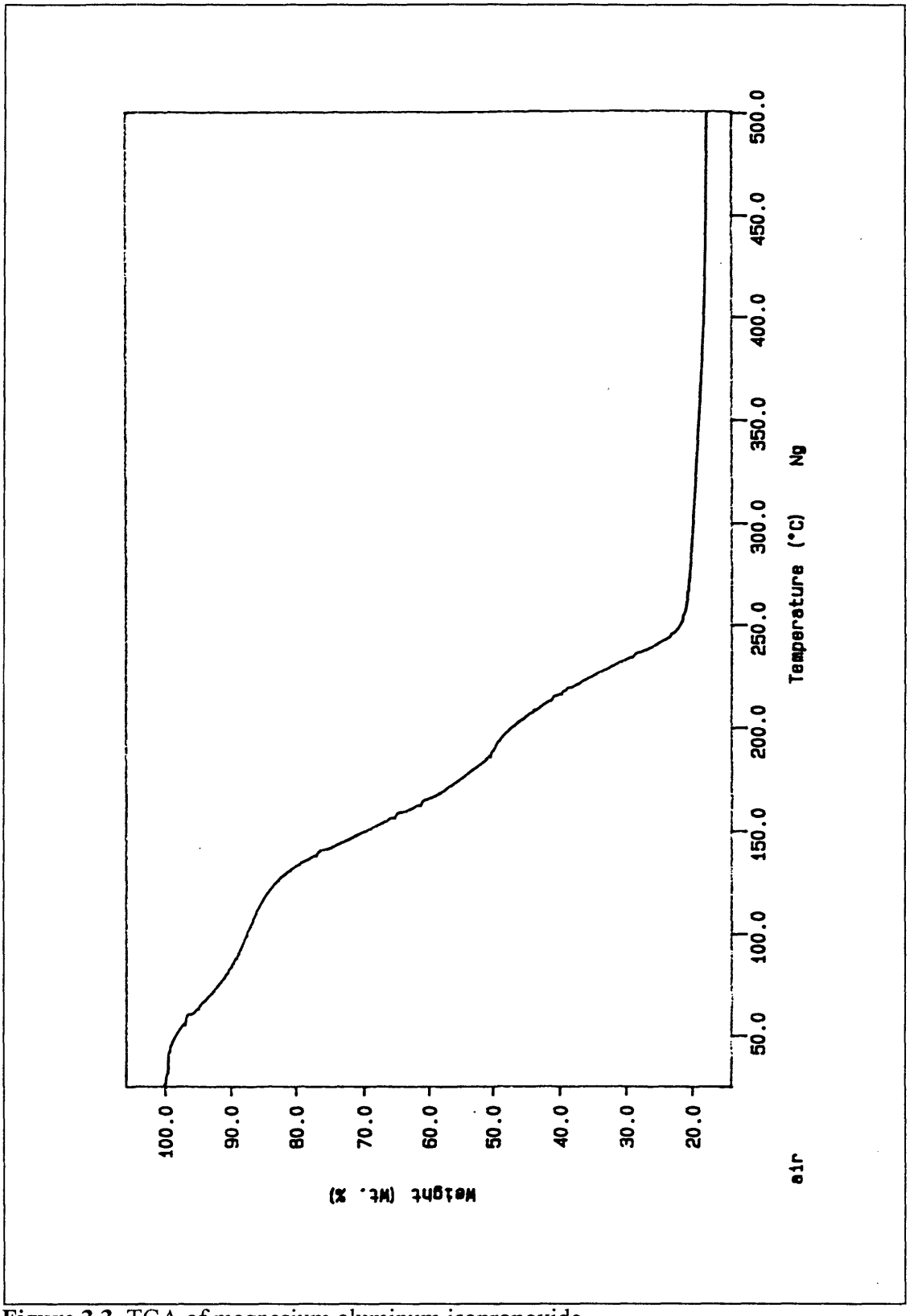

Figure 3.3 TGA of magnesium aluminum isopropoxide.

simultaneous water evaporation and any melting. The DTA curves, however, did not exhibit any distinct endotherm commonly associated with melting at 67°C.

The most likely explanation for the liquefaction, therefore, is that the mixed nitrates gave off and dissolved in their own water at 67°C. The cooled samples would not melt again once the water had evaporated. Aluminum nitrate was reported to dissolve in its own water of crystallization (Messing, 1993). This type of dissolution was also observed in other hydrated metal salts (Rillings, 1974).

Table 3.1 Liquefaction Temperature of Magnesium-aluminum Nitrate Powder

mol. % Al-nitrate	mol. % Mg-nitrate	liquefaction temperature
100	0	74°C
80	20	67°C
66.7	33.3	67°C
60	40	67°C
40	60	67°C
20	80	67°C
0	100	89°C

A stable, dehydrated form of aluminum nitrate could not be produced even by vacuum heating. The aluminum nitrate decomposed at as low as 55°C when partially deprived of its water of hydration. This suggested that dehydrated aluminum nitrate was unstable and decomposed at lower temperatures than would be if the atmosphere was dry. Aluminum nitrate decomposed at different rates depending on the pyrolysis atmosphere. Table 3.2 lists the cummulative amount of weight loss of aluminum nitrate at different temperatures in DTA experiments performed in both dry and humid oxygen atmospheres. The cumulative weight loss in a humid atmosphere was lower than that in a dry atmosphere until at approximately 140°C. The cumulative weight loss were very similar in both atmospheres above 140°C. It appeared that at low temperatures, the moisture in atmosphere slowed down the decomposition of aluminum nitrate until shortly before 140°C when the decomposition could not be retarded. The DTA curves of both dry and humid atmospheres had very similar trends despite the different rates.

The pyrolysis atmosphere hardly influenced the decomposition rate or path of magnesium nitrate. Dehydrated magnesium nitrate was successfully made. Evidence of melting was not observed for the dehydrated magnesium nitrate from the DTA data. The dehydrated magnesium nitrate did not melt at 89°C in the capillary tube melting experiment. This showed that magnesium nitrate decomposed by first giving off the water molecules. The dehydrated magnesium nitrate was stable and decomposed at higher temperatures.

Table 3.2 Cummulative Weight Loss of Aluminum Nitrate at Various Stages of Decomposition

Temperature	% Wt. loss in wet oxygen	% Wt. loss in dry oxygen
100°C	1.8	3.3
110°C	3.6	5.9
120°C	6.8	11.8
130°C	10.7	17.7
140°C	28.3	28.2
180°C	68.5	67.1
200°C	71.1	72.8

The pyrolyzed products of mixed magnesium-aluminum nitrates were examined by XRD. The mixed nitrates powders retained the individual identities of magnesium nitrate and aluminum nitrate at room temperature. The XRD pattern of the mixed nitrates after a 2 h annealing at 200°C showed that aluminum nitrate part had decomposed into an amorphous phase while the magnesium nitrate part remained stable and crystalline. The observation that aluminum nitrate decomposed at much lower temperatures is consistent with the section explained earlier. XRD patterns of the partially pyrolyzed magnesium-aluminum nitrate showed that magnesium nitrate remained stable at as high as 300°C but decomposed at below 400°C in an oxygen atmosphere. The entire mixture became amorphous after a 2 h annealing at 400°C. Mixed nitrates annealed for 2 h at 600°C remained amorphous.

For the individual nitrates, magnesium nitrate probably first decomposed into $Mg(NO_2)_2$ and then to amorphous MgO, as the weight loss data suggested (Fig. 3.4).

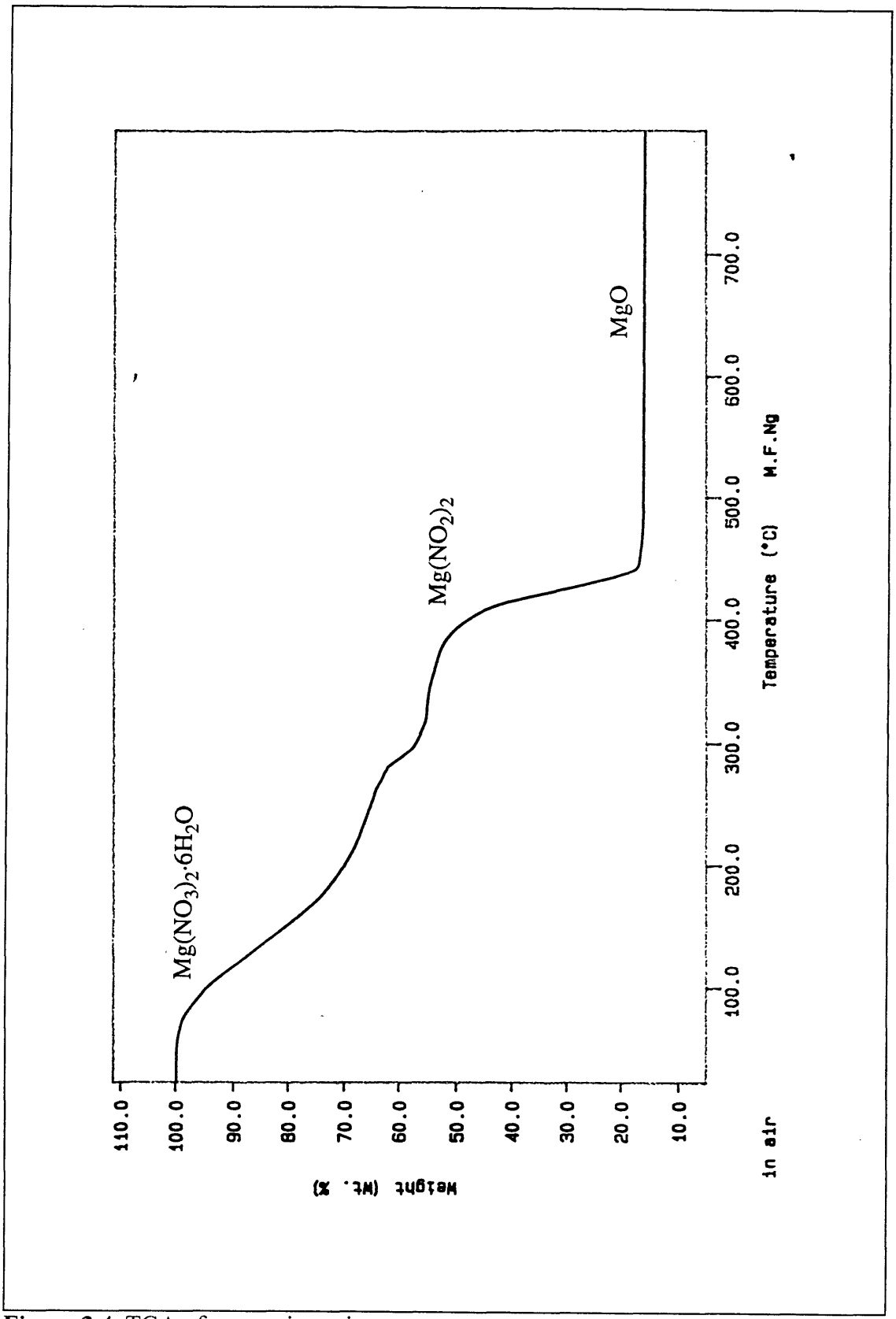

Figure 3.4 TGA of magnesium nitrate.

The weight loss of magnesium nitrate completed at 500°C. The following reactions were confirmed in literature (Oza, 1965).

$$Mg(NO_3)_2 \rightarrow Mg(NO_2)_2 + O_2 \quad (3.2)$$

$$Mg(NO_2)_2 \rightarrow MgO + NO_2 + NO \quad (3.3)$$

TGA data showed that by 500°C most of the weight loss of aluminum nitrate stopped. There was a small amount of weight loss that occurred at higher temperatures. The XRD patterns suggested that aluminum nitrate decomposed into an amorphous material. Hydroxyl absorption bands were observed in DRIFTS spectrum obtained from aluminum nitrate powders heated for 2 h at 500°C. The most likely explanation is that aluminum nitrate decomposed first into AlO(OH) and then the AlO(OH) decomposed slowly into Al_2O_3. These observations were consistent with other published data (Funaki, 1959).

The calcined powder pellets (mixed or individual nitrates) did not show any evidence of liquid formation at high temperatures. There was no endotherms observed in the DTA curves. Neither was there any shape distortion in the pressed pellets annealed at higher temperatures.

3.3.3 Lanthanum-Aluminum Nitrates

The "eutectic" melting phenomenon was also observed in lanthanum-aluminum nitrates. Liquefaction of the mixed nitrate powders, as observed from the nitrate powders in capillary tubes, started at 70°C. This temperature was very consistent regardless of the lanthanum nitrate to aluminum nitrate ratio in the mixture. Again this melting could not be reproduced once the same powder had been cooled and re-heated. The DTA curves did not exhibit any distinct endotherm commonly associated with melting. The liquefaction can similarly be attributed to the nitrates giving off and dissolving in their own water at 70°C as in the case of magnesium-aluminum nitrates.

The TGA data of the lanthanum nitrate decomposition showed that there was no weight loss above 620°C. This finding contradicts a published report that it required up to 780°C to decompose lanthanum nitrate into La_2O_3 (Wendlandt, 1956). It will be shown in Chapter 6 that $LaAlO_3$ can be formed in temperature much lower than 780°C. Lanthanum nitrate, therefore, must decompose at temperatures much lower than 780°C. The discrepancy between these decomposition temperatures may be attributed to the different atmospheres used in heating. Dry, flowing atmosphere was used in this study;

whereas the heating atmosphere in Wendlandt's study was not specified. The XRD spectra showed that lanthanum-aluminum nitrates decompose into an amorphous mixture at low temperature and remains amorphous up to 600°C.

3.4 SUMMARY

The decomposition routes of the precursors are examined in this chapter. The information obtained will be used to design the heat treatments for the precurors. The precursor decomposition routes found in this chapter largely agree with the information available in literature. The precursors decompose into solid amorphous mixture of oxides prior to the formation of crystalline phases. One interesting finding is that the mixed nitrates liquefy at lower temperatures than would be for the individual nitrates. Another new finding is the dependence of decomposition rate on the humidity of the pyrolysis atmosphere. These two findings will be used to design the proper heat treatements for the chemically derived films.

CHAPTER 4
SURFACE FEATURES OF CHEMICALLY DERIVED FILMS

4.1 INTRODUCTION

Some of the common criticisms on chemically derived films are their rough surfaces and high densities of pin-hole and cracking. These defects are caused by the volume change as the precursors decompose and crystallize into the desired phases. Rough surfaces will inevitably affect the qualities of the subsequently deposited BYC films. Cracks and pin-holes will lead to shorting between BYC layers. These physical defects must be eliminated if the films are to be used as insulating layers. Therefore, part of this thesis concentrates on the influence of processing parameters on the physical integrity of the films.

This chapter examines the processing conditions used and their effects on the surface features such as pits, cracks, and roughness. The emphasis is on the nitrates-derived films. This is the first time that smooth and crack-free spin-on spinel and $LaAlO_3$ films are produced from chemical precursors. A technique of using a humid atmosphere to eliminate cracking in the spinel films from nitrates is also discussed.

4.2 EXPERIMENTAL PROCEDURE

4.2.1 Substrates Preparation

Substrates used in this study were single-crystal yttrium-stabilized zirconia (YSZ), $SrTiO_3$, $MgAl_2O_4$, $LaAlO_3$, and MgO substrates. The results discussed in this chapter are for films on $SrTiO_3$ substrates unless otherwise specified. The as-received $SrTiO_3$, MgO, and $MgAl_2O_4$ substrates were 0.25" by 0.25" by 0.02" thick with one side polished. The $LaAlO_3$ substrates were diced in the same dimensions from large $LaAlO_3$ wafers (polished both sides) by a wire saw. All substrates were cleaned with a 15 min of ultrasonication in chloroform, followed by 15 min in acetone and 15 min in methanol. The substrates were quickly transferred from one solvent to another to avoid any drying of solvent and subsequent deposition of undesired materials. They were wiped dry with Kimwipes immediately after removal from the methanol bath. They were cleaned once more by methanol and dried with Kimwipes in a laminar flow hood before spin-coating. The surfaces were inspected under an optical microscope at 36.7 X magnification to ensure that no dust particles were left on the surface.

4.2.2 Making Films from Solutions

The magnesium aluminum isopropoxide was diluted in either a 5:1 or a 11:1 dried isopropanol:alkoxide ratio in a dry box. The solutions were filtered with a 0.22 μm ceramic tip filter to eliminate any large particles in the solution. The solutions were spin-coated on (100) silicon, (100) $LaAlO_3$ and (100) $SrTiO_3$ substrates inside a dry box. The spin coating time was 120 s. Different spinning rates were used to obtain different final film thicknesses. The as-spun films were transported to a tube furnace which had been attached to the dry box and filled with dry nitrogen without exposure to the outside atmosphere. The furnace was switched to either dry oxygen or nitrogen gas for about 30 min before pyrolysis. The precursor films were first heated in moist atmosphere for hydrolysis and then pyrolyzed in a dry atmosphere. The moist atmosphere was produced by first letting the furnace gas bubble through a 3 liter flask full of water, as described in Chapter 3. Spinel films were first hydrolyzed with the heating schedule illustrated in Figure 4.1. The heating schedule was designed from the TGA data to ramp up slowly at the early stage to minimize the chance of crack formation during the segment with the greatest volume change. The films were stable enough to be taken out of the furnace once they had been hydrolyzed into oxide (or even hydroxide). Then they were calcined at higher temperatures in a dry oxygen atmosphere.

The nitrate solutions were also filtered with a 0.22 μm ceramic tip filter to eliminate any particle from the solution. The solutions were spin-coated on planar (100) YSZ, (100) $LaAlO_3$, (100) $SrTiO_3$, (100) MgO, and (100) $MgAl_2O_4$ substrates inside a dry box with a dry nitrogen atmosphere. A dry atmosphere was needed to avoid dewetting the as-spun films. Different spinning rates were used for to obtain different film thicknesses with the spin coating time maintained at 120 s. The as-spun films were transported to a tube furnace which had been attached to the dry box and filled with dry nitrogen without exposing to atmosphere. The furnace was switched to dry oxygen gas for about 30 min before pyrolysis. A segment of heating with humid atmosphere was produced by first letting the furnace gas bubble through a 3 liter flask full of water before the gas entered the furnace. The relative humidity of the gas was slightly > 80% at room temperature. The heating schedules are shown in Figs. 4.2 & 4.3.

The heating schedules for films with were designed from the information obtained in Chapter 3 to accommodate the volume change in precursor decomposition. The molar volume of the molten magnesium-aluminum nitrates is approximately 230 cm^3

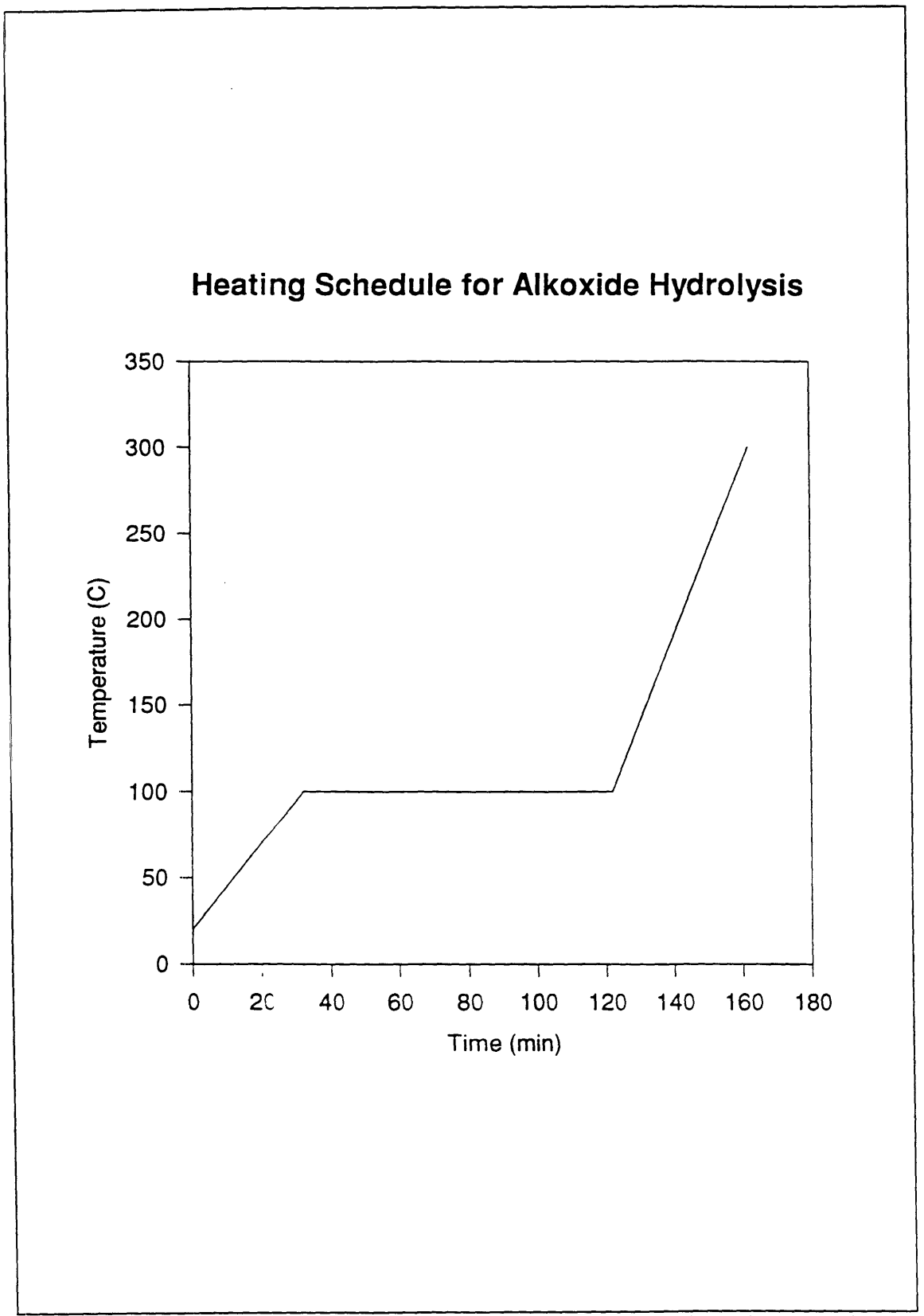

Figure 4.1 Heating schedule used to hydrolyze magnesium aluminum isopropoxide.

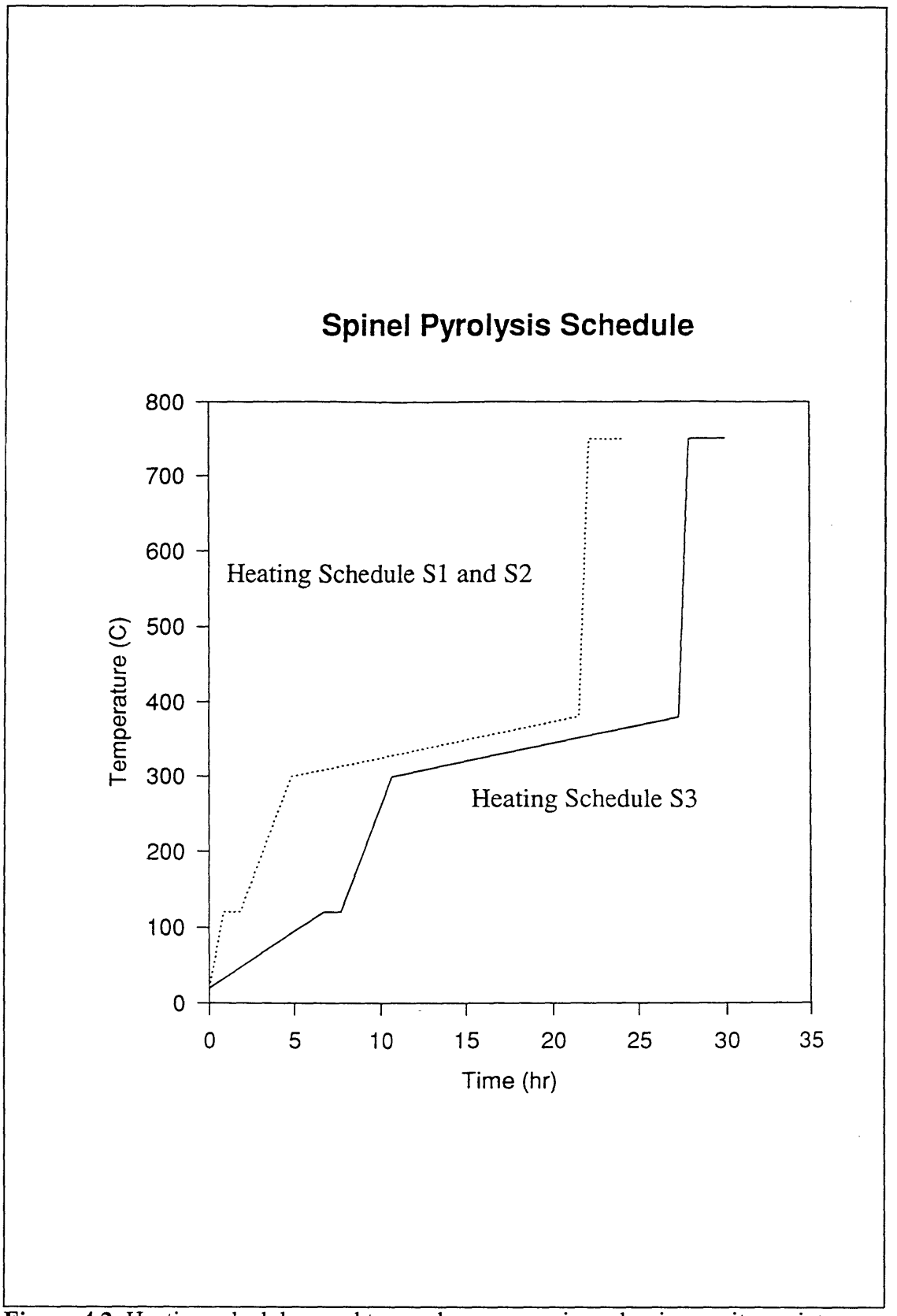

Figure 4.2 Heating schedules used to pyrolyze magnesium-aluminum nitrates into spinel (a) S1, S2, and S3.

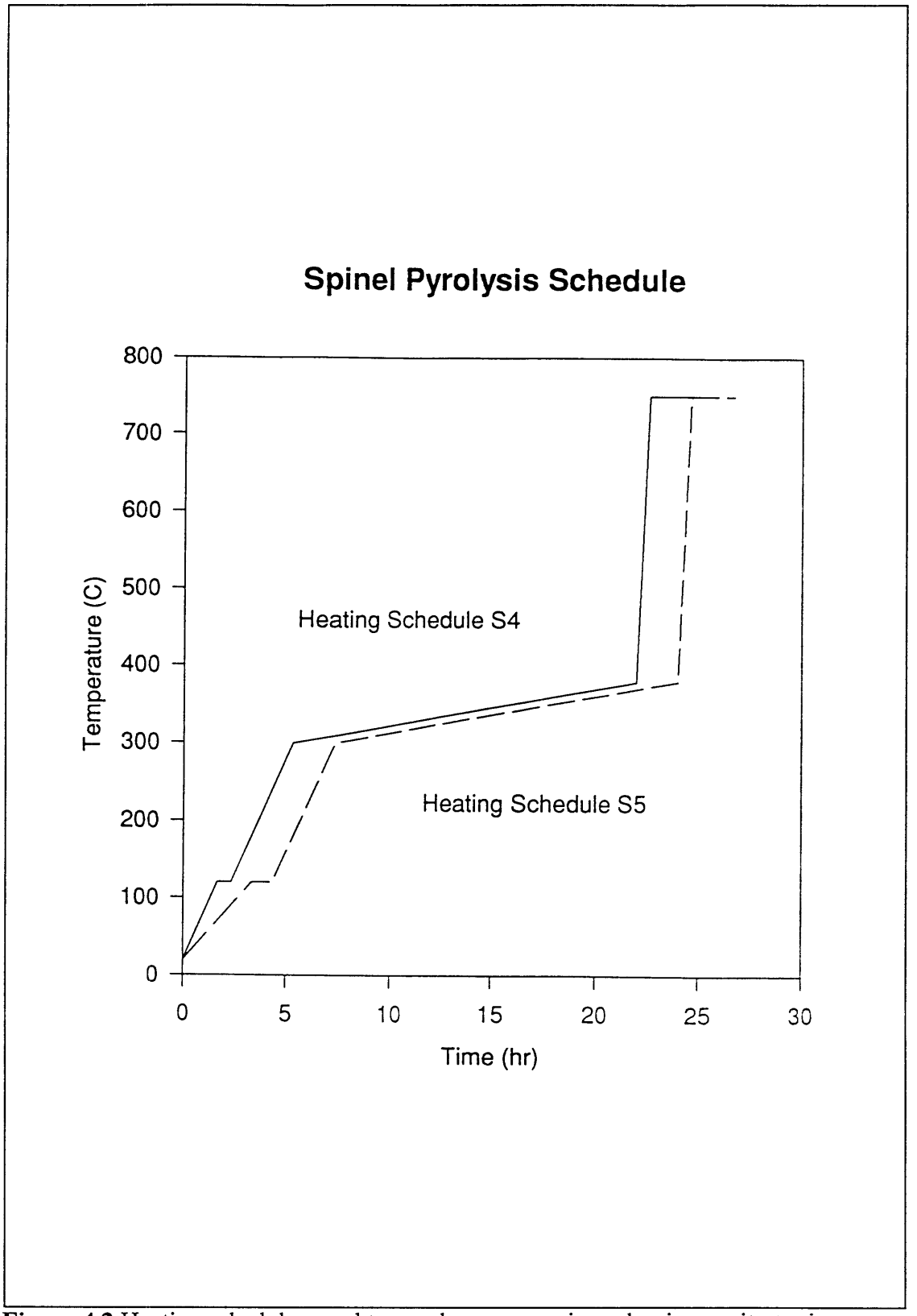

Figure 4.2 Heating schedules used to pyrolyze magnesium-aluminum nitrates into spinel (b) S4 and S5.

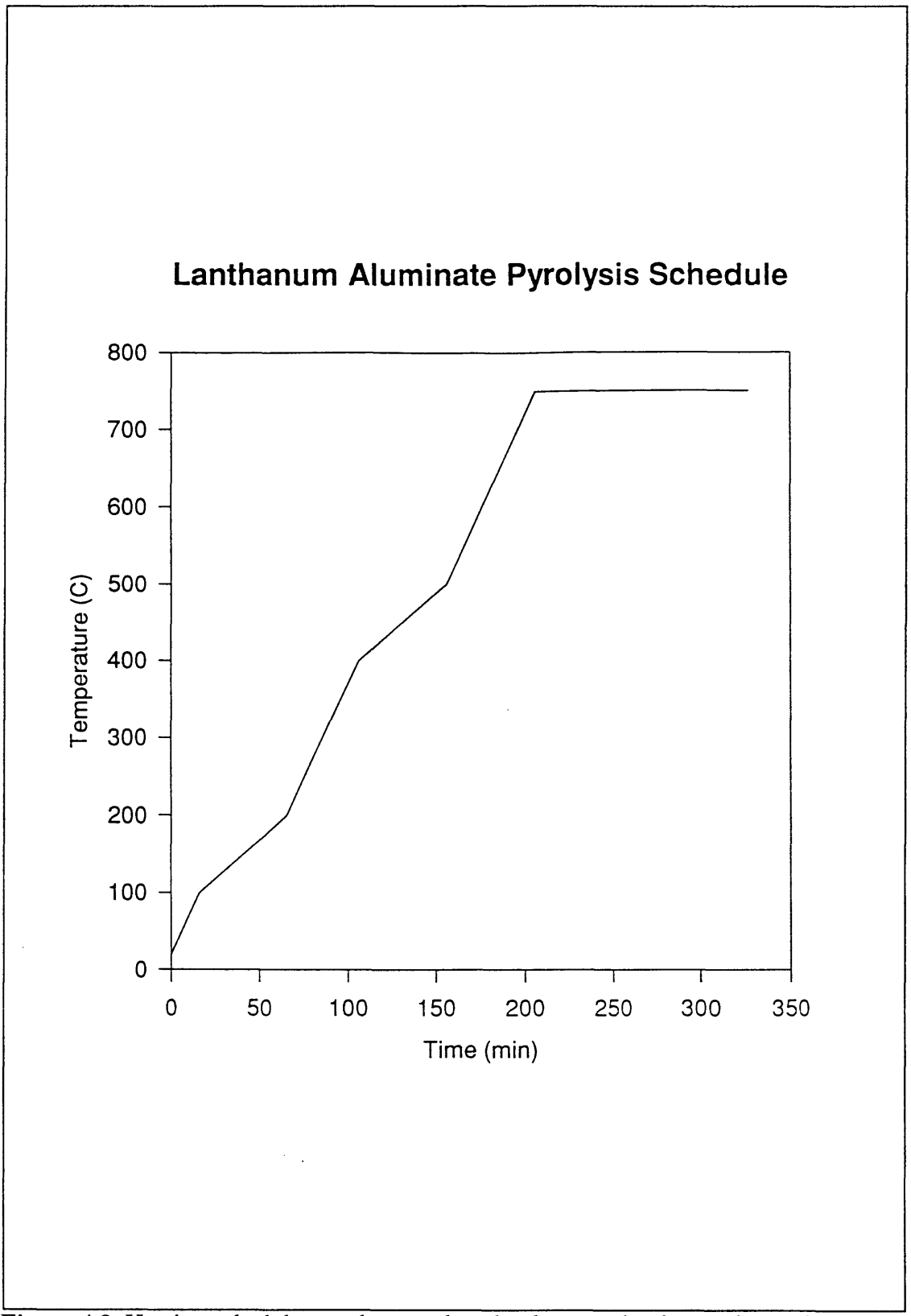

Figure 4.3 Heating schedules used to pyrolyze lanthanum-aluminum nitrates into $LaAlO_3$.

(Ramana, 1985). Spinel has a molar volume of only 37 cm^3, which is only 16% of the original volume. The TGA data suggest there are two major decomposition segments. The first one in the early part of heating is the removal of the water of hydration of both aluminum and magnesium nitrates. The second major weight loss segment is the decomposition of magnesium nitrate between 300°C and 400°C. The aluminum nitrate portion has already decomposed into a solid phase by that temperature range. Thus, the heating schedules (Fig. 4.2) were designed to allow for the volume change during the two segments of major weight loss. Some nitrates-derived spinel films were fired in a nitrogen atmosphere with a boat of methanol inside the tube furnace to provide a partial methanol atmosphere at the early stage of pyrolysis.

The heating schedule shown in Figure 4.3 for $LaAlO_3$ films was designed to have two slow segments to accommodate the major decomposition stages of aluminum nitrate and lanthanum nitrate.

4.2.3 Surface Characterization

The surface features of the films were examined by scanning electron microscopy (SEM) and atomic force microscopy (AFM). SEM samples were first sputtered with a thin layer of gold to avoid charging. Samples for AFM were analyzed without any coating. The average surface roughness measurements were made over an area of 25 μm^2 by AFM. The measurements were done using a tapping mode method in which a silicon cantilever scanned the surface.

4.3 SURFACE MORPHOLOGY

4.3.1 Spinel Films from Magnesium Aluminum Isopropoxide

A small number of cracks were formed after calcination at 800°C for films using a precursor solution with a magnesium aluminum isopropoxide:isopropanol ratio of 1:5. The thickness of these films were approximately 0.2 μm. A precursor with a magnesium aluminum isopropoxide:isopropanol ratio of 1:11 produced very smooth film surfaces with no cracks observed (Fig. 4.4) under the same heating schedule. These films were approximately 0.1 μm thick. The films were featureless. Figure 4.4a shows the few cracks near the edges of the samples. The edges of the films were inevitably much thicker than the rest of the film and produced cracks during pyrolysis of chemical precursors. The cracks, however, did not propagate into the rest of the film. Figure 4.4b shows the typical film surface, which was featureless.

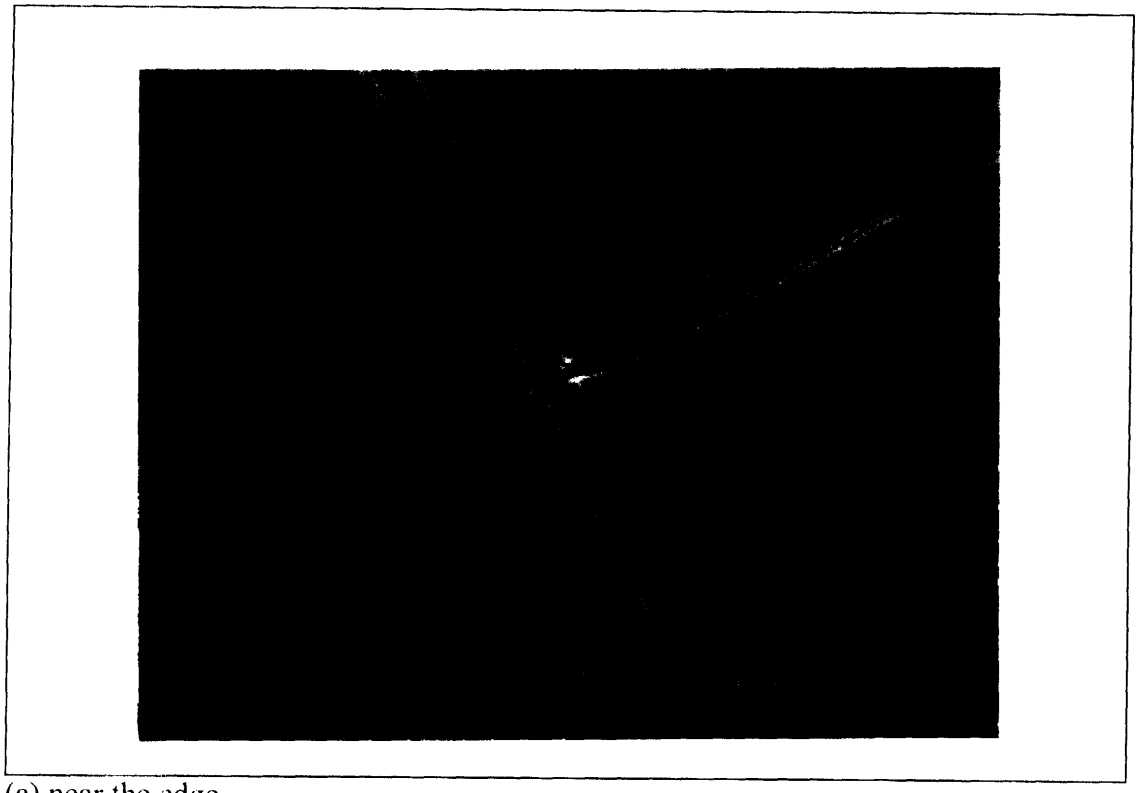

(a) near the edge

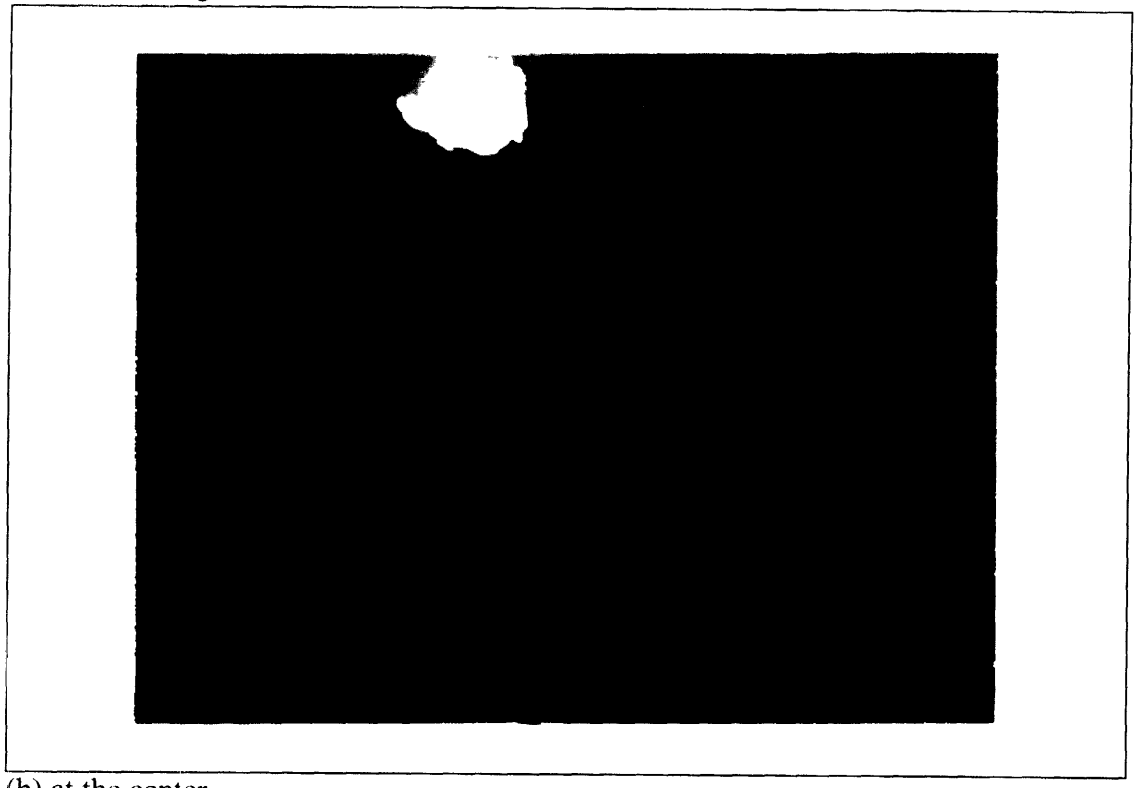

(b) at the center

Figure 4.4 SEM micrographs of a spinel film from magnesium aluminum isopropoxide.

The observations of cracking in the thicker alkoxide-derived films suggested that there was a critical cracking thickness (CCT) for the alkoxide-derived films under identical processing conditions. The CCT can be modeled as follows. The strain energy is caused by shrinkage of the precursor film due to volume change during decomposition. The precursor film can shrink in the thickness direction because there is no constraint. The film/substrate interface, however, introduces friction against shrinkage in the in-plane directions. This friction constrains the shrinkage and results in a biaxially tensile stress σ in the film. The strain energy U is proportional to the thickness of the film. Cracking can relieve the strain energy if the formation of crack is energetically favorable. Cracking will form new interface and that increase energy. For an elastic homogeneous system, the theoretical crack formation energy for thin film has been modeled (Hu, 1988). Let z be the crack depth illustrated in Figure 4.5. The strain energy release rate G is

$$G = 1.2\pi\sigma^2 z/E \tag{4.1}$$

where E is the Young's modulus of the film. The energy release rate is defined as

$$G = -\partial U/\partial A \tag{4.2}$$

where A is the crack area. The difference in the strain energy, ΔU, of a fully cracked film and an uncracked film of width l, can be expressed as

$$\Delta U = l \int_0^h G\, dz = 0.6\, \pi\sigma^2\, l\, h^2/E \tag{4.3}$$

Here ΔU is the strain energy difference between an element of thickness Δl in front of a crack growing along the film and a similar element in the crack wake. The steady-state energy release rate for crack extension along the film is

$$G = \Delta U/hl = 0.6\, \pi^2\, h/E \tag{4.4}$$

The stress intensity factor is

$$K = (EG)^{1/2} = 1.4\sigma h^{1/2} \tag{4.5}$$

The stress intensity factor is proportional to the square root of the thickness. This will lead to cracking when the thickness of the stressed film reached a critical value. This can why explain the cracking occurred in the thicker films and the thicker edge regions.

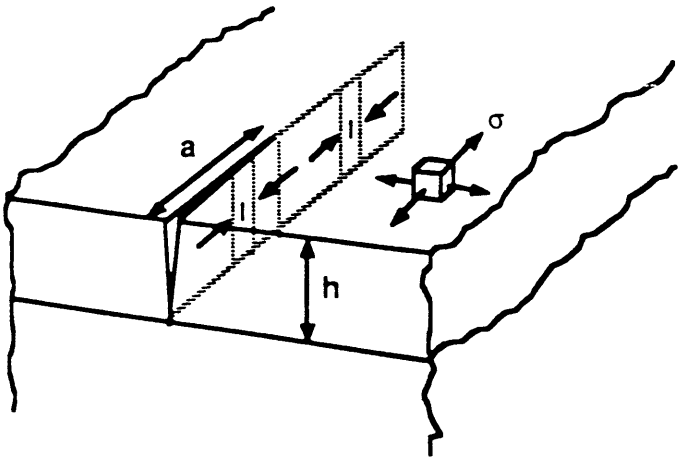

(a)

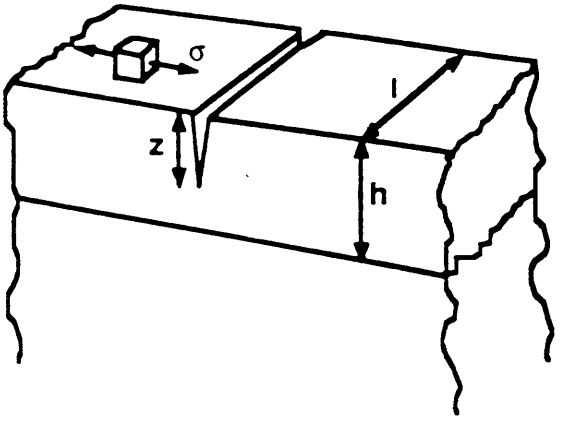

(b)

Figure 4.5 (a) A section of a crack extending through thin film, and (b) a steady-state film crack (Hu, 1988).

4.3.2 Spinel Films from Magnesium-Aluminum Nitrates

Nitrates-derived spinel films had thickness of approximately 0.1 μm when spun with a 0.35 osmolar methanol-based precursor solution with a spinning rate of 7000 rpm. Methanol-based solution produced thicker films than isopropanol-based. All films had cracking at the edge of the films. This is consistent with the analysis of critical cracking thickness mentioned earlier. Spinel films pyrolyzed with Heating Schedule S1 (Fig. 4.2a) exhibited circular cracks even though the overall film surfaces were smooth (Fig. 4.6a). These circular cracks were about 20 μm in diameter. Heating Schedule S2 (Fig. 4.2a) is identical to S1 except for a 10 min 120°C hold when moist oxygen (> 80% relative humidity) was introduced in the furnace. Introduction of moisture in the pyrolysis atmosphere eliminated those circular cracks (Fig. 4.6b). Heating Schedule S3 (Fig. 4.2a) is identical to Heating Schedule S1 except that the ramp rate from room temperature to 120°C is four times slower. Spinel films fired with Heating Schedule S3 also did not have circular cracks.

The role of the 10 min hold at 120°C with moist atmosphere in eliminating the circular cracks is worth investigating because it can reduce the overall processing time to achieve the same film qualities. One possible explanation is that moisture in the atmosphere decreased the decomposition rate of aluminum nitrate because dehydrated aluminum nitrate was very unstable and decomposed rapidly. This hypothesis was confirmed when crack-free films were produced with Heating Schedule S3 with only dry oxygen atmosphere throughout the pyrolysis. A slower heating rate from room temperature produced the same effect as a 10 min hold in moist atmosphere did.

Another experiment to prove the hypothesis was to observe a film produced with a faster rate at the beginning but still including a 10 min 120°C hold in moist atmosphere. It is very likely that the decomposition rate was the key to circular crack formation if that film still had circular cracks. A more rapid initial ramp, however, caused dewetting of the spin-on films instead. It is known that even atmospheric humidity causes dewetting of the as-spun films. It has been shown in the previous section that the nitrates precursors dissolved in its own water at approximately 67°C. A fast heating rate in the beginning did not allow the water to evaporate fast enough. The excess water caused the film to dewet. This suggested that the early heating rate/atmosphere is critical in the resultant film morphologies.

DTA results mentioned in Chapter 3 provided another piece of evidence that moisture in the pyrolysis atmosphere reduced the decomposition rate. The general shapes of the DTA curves were very similar for the nitrates precursors in either dry or

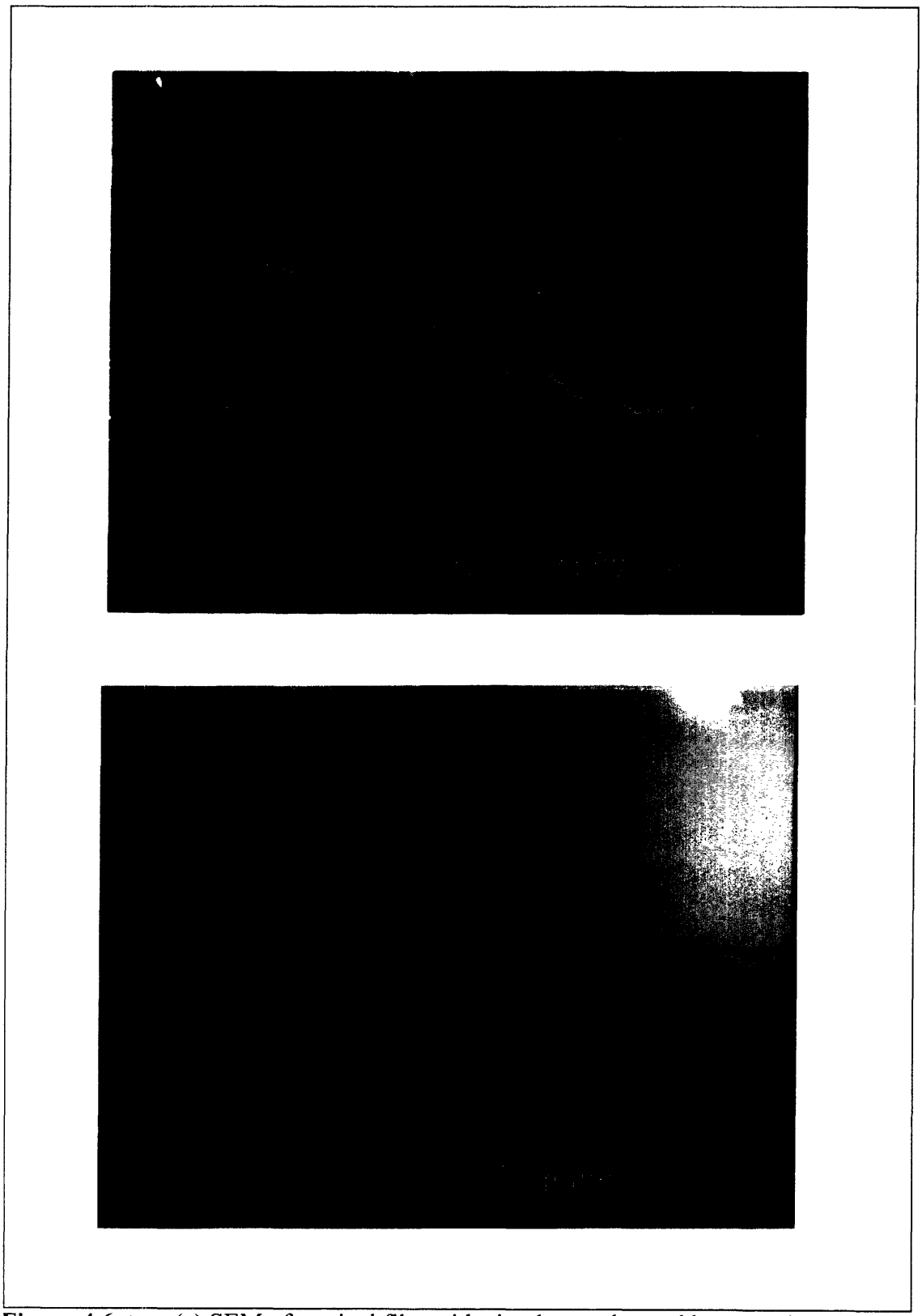

Figure 4.6 top: (a) SEM of a spinel film with circular cracks, and bottom: (b) a film without circular cracks.

humid pyrolysis atmospheres. The decomposition path was not influenced by introduction of moisture in the atmosphere.

The other possible explanation is that the moisture in the atmosphere condensed on the surface and acted as a solvent and let the film maintains its molten form. The temperatures, however, may be too high to allow the water to condense. It was not probable that the mixed nitrates were in a liquid state at that temperature.

Lengthening or shortening other segments in the heating schedule did not affect on the presence of the circular cracking. (The slow heating segment between 300°C to 400°C, however, is needed for magnesium nitrate decomposition.) This indicated that the early stage of the heating is responsible for formation of circular cracks. Figure 4.7 shows the initial heating conditions in which circular cracking can be eliminated.

The elimination of cracking in nitrates-derived spinel films suggested that the films were viscoelastic at the early stage of decomposition. The fact that the decomposition rate causes cracking indicates that the cracking depends on the strain rate. A simple quantitative derivation is as follows. The film is assumed to be linear viscoelastic such that

$$E = E_0 \exp(-t/\tau) \text{ for } 0 \leq t \leq t_f \tag{4.6}$$

where E_0 and τ are constants. The shrinkage stops when time t reaches t_f. The stress necessary to maintain a strain ε is

$$\sigma = \varepsilon E_0 \exp(-t/\tau) \tag{4.7}$$

The strain rate s can be assumed as constant such that.

$$\varepsilon = s\, t \tag{4.8}$$

$$\sigma = \varepsilon E_0 \exp(-\varepsilon/s\tau) \tag{4.9}$$

Therefore, a decrease in the strain rate will lower the stress because of the exponential term. Combining this with Equation (4.5) gives

$$K = 1.4\, \varepsilon E_0 \exp(-\varepsilon/s\tau) h^{1/2} \tag{4.10}$$

Overall the cracking phenomenon is determined by the overall strain, the ramp rate, and the thickness.

The initial heating rate still influenced the surface roughness for films that were processed even with a humid atmosphere. AFM analyses of the surface of the spinel thin film produced by Heat Schedule S4 showed that the films had surface roughness of about 6 Å for a 25 μm^2 region (Fig. 4.8a). There were some pinhole-like features on the

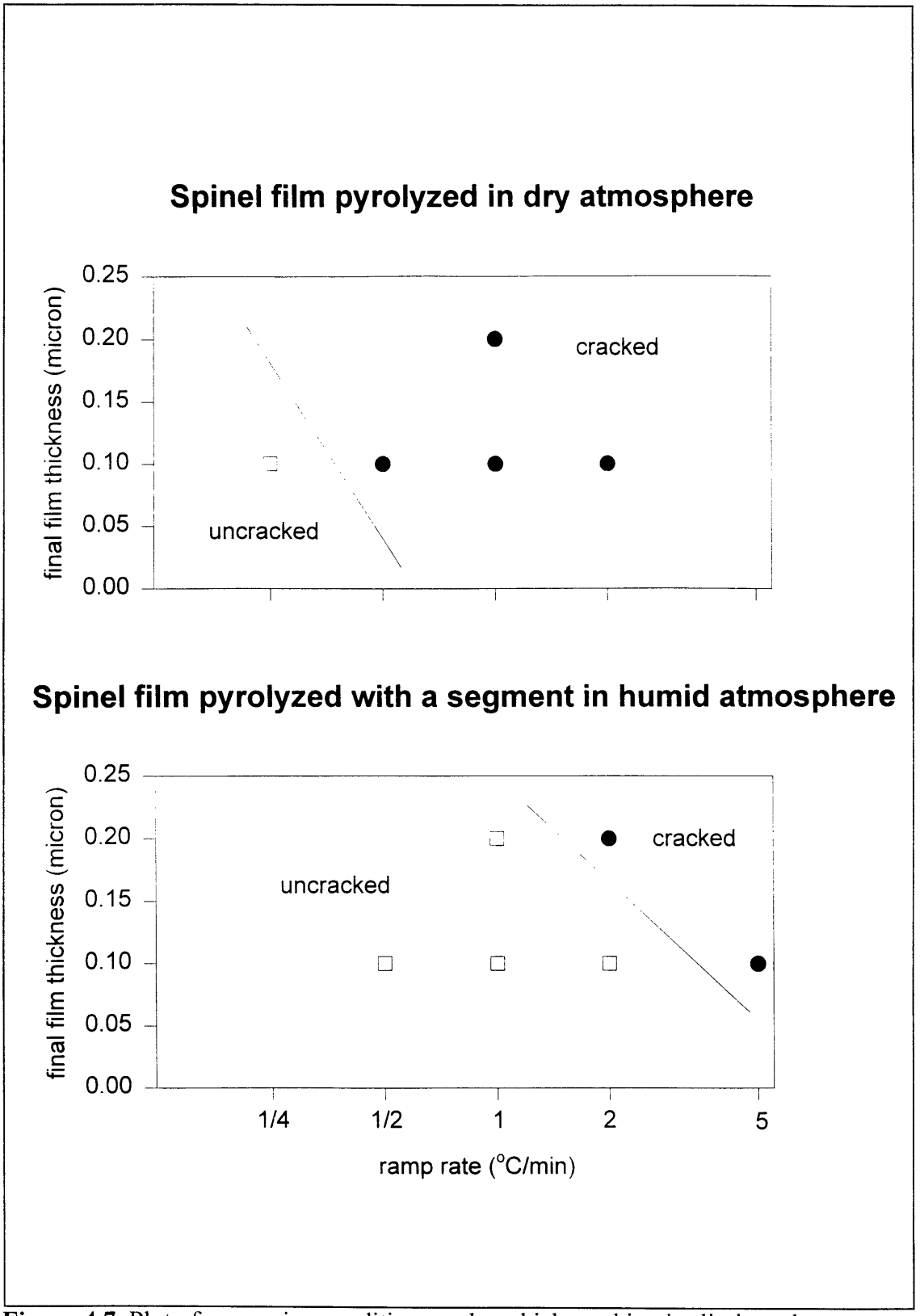

Figure 4.7 Plot of processing conditions under which cracking is eliminated.

surfaces despite the smoothness. Faster heating rate (Heating Schedule S5) greatly roughened the surface and caused formation of pits that are about 10 nm deep and 0.2 μm wide (Fig. 4.8b). It was believed that the longer ramp time allowed the gaseous products to diffuse out gradually without forming micro-blisters that result in pits.

Attempts were made to produce thicker films by using more concentrated solutions. A film spun from a diluted precursor solution normally retained a shiny surface even after spinel formation. Films spun from a more concentrated precursor solution quickly wrinkled immediately after spin-coating. The resultant films also had very rough surfaces observable without magnification. Attempts to smooth the as-spun surfaces were made by keeping a methanol environment near the spin-coater. The wrinkled surfaces quickly regained their smoothness. Yet they wrinkled again once they had been removed from the methanol vapor environment. Attempts were made to improve the smoothness by putting a boat of methanol inside the tube furnace and firing the films in nitrogen at the beginning. It was hoped that the methanol vapor would keep the films from wrinkling until they had decomposed. The resultant films were not as good as the films spun from diluted precursor solutions even though the resultant films were still smoother than without methanol vapor. This indicated that the drying of the solvent can as well be an important processing condition affecting the surface features of the films.

4.3.3 Lanthanum Aluminate Films

Films were made using a solution of 0.25 osmolar in methanol with a spinning rate of 7000 rpm. The thickness was approximately 1000 Å. The overall $LaAlO_3$ film surfaces were also smooth and crack-free (Fig. 4.9). Cracking was observed at the thicker edge of the films, as in the spinel films. The surface roughness of films produced by different heating rates were measured by AFM. These films were held for 2 h at 750°C. The average surface roughness of a film that took 1 hour and 13 minutes to reach 750°C was 7 Å in a 25 μm^2 area. The average surface roughness was approximately 9 Å when the total ramp time was to 3 h 25 min. The roughness increased to approximately 12 Å when the ramp time was 29 h 47 min. The surface roughness of a multiple-coating film could be as high as 30 Å. The general trend was that longer heating caused rougher surfaces. This could be due to shorter time at higher temperature to reduce the coarsening of the surface of the films. There was no recognizable pattern in surfaces, i.e., oriented surface step or twinning as observed in single-crystal substrates. For comparison, an as-received single-crystal $LaAlO_3$

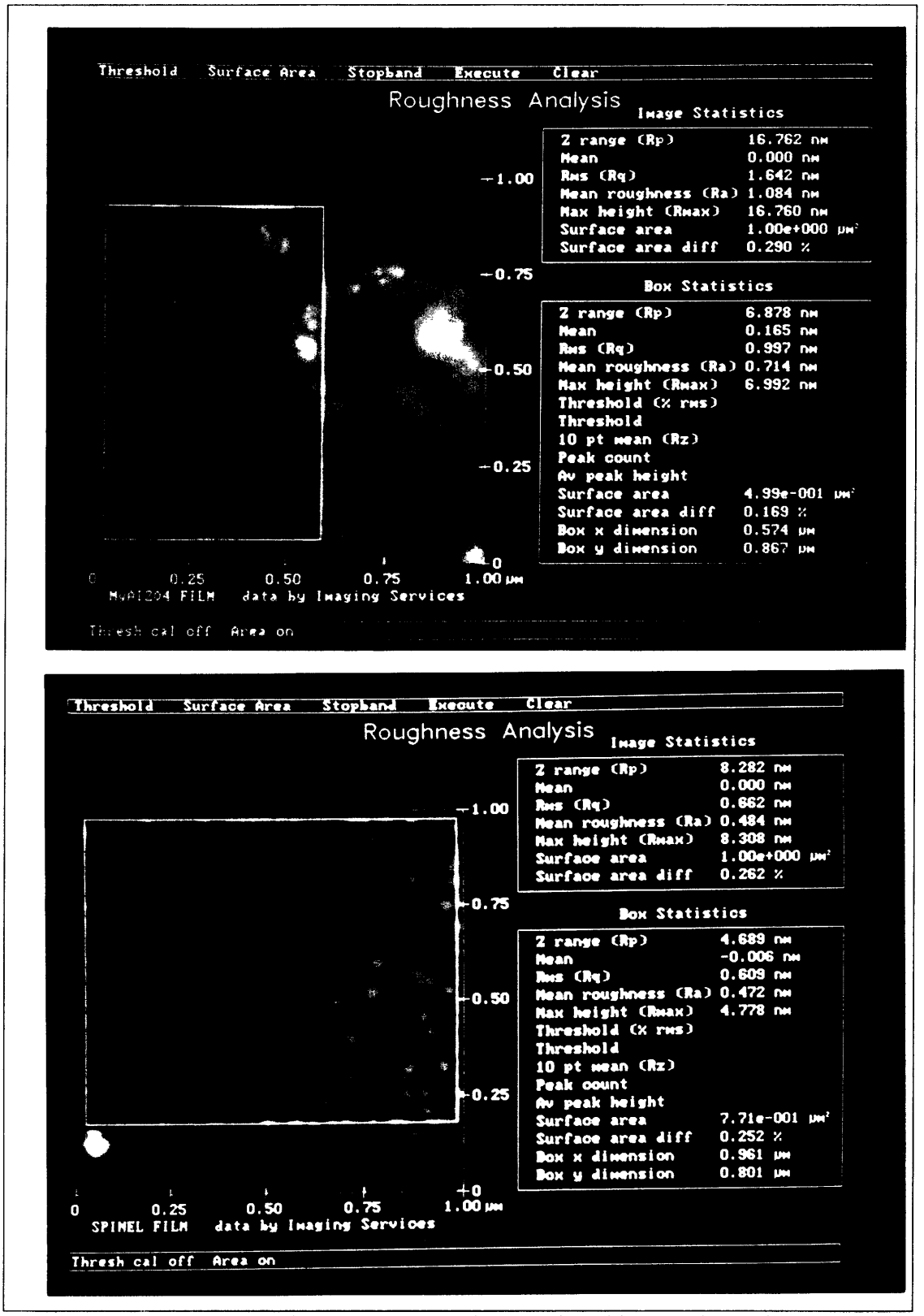

Figure 4.8 top: (a) AFM of a spinel film surface produced by Heating Schedule S4, and bottom: (b) by Heating Schedule S5.

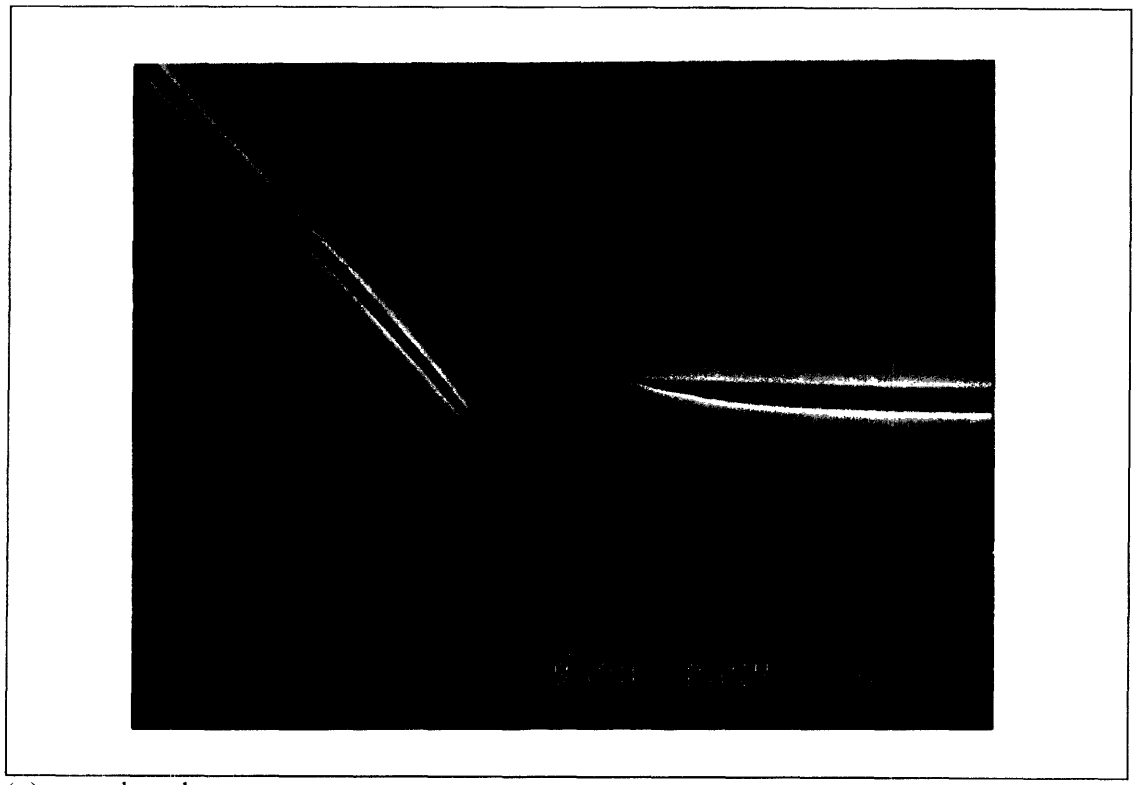

(a) near the edge

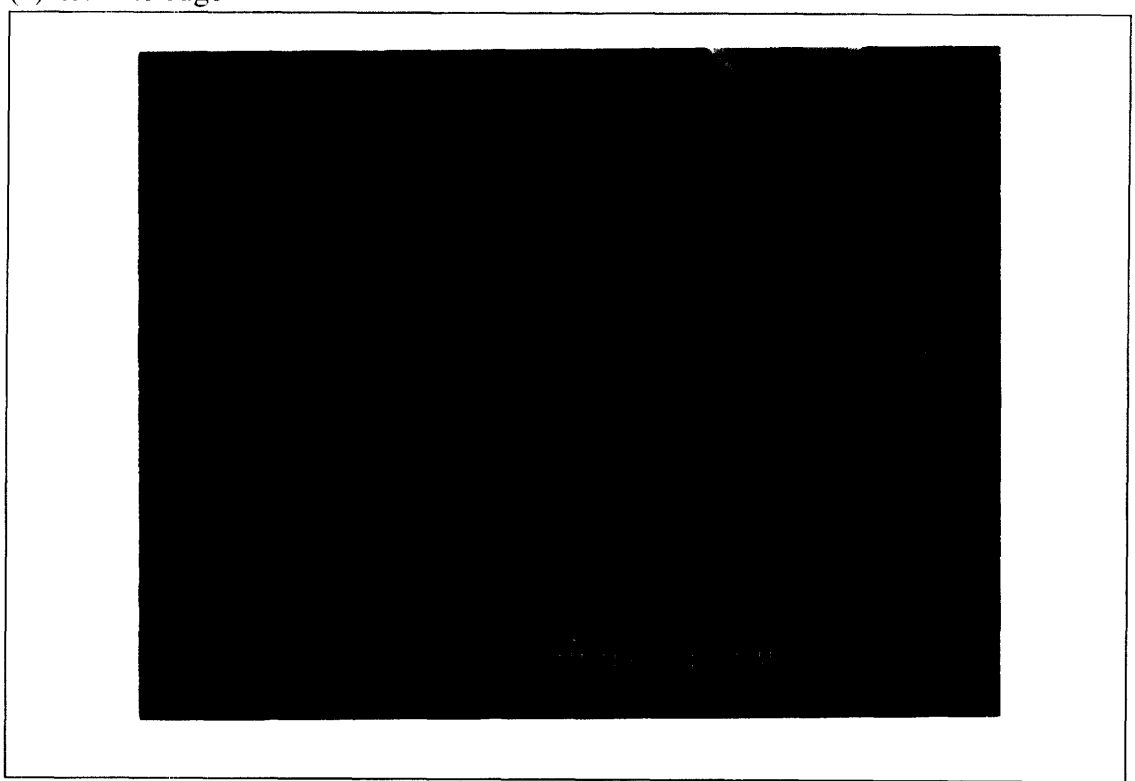

(b) at the center

Figure 4.9 SEM micrographs of a $LaAlO_3$ film annealed at 750°C for 2 h.

substrate had an average surface roughness of less than 1 Å but had twinnings observable without magnification.

4.4 SUMMARY

Pyrolysis conditions have been designed to produce crack-free and smooth films in spite of the huge volume shrinkage in precursor decomposition. The two major factors that control the cracking are the thickness and the decompostion rate. Dehydrated aluminum nitrate decomposes too rapidly and causes circular cracks in the nitrates-derived spinel films when pyrolyzed in a dry atmosphere. Instead of using the conventional method of reducing the ramp rate, a new method is used. The precursors are pyrolyzed in a humid atmosphere to decrease the effective decomposition rate. The overall processing can be reduced significantly. The average surface roughness of the chemically derived films can be as low as 6 Å and 7 Å for spinel and $LaAlO_3$, respectively.

CHAPTER 5
CRYSTALLOGRAPHY OF THE SPIN-ON FILMS

5.1 INTRODUCTION

One concern about mixed nitrate precursors (or other mixed metal salt precursors) is the potential segregation of the different cationic species during decomposition and crystallization. Segregation will lead to formation of undesired phases. This will be disastrous for multi-cation films. This study proves that multi-cation oxide films can be deposited from mixed nitrate precursors without any evidence of segregation. This chapter examines the crystallographic properties of the chemically derived films, particularly on the nitrates-derived films. The film microstructures, porosity, and orientations are discussed.

5.2 CHARACTERIZATION

5.2.1 X-ray Diffraction

The crystallinity and the in-plane orientation of the films were studied by normal powder, rocking curve, and pole figure XRD techniques. Basically the same $\theta/2\theta$ setup as in powder samples described in Chapter 4 was used for thin-film samples. The only difference was an addition RSM slit of 0.3 mm inserted in front of the detector to eliminate the erroneous substrate peaks. The texture of the films was measured by rocking curve XRD. The 2θ angle in rocking curve was kept constant but the θ angle was varied. A Rigaku RU-200 diffractometer was used for the pole figure XRD setup to determine the in-plane orientation. The (311) plane of spinel was chosen for pole figure because of the absence of (311) reflection from the substrate. No pole figure experiment was performed on the $LaAlO_3$ films because of the close proximity between the film diffraction peaks and the substrate diffraction peaks. The pole figure measurement was taken with a dwell time of 1 s. The Cu K_α radiation was generated with an accelerating voltage of 50 kV and a current of 200 mA.

5.2.2 Transmission Electron Microscopy

Plan-view transmission electron microscopy (TEM) specimens were made by cutting a small piece of the film sample. The film side of the sample was glued with M-

Bond 610 to a copper TEM grid with a 800 μm diameter aperture. The glued specimen was cured at 140°C for 2 h. The TEM sample was mounted on a tripod polisher to ensure a parallel polishing surface once the glue had been set. It was mechanically polished down to approximately 50 μm thick with a 3 μm finish. It was then dimpled with 3 μm diamond slurry to a thickness of about 5-10 μm. The dimpled region was ion milled from the substrate side at an accelerating voltage of 5 kV while rotating until perforation. A final, brief ion milling on from both the film and the substrate sides was performed to clean up any material re-deposited by the previous ion milling. Bright field TEM images were taken.

5.2.3 Optical Method

Attempts were made to measure the density of the films by comparing the index of refraction of the films with those of the bulk samples. The transmission spectra were measured by using uv-visible spectrophotometry. The indices of refraction can be calculated from the spectra (Weinstein, 1954). Films used in spectrophotometry were deposited on substrates polished on both sides for the incident light to transmit. Multilayer films were used because of the requirement for a minimum thickness of the film to observe the interference effect. The calculations and theories are presented in Appendix C.

5.3 FILM CRYSTALLINITY

5.3.1 Spinel Films from Alkoxide

XRD spectra for films produced from magnesium aluminate isopropoxide showed only the (100) spinel phase (Fig. 5.1). No other phase was detected by XRD. The FWHM of the rocking curve for the (400) spinel plane diffraction was approximately 1° θ. Pole figure XRD of the (311) plane confirmed the overall in-plane orientation (Fig. 5.2). Plan-view TEM micrograph of a spinel film on $SrTiO_3$ heated at 800°C for 2 h showed that there were pores range from 3 to 8 nm (Fig. 5.3). The SAD showed that the film was single-crystal like despite the presence of small pores. The appearance that the pores are the major phase was due to the projection of pores from different planes of depth. The SEM micrographs in Chapter 4 showed that the films were rather solid. More on the pore formation will be discussed later in this chapter.

The position of the (400) diffraction plane did not differ from those obtained in a standard powder sample. This indicated that the films were not noticeably strained. In

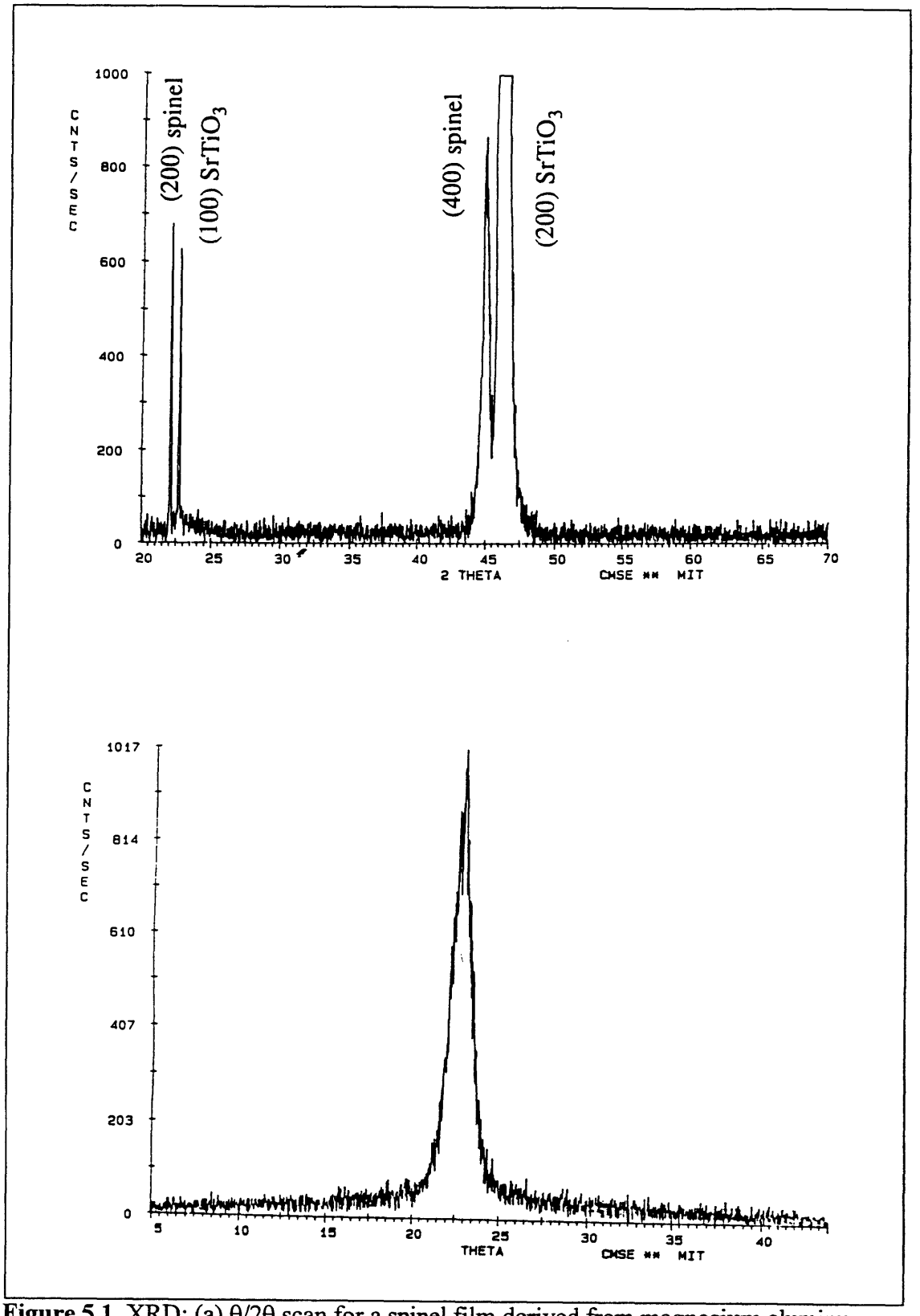

Figure 5.1 XRD: (a) θ/2θ scan for a spinel film derived from magnesium aluminum isopropoxide, and (b) (400) rocking curve of the same film.

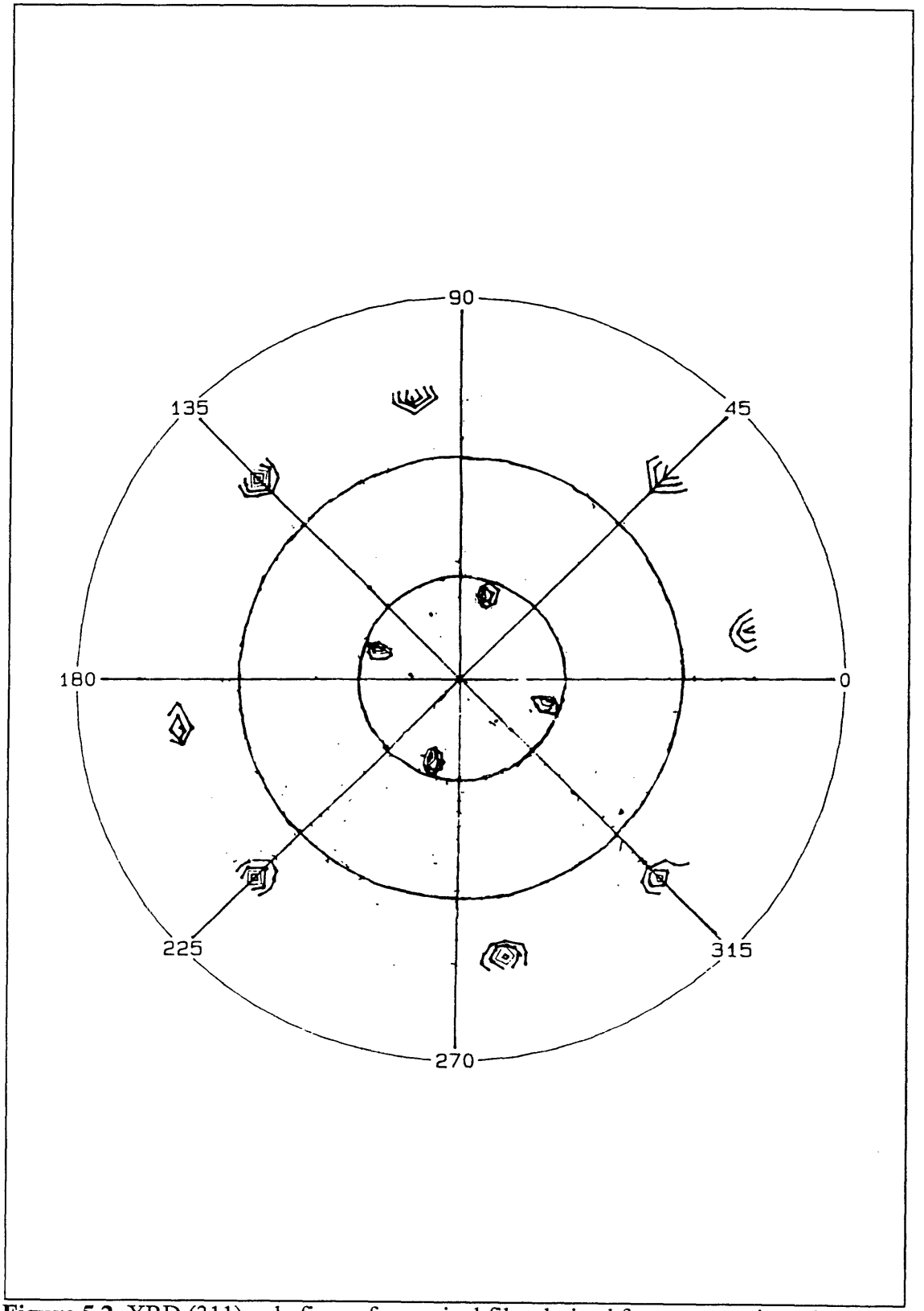

Figure 5.2 XRD (311) pole figure for a spinel film derived from magnesium aluminum isopropoxide.

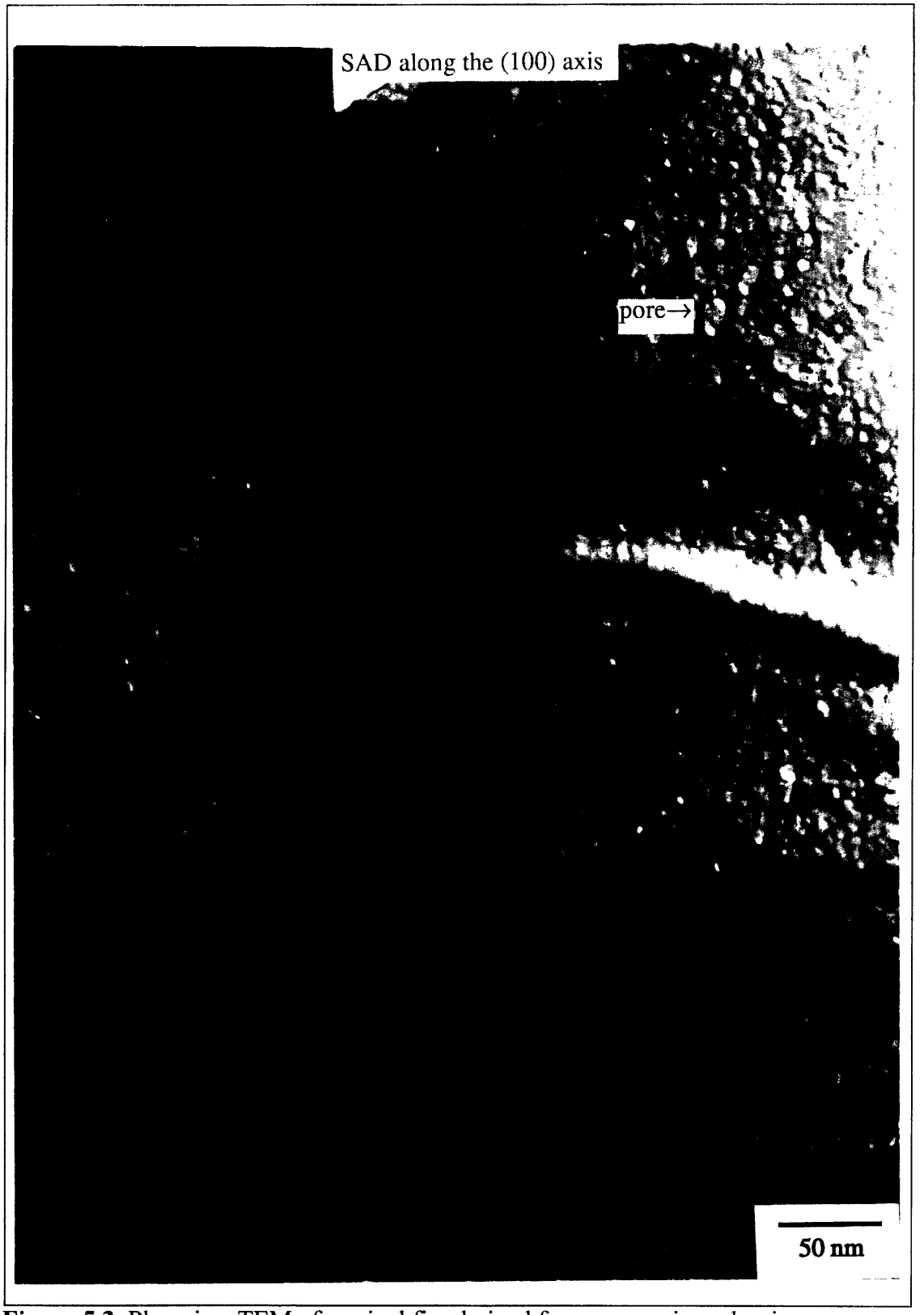

Figure 5.3 Plan view TEM of a spinel fim derived from magnesium aluminum isopropoxide.

heteroepitaxy the mismatch may produce strained films. It is not surprising that the films were not strained, however. The high elastic modules of ceramics make the stained films energetically unfavorable. Let f be defined as follows.

$$f = (a_s - a_0)/a_0 \tag{5.1}$$

where a_s and a_0 are the stress-free lattice parameters for substrate and film, respectively. These cubic films are biaxially stressed. The coherent strain energy E_c per unit area for cubic system films can be expresssed as

$$E_c = [2\, G_0\, (\, 1 + \nu\,)\, /\, (\, 1\text{-}\nu\,)]\, h\, \varepsilon^2 \tag{5.2}$$

where G_0 is the shear modulus of the film; ν is the Poisson's ration; h is the film thickness; and ε is the elastic strain (Matthews, 1979). The strain energy can be relieved by formation of dislocations. The unit area energy associated with dislocation dislocations E_d can be expressed as

$$E_d = [\ln (R/b) + 1]*[G_0 G_s (f\text{-}\varepsilon) b]/[\pi (G_0 + G_s)\, (1\text{-}\nu)] \tag{5.3}$$

where R is half the distance between dislocations; b is the Burger vector; and G_s is the shear modulus for the substrate. There is a critical thickness in which dislocations will form to relieve the strain. Because R cannot be determined from the micrographs, the critical thickness is not estimated in this study.

5.3.2 Spinel Films from Nitrates

The general crystallographic characteristics of spinel films derived from nitrates were very similar to those derived from magnesium aluminum isopropoxide. This section will describe the general characteristics of the films. The temperatures range for formation of the spinel phase will be discussed further in Chapter 6. XRD spectra for films produced from nitrates also showed only (100) spinel phase with no other phase detected. Normal strain was again not observed in the films. The FWHM of the rocking curve for the (400) spinel plane diffraction was approximately 1°θ, as in the alkoxide-derived spinel films. More on the nucleation and growth of the epitaxial films will be discussed in Chapter 6. The fact that the crystallinity of spinel films derived from nitrate precursors was comparable to those derived from metal alkoxide precursors is significant. The perceived advantage of metal alkoxide precursors was that there would be molecular homogeneity whereas nitrate precursors may segregate/crystallize when the solvent had evaporated. This study shows that there was no noticeable segregation for the mixed nitrate precursors. This may lead to more application of

nitrates-derived films because metal nitrates are simpler than metal alkoxides to synthesize and decompose.

Plan-view TEM micrograph of a spinel film on $SrTiO_3$ heated at 700°C for 2 h also showed that there were pores with size about 10 nm, just like those in the alkoxide-derived films. The SAD showed that the film was almost single-crystal-like despite the presence of small pores. The porosity can actually reduce the overall dielectric constant of the film because the pores have a dielectric constant of 1. The total dielectric constant κ can be approximated by a simple mixture law of

$$\kappa = \kappa_f \nu_f + \kappa_p \nu_p \tag{5.4}$$

where κ_f and κ_p are the dielectric constant for the film and the pore, respectively; and ν_f and ν_p and the volume fraction of the film and pore, respectively. The actual dielectric constant of the film can be lower than the bulk dielectric constant of 8.3. The nitrates-derived spinel films may be suitable as a dielectric layer.

5.3.3 Lanthanum Aluminate Films

This section will describe the general characteristics of the films. The temperatures range for formation of the $LaAlO_3$ phase will be discussed further in Chapter 6. XRD spectra for films produced from mixed nitrate precursors on (100) $SrTiO_3$ substrates showed only (100) $LaAlO_3$ phase but no other phase was detected (Fig. 5.4). The FWHM of the rocking curve for the (200) $LaAlO_3$ plane diffraction was approximately 0.8° θ. Again, normal strain was not observed in the films (within 0.1% error). Plan-view TEM on a film calcined at 750°C for 2 h showed that there were pores with sizes range from 15 to 30 nm in the epitaxial films (Fig. 5.5a). These pores were somewhat faceted (Fig. 5.5b). SAD showed that the film had single-crystal-like quality despite being highly porous.

Another piece of evidence for heteroepitaxy of these $LaAlO_3$ films was the ability to deposit new layers of epitaxial films on them. Epitaxial BYC derived from MOD of metal trifluoroacetates were deposited on $LaAlO_3$. More of these BYC films will be discussed in Chapter 7. Epitaxial (100) CeO_2 also were successfully deposited by electron-beam evaporation on these $LaAlO_3$ films (Chang, 1994a). The successful deposition of (100) CeO_2 also showed that the surface did not have any significant amount of non-crystalline, non-epitaxial material. The results from electron-beam evaporation, unlike those from MOD of BYC, ruled out the possibility that chemical precursors or their by-products clean the surface to remove any non-crystalline material.

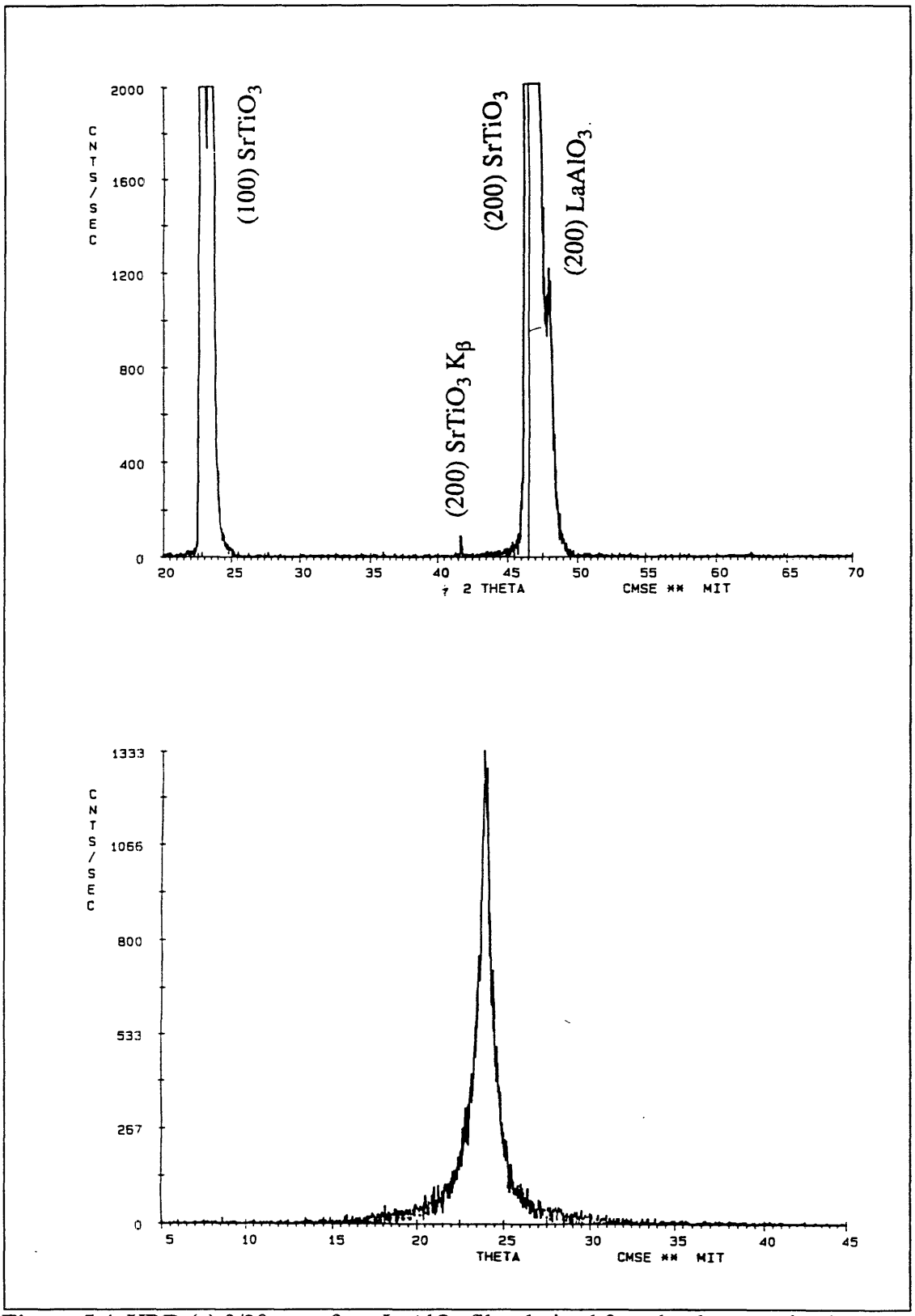

Figure 5.4 XRD (a) θ/2θ scan for a $LaAlO_3$ film derived from lanthanum-aluminum nitrates, and (b) (200) rocking curve of the same film.

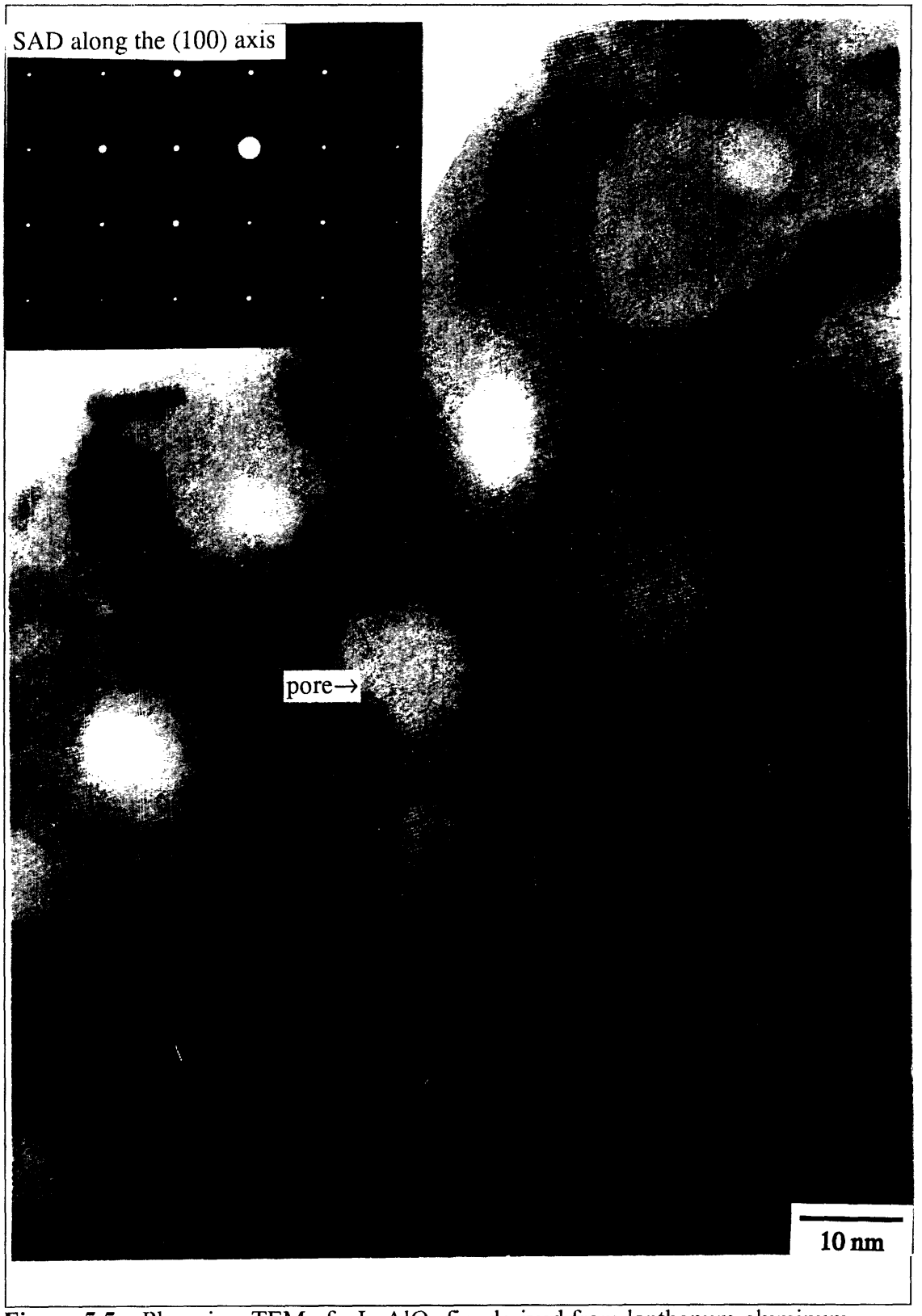

Figure 5.5a Plan view TEM of a $LaAlO_3$ fim derived from lanthanum-aluminum nitrates.

Figure 5.5b Plan view TEM of a $LaAlO_3$ fim derived from lanthanum-aluminum nitrates (at lower magnification).

5.4 OPTICAL PROPERTIES AND POROSITY

The density of the films can be deduced by comparing their indices of refraction with those of bulk samples. The change of refractive index can be related to the porosity (Harris, 1979). One difficulty encountered in this study was the increase in the transmittance of the $SrTiO_3$ substrate after firing. The amount of increase varied from substrate to substrate. This could be due to the defects present in the as-received substrates. The other difficulty was the lack of reported data on the refractive index of bulk $LaAlO_3$. The twinning makes the optical measurement difficult. Attempts to obtain data by ellipsometry had failed to yield any consistent data. Therefore, only the spinel data are analyzed in this study.

The analyzed film must be thick enough to allow for interference of the light. A thicker spinel film was produced by multiple coatings. A total of ten layers was deposited. The first five layers were annealed at 750°C for 2 h. The other five layers were annealed at 900°C. The total thickness was 1.11 μm thick. The cross-section of the film appeared to be uniform according to SEM. The transmission spectrum, however, showed that some of the transmittance minima had higher values than would be expected for a single uniform film. This can be due to the difference in refractive indices from different layers produced by two different annealing temperatures. The film can be assumed to have only two regions, the lower 750°C region and the upper 900°C. The indices can be obtained calculating the transmission from multilayers (Weinstein, 1954). The theories and calculations are described in Appendix C. The thickness and density of each region were varied in the simulation in order to fit the actual observed spectrum. The best fit occurred with the first layer is 0.62 μm thick and the second was 0.5 μm thick. The corresponding densities were 80% and 71% for the two layers according to calculations to convert the indices into densities. The equivalent density was 78% if one homogeneous layer was assumed.

5.5 PORE FORMATION

The TEM micrographs showed that there were pores in both spinel and $LaAlO_3$ films. Pore formation had also been observed in other chemically derived films. TEM micrographs showed some 30 nm pores in $Pb(Zr,Ti)O_3$ prepared by hybrid metalorganic decomposition (Tuttle, 1992). The pore size could be as large as 50 nm to 100 nm in diameter in sol-gel derived $LiNbO_3$ films (Partlow, 1987; Nashimoto, 1995). Volume

porosity can be as high as 50% (Mantese, 1989). Pores were observed even in epitaxial crystallization of amorphous silicon (van Veen, 1993).

The pores may be formed during three stages: when the intermediate films were still amorphous, during crystallization from amorphous phases, and after crystallization. The existence of pores prior to crystallization process was due to the volume change caused by dehydration of the precursors and the decomposition process. TEM micrographs of partially converted films, however, showed that the amorphous part of the films was relatively dense. Therefore, it was not the major contributor to the porosity observed in the final films.

The other stage in which pores can be formed was during crystallization. The volume change depended on form of the amorphous oxide present in the intermediate films. Crystallization of $LaAlO_3$, for example, could undergo a volume change of -13% if the intermediate film was assumed to have the equivalent volume of lanthanum oxide and aluminum oxide. The voids were left behind after the epitaxial films had been formed. The crystal growth front was fast and the voids were trapped. This mechanism was likely to be the source of porosity.

The third way additional pores were formed was after crystallization. There were many point defects present, such as vacancies, when the crystals were first formed. The supersaturation of vacancies caused them to coalesce into the voids during high temperature annealing. The nucleation can be modeled by the classical theory (Russell, 1992). The observed volume fraction of pores, however, was too high to be accountable from the vacancy coalescence. In addition, the self diffusion coefficient of oxygen ion in single-crystal spinel and $LaAlO_3$ is very low. The pre-exponential coefficient D_0 for spinel is 0.89; and the activation energy Q is 105 kcal/mol (= 4.55 eV) [Ando, 1974]. The diffusivity at 750°C is only 3.28×10^{-23} cm^2/s. This makes it very unlikely for the vacancies to have enough mobility to coalesce and form pores. The diffusion data for $LaAlO_3$ could not be found. Common oxides have diffusivity between 10^{-12} to 10^{-15} cm^2/s at their melting temperatures. $LaAlO_3$ has a melting temperature of approximately 2100°C. This suggests that the diffusivity at 750°C will be too low for the length of annealing time used in this study for vacancy coalescence. This mechanism at most contributed only slightly to the porosity.

Plan-view TEM micrograph on a $LaAlO_3$ film calcined at 750°C for 2 h showed that there were pores with size range from 15 to 30 nm in the epitaxial films. Plan-view TEM micrograph on another sample that had been annealed for an additional 2 h at 800°C again showed the existence of similarly faceted pores with approximately the same pore sizes. This is consistent with the low diffusivity of the oxides. This showed

that pores coalescence was slow and pores did not annihilate easily even though the films were thin. Also the ceramic film surfaces are not good sink/source for vacancies.

Nevertheless, it is interesting to model the coarsening rate for the case of high temperature, long time annealing. The coarsening rate of the pores can be modeled as precipitation and coarsening of voids. The concentration of vacancies, however, is not constant because the film surface can serve as a vacancy sink. This is analogous to closed pore shrinkage in densification. One difference is that there are no grain boundaries in the epitaxial film. Dislocations may not be good vacancy sinks either because the strain energy dictates the nature of dislocations in the film. The rate controlling step is assumed to be diffusion of vacancies.

The coarsening can be modeled as follows. The voids are assumed to be cubic and closed. The surface to volume ratio is $6a^2$ where a is the length of the cube. Then the change in the solubility of vacancies Δc can be expressed by the Thompson-Freundlich equation:

$$\Delta c = 4\gamma\Omega C_o/(k_B T a) \tag{5.5}$$

where γ is the interfacial energy of voids; Ω is the molecular volume of the vacancies; C_o is the vacancy concentration under a planar stress-free solid-vapor interface; k_B is the Boltzmann constant; and T is the absolute temperature. The total mass of the precipitates is conserved under the normal precipitate coarsening model. In this case the top surface of the film serves as a vacancy sink. The easiest case is to assume that ceramic free surface is an ineffective vacancy sink with low sink strength. Then

$$\partial V/\partial t = \Sigma\, \partial(a^3)/\partial t = 0 \tag{5.6}$$

for all different values of a. This leads to the familiar time-dependent relation of average size a_{avg}:

$$a_{avg}{}^3 = 16Dt\gamma\Omega C_o/(9k_B T) \tag{5.7}$$

where D is the diffusivity.

The average size, however, will not increase as fast if the surface has high sink strength. The overall concentration of vacancies will decrease as the vacancies diffuse to the free surface. The film thickness is about 100 nm and the pore size can be as large as 30 nm for a $LaAlO_3$ film annealed for 2 h at 800°C. The distance from the top surface of the pore to the free surface of the film is important in the pore shrinkage due to the random walk distance. The other complication arises from the shrinkage of the film due to pore reduction. The in-plane area of the film is fixed; so any volume change

due to shrinkage is linear proportional to the thickness. These reasons make it impractical to use the classical pore reduction model (Coble, 1961).

One method is to approach this problem as a degassing problem common in metallurgy. The pores are assumed to be closed. The coordinate is x = 0 at the substrate/film interface; $x = L_o$ at the initial free surface. The initial conditions are

$$C(L_o, 0) = 0 \tag{5.8}$$

$$C(x, 0) = C' \text{ for } 0 \leq x < L_o \tag{5.9}$$

for a film with an initial thickness L_o. C is the concentration of vacancies. The boundary condition are

$$C(L, t) = 0 \tag{5.10}$$

$$J(0, t) = 0 \tag{5.11}$$

where L is the instantaneous thickness as the film shrinks. The variation of L with time is high because of the high initial porosity due to the volume change of crystallization. The solution for a simpler case with fixed L is a Fourier series of cosine waves. Even this simpler version makes the mathematics complicated when right-hand term in Equation (5.8) is not zero. The coarsening rate is therefore difficult to solve analytically.

The coarsening rate for spinel and $LaAlO_3$, based on the diffusivity, should be extremely low such that the pores can be regarded as metastable. There is, however, a trend that can be deduced from these models. The pores near the substrate/film interface are formed first. They have more time to coarsen. Their distance from the free surface is also greater. This means that they shrink slower due to vacancy annihilation.

5.6 SUMMARY

The results in this chapter demonstrated that epitaxial multi-cationic oxide films can be produced by a new chemical route: mixed nitrate precursors. This simpler approach produced epitaxial spinel films with qualities similar to those derived from magnesium aluminum isopropoxide, a more complex precursors. TEM micrographs of both spinel and lanthanum aluminate films hardly show any grain boundaries. The films are single crystal-like but contain faceted pores. The pores cannot be annihilated or coalesce at the temperature/time range used in this study due to the low diffusivities.

CHAPTER 6
EPITAXIAL GROWTH OF NITRATES-DERIVED FILMS

6.1 INTRODUCTION

It is established in Chapter 3 that the alkoxide and mixed nitrates and precursors first decompose into solid, amorphous intermediate films prior to formation of the epitaxial films. The growth mechanism and kinetics of how these solid, amorphous films transform into epitaxial films are investigated in this chapter. The effect of lattice-matched substrates is discussed. A simple model is proposed to explain the mechanism and kinetics of the epitaxial phase formation. Understanding the nucleation and growth phenomena of nitrates-derived spin-on films can lead to better controlled microstructures. The understanding gained in this study can also be applied to heteroepitaxial growth of other types of spin-on films.

6.2 EXPERIMENTAL PROCEDURE

6.2.1 X-Ray Diffraction

Normal powder XRD was done on both spinel and $LaAlO_3$ films on different substrates and calcined at different temperatures to determine the crystallization temperature of the epitaxial phases. These films were typically maintained at the peak temperature for 2 h.

Lanthanum aluminate and spinel films on $SrTiO_3$ substrates were heated at rate of 10°C/min to a constant temperature which was maintained for different lenghts of time before quenching. The temperatures used for $LaAlO_3$ films were 650°C, 665°C, 680°C, 700°C, and 750°C. The temperatures used for spinel films were 650°C and 750°C. The in-plane orientation and the fraction of conversion of these epitaxial films were measured quantitatively by four-circle X-ray diffraction.

The four-circle XRD setup is shown schematically in Fig. 6.1. The orientation of the sample is rotated by a four-circle goniometer. The "four circles" are the two-theta (2 θ), theta (θ), chi (χ) and phi (ϕ). The θ and 2θ are similar to those in normal powder diffraction. In this set up, however, the θ and 2θ can be rotated independently such that the 2θ may not necessarily equal to twice the value of the θ. The ϕ axis is normal to the film surface. Chi controls the tilt of the incident X-ray beam with respect to the sample. The Cu K_α radiation was generated by a Rigaku rotating anode source. The

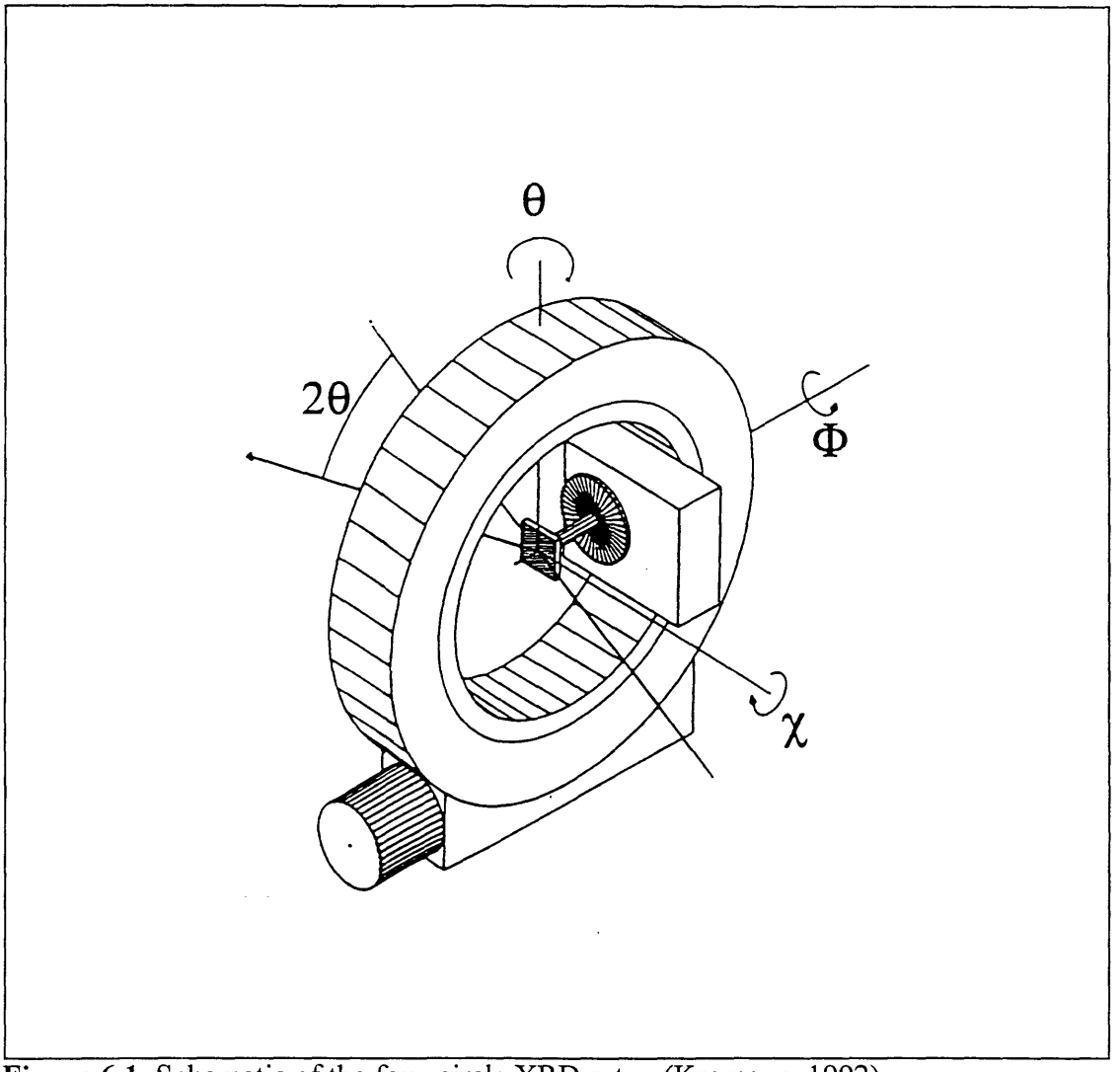

Figure 6.1 Schematic of the four-circle XRD setup (Kromann, 1992).

accelerating voltage in all the four-circle XRD experiments was 50 kV and the current was 160 mA.

Each sample was first aligned by maximizing the intensity of a substrate diffraction peak. Initially a normal θ-2θ scan was performed to measure the (200) $SrTiO_3$ substrate diffraction peak. Theta was rocked slightly in both directions to find the maximum the (200) $SrTiO_3$ substrate diffraction peak. The θ value that maximized the (200) substrate peak would then be used throughout the experiment. Next the 2θ and χ values of the desired (hkl) substrate plane were set. The φ axis was rotated to find the position of the substrate peak. The χ angle was rocked again to maximize the substrate diffraction intensity once the φ value was set.

The (hkl) plane the film was scanned after the substrate had been correctly aligned. The choice of (hkl) plane was chosen based on three criteria: minimum substrate interference, strong diffraction intensity, and ease of alignment. High 2θ values were chosen because the difference in the 2θ values between the film and substrate plane increases as the 2θ increases. Any (hkl) diffraction peak that was absent in the substrate was not chosen because it could not be aligned by using the substrate. The (311) plane of spinel, therefore, was not used despite its high diffraction intensity. The (211) plane of $LaAlO_3$ and the (440) plane of spinel were used in the four-circle XRD experiments.

The in-plane orientation of the films was measured by scanning the φ. The integrated 2θ intensities were used for the quantitative measurement of the fraction of film conversion. The integrated intensities from the 2θ scans were used because the intensity is more sensitive to the change in the 2θ position than of the φ position. A scan in the 2θ could ensure that a slight misalignment in the 2θ position would not greatly reduce the integrated intensity.

6.2.2 Transmission Electron Microscopy

Cross-sectional TEM specimens were made by first cutting a piece of sample along its (100) axis. Then the film side was glued with M-Bond 610 to a piece of polished sapphire crystal and cured with the same heating schedule as in plan-view TEM sample preparation. The specimen sandwich was mounted on a tripod polisher. One side of the specimen was polished to a 1 μm finish while the position of the sample was adjusted to ensure that the polished side was parallel to the (100) axis. The polished side was then glued with M-Bond 610 to a nickel TEM grid with a 800 μm aperture. The film/substrate interface was aligned along the diameter of the TEM grid aperture. The heat curing for the M-Bond 610 was repeated. The sandwich was polished until it was

about 50 μm thick. It was dimpled further to 5 μm thick prior to ion milling. Ion milling was done in a cold stage setup to avoid ion damage to the sample. The ion guns were positioned so that the ion beams remained perpendicular to the glue line throughout the ion milling process.

Transmission electron microscopy and selected area diffraction (SAD) were done on the calcined nitrate powders as well. The powder samples were dispersed on copper TEM grids that have a layer of carbon on Formvar film. These samples were further carbon coated prior to observation to avoid charging. Microscopy was performed on a JEOL 200CX microscope operating at 200 kV.

6.3 SUBSTRATE EFFECT ON NUCLEATION

Nucleation of crystalline materials can be either heterogeneous or homogeneous. Studies have shown that heterogeneous nucleation, or "seeding", can lower the activation energy for nucleation and reduce the observable crystallization temperature in powder samples. Seeding by α-alumina in sintering of a boehmite sol-gel lowered the transformation temperature of θ- to α-alumina by as much as 170°C (Kumagai, 1985). The reduction of transformation temperature was attributed to solid phase epitaxy (McArdle, 1989). Seeding also decreased the crystallization temperature of rutile by nearly 250°C (Roy, 1986), of β-$ThSiO_4$ by 200°C (Vilmin, 1987), and of α-cordierite by 125-150°C (Kazakos, 1990). Seeding can also reduce the temperature of thin film formation. Lead zirconate titanate thin film formation temperature was reported to be reduced by 100°C with $PbTiO_3$ seeding (Kwok, 1993).

6.3.1 Lanthanum Aluminate Films

The role of substrate in assisting the crystallization was examined by TEM and XRD. Diffraction from the (100) $LaAlO_3$ plane was observed in films on $SrTiO_3$ substrates by XRD when the precursor films were heated to as low as 650°C. Diffraction from the (100) $LaAlO_3$ plane was not observed, however, when the films were heated to only 630°C. No other phase was detected except for the substrate diffraction in either case. Diffraction from the (100) $LaAlO_3$ plane was not detected on MgO, YSZ, and $MgAl_2O_4$ substrates for films held at 750°C for 2 h. Polycrystalline $LaAlO_3$ diffraction peaks were observed instead in films on MgO substrates when heated to 900°C for 2 h. $LaAlO_3$ films on $SrTiO_3$ still showed the (100) orientation even when heated to 900°C for 2 h.

For comparison no crystallinity was observed by TEM for the mixed lanthanum aluminum nitrates powder calcined at 750°C for 2 h. Some signs of crystallinity were observed after calcination at 775°C for 2 h, but the weak intensities of the diffraction spots made the determination of the crystal structure impossible. Polycrystalline $LaAlO_3$, however, was detected by SAD when the mixed lanthanum-aluminum nitrates powder was calcined at 800°C for 2 h.

Detection of (100) $LaAlO_3$ on $SrTiO_3$ substrates by XRD at 650°C showed that lattice-matched substrates can reduce the nucleation temperature by at least 100 K. No major reduction in nucleation temperature was observed when the lattice mismatch was large (5.2%, 6.1% and 10.0% for YSZ, $MgAl_2O_4$, and MgO substrates, respectively vs. 3% for $SrTiO_3$ substrate).

Polycrystalline $LaAlO_3$ films annealed at 900°C were observed on MgO substrates. This suggested that there were two competing growth mechanisms: homogeneous nucleation with random orientation vs. solid state epitaxy initiated on the substrate/film interface. Lattice-matched substrates would induce epitaxial growth by heterogeneous nucleation at lower temperature. Homogeneous nucleation occurred at higher temperature and formed randomly oriented grains on non lattice-matched substrate. The results are summarized in Table 6.1.

Table 6.1 Crystallization Temperature of Nitrates-Derived Films on Different Substrates

Substrate	Film	Mismatch	Temperature	Phase observed
$SrTiO_3$	$LaAlO_3$	-2.9%	630°C	amorphous
$SrTiO_3$	$LaAlO_3$	-2.9%	650°C	epitaxial
YSZ	$LaAlO_3$	5.2%	750°C	amorphous
Spinel	$LaAlO_3$	-6.1%	750°C	amorphous
MgO	$LaAlO_3$	-9.9%	750°C	amorphous
MgO	$LaAlO_3$	-9.9%	900°C	random orientation
$SrTiO_3$	Spinel	3.5%	750°C	epitaxial
MgO	Spinel	-4.0%	750°C	epitaxial
$LaAlO_3$	Spinel	6.6%	750°C	amorphous

6.3.2 Spinel Films

The (400) diffraction of spinel was detected by XRD when the nitrates-derived films were deposited on $SrTiO_3$ at 700°C for 2 h. Epitaxial spinel film was not formed on $LaAlO_3$ substrate but on MgO substrate. These observations can be explained by the lattice mismatch. The lattice mismatch between $MgAl_2O_4$ film and $SrTiO_3$ or MgO substrate is only 3.5% and 4%, respectively, whereas the mismatch between $MgAl_2O_4$ and $LaAlO_3$ is 6.6%. The smaller lattice mismatch reduced the nucleation temperature of $MgAl_2O_4$. These observations suggested that substrates with small lattice mismatch reduced the crystallization temperature of $MgAl_2O_4$.

X-ray diffraction patterns of alkoxide-derived spinel films on $SrTiO_3$ showed the presence of only (400) $MgAl_2O_4$ plane diffraction after calcination for 2 h at 800°C. No $MgAl_2O_4$ diffraction peak was detected for films calcined at 750°C for 2 h. No other phase was observed in either case. The formation of $MgAl_2O_4$ was confirmed by the presence of the $MgAl_2O_4$ (311) diffraction in pole figure XRD. No (400) $MgAl_2O_4$ diffraction was observed on films grown on $LaAlO_3$ substrates even for calcination at 850°C for 2 h. Formation of epitaxial $MgAl_2O_4$ films only on $SrTiO_3$ substrates can be explained by the lattice mismatch between the film and the substrates, as in the case of mixed nitrates.

Prior substrate annealing has been reported to increase the number of surface steps for nucleation. It was reported that when a single-crystal $SrTiO_3$ substrate was preheated to 1100°C prior to spin-coating of precursor for MOD derived $SrTiO_3$, there was a lowering of nucleation temperature (Braunstein, 1994a). A further reduction in crystallization temperature was not observed in spinel films even when the $SrTiO_3$ substrates were preheated to 1000°C for 8 h.

6.4 EPITAXIAL GROWTH MECHANISM

The epitaxial growth mechanism responsible for the growth in nitrates-derived films is discussed in this section. Four possible heteroepitaxial growth mechanisms are mentioned in Chapter 2. The first mechanism involves the nucleation of epitaxial grains at the film/substrate interface (Fig. 2.9a). These epitaxial grains grow by consuming the intermediate film. The second mechanism is by surface energy driven grain growth (Fig. 2.9b). A polycrystalline film is formed initially. Subsequent grain growth produces grains with size on the order of the film's thickness. The difference in the surface and interfacial energies of the grains is the driving force promoting grain

growth. Grains with certain orientation grow at the expense of grains of other orientation. Epitaxial grains, which generally have lower energy, grow and consume other grains. The third mechanism is the formation of a transient liquid in which the epitaxial phase precipitates (Fig. 2.9c). The fourth mechanism is the reaction between the substrate with the intermediate film to produce a new layer at the interface (Fig. 2.9d). These mechanisms are examined to determine which one applies in the nitrates-derived films.

The possibility that the mechanism of substrate/film reaction occurred can be eliminated simply by the fact that the cations in the epitaxial films differ from those of the substrate. XRD spectra also confirm that a reaction layer was not present. Results from Chapter 3 also showed that there was no distortion of the pellet shapes observed in the isothermal annealing experiments with the nitrate powders. Moreover, the DTA curves of nitrates did not exhibit any endotherm commonly associated with melting. Thus, the transient liquid phase induced epitaxy model also cannot explain the heteroepitaxial growth.

The two remaining mechanisms can be determined by examining the precursor films prior to crystallization. The ϕ scan data are particularly useful in determining if the films are amorphous or polycrystalline prior to epitaxial grain growth. Figure 6.2 illustrates the trends of the ϕ scan data for the cases of amorphous and polycrystalline intermediate films. At first the designated (hkl) diffraction intensity will be independent of the ϕ position if the intermediate filmd are polycrystalline. The (hkl) intensity at the preferred ϕ position will increase while the intensity at other ϕ positions will decrease with increasing annealing time because the grains with the correct orientation grow at the expense of grains with other orientations (Fig. 6.2a). On the other hand only the preferred ϕ position will increase in intensity but the other positions will remain the same low intensity with increasing annealing time if the intermediate films are amorphous (Fig. 6.2b).

Figure 6.3a showed the ϕ scan data for the (211) plane of $LaAlO_3$ films annealed isothermally at 650°C for various lengths of time. Initially the (211) diffraction intensity would be independent of the ϕ position if the initial films were polycrystalline. The strong dependency of the intensity on ϕ even at very short hold time, however, showed that only epitaxial crystals were formed at first. The absence of the (211) diffraction at other orientations showed that, prior to the growth of the epitaxial (100) film, the precursor films were amorphous. Similar results were found for films annealed at higher temperatures.

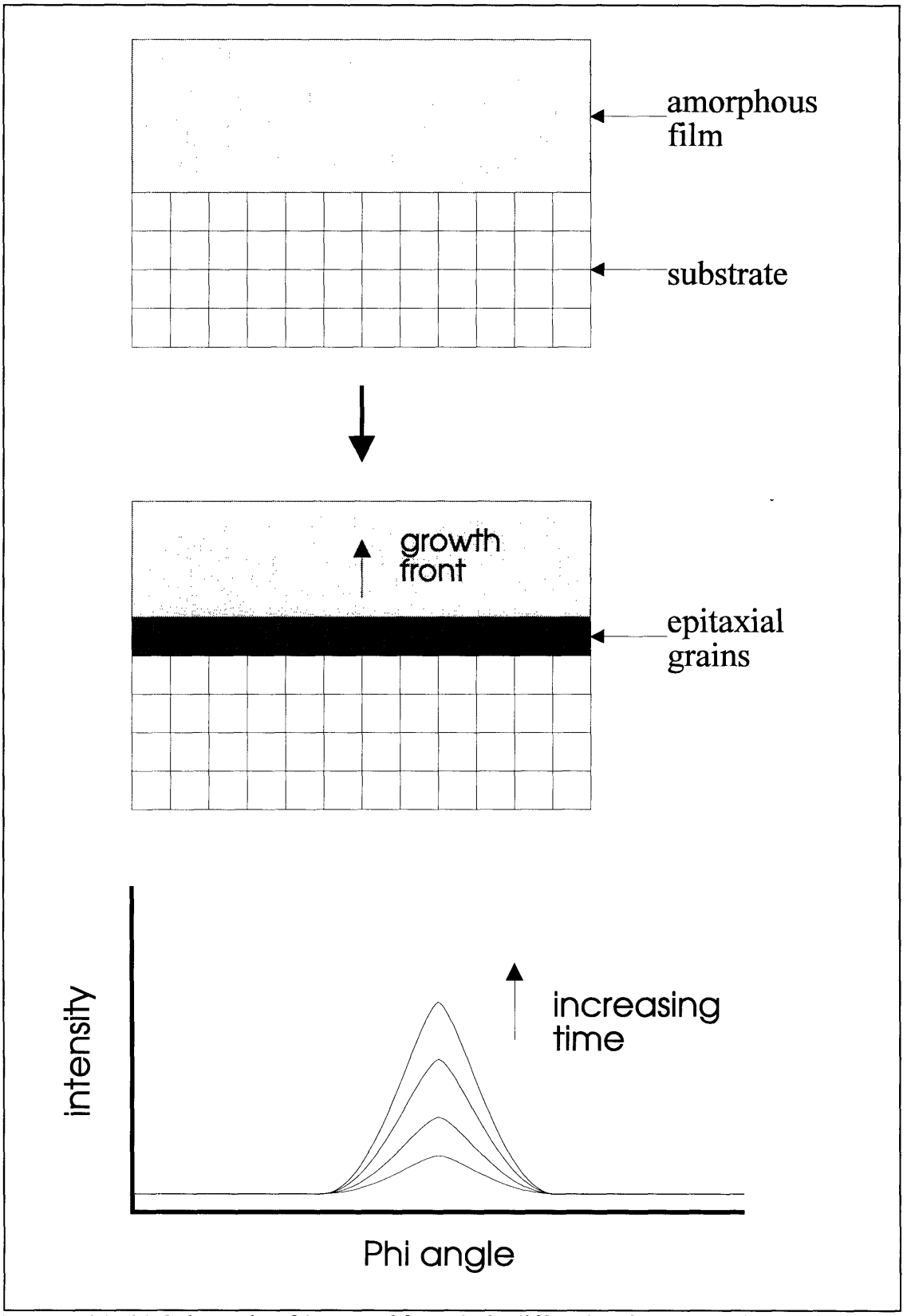

Figure 6.2 (a) Schematic of ϕ scan of four circle diffraction for epitaxial growth from the substrate/film interface.

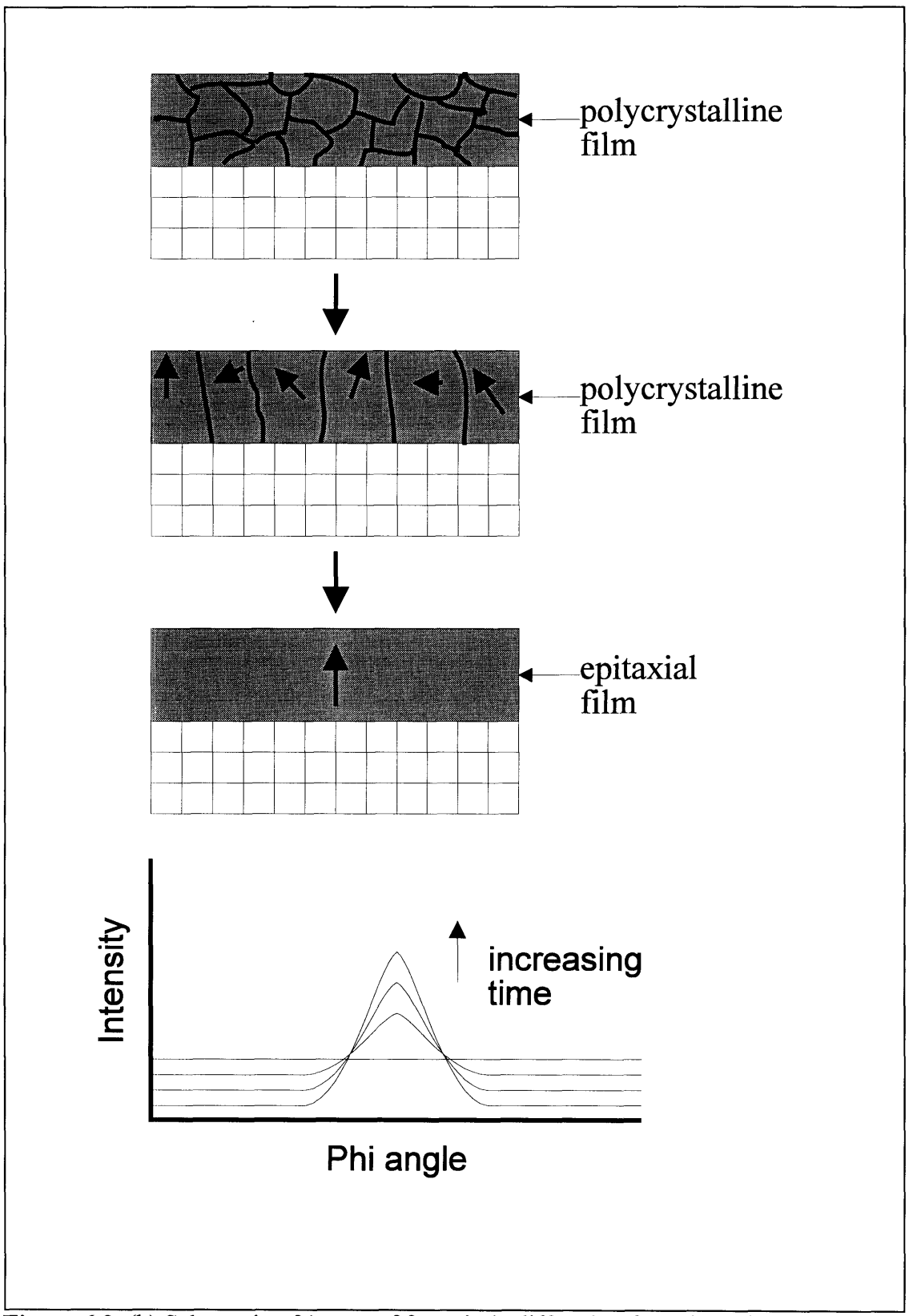

Figure 6.2 (b) Schematic of ϕ scan of four circle diffraction for epitaxial growth from from surface-energy-driven secondary grain growth..

The (440) diffraction peak intensities of the spinel films annealed at 650°C were extremely low regardless of the annealing time. Another set of experiments in which an annealing temperature of 750°C was used, the ϕ scan data for the (440) spinel plane are shown in Fig. 6.3b. Here again, although the intensities were weak, they had the same trend as those of $LaAlO_3$ films. Those four-circle XRD data suggested that the epitaxial film growth from nitrate precursors was not by surface/interfacial energy driven secondary grain growth.

The only mechanism left is the formation of epitaxial film along the substrate/film interface and its upward growth. This was confirmed by cross-sectional TEM micrographs of $LaAlO_3$ films heated to 650°C for 2 h and 3 h and then quenched. The micrograph of the 3 h hold (Fig. 6.4) showed that the region near the substrate was crystalline whereas the top region remains amorphous.

The TEM photographs of quenched films also showed that the growth interface was rough. This was rather unusual for growth of ceramic materials. Typically ceramic growth would result in a sharp or faceted growth interface. One possible reason is the huge driving force for crystallization. The amorphous region can be viewed as a supercooled liquid because the melting temperature of $LaAlO_3$ is 2075-2110°C. The undercooling was approximately 1450°C. A large undercooling produced a huge driving force for transformation from amorphous to crystalline phase. A sharp interface was rare with a huge driving force (Cahn, 1960, 1966).

One may argue that the low entropy change in crystallization is another likely explanation for the rough interface (Jackson, 1967). Jackson proposed that the magnitude of the change of entropy (ΔS_f) divides by the Boltzmann constant (k_B) can predict whether the interface would be rough or smooth. A $\Delta S_f/k_B$ of less than 2 will give a rough growth interface when the system solidifies at the melting temperature. In this case the amorphous region can be viewed as a undercooled $LaAlO_3$. The calculated entropy of fusion at melting temperature from liquid to solid $LaAlO_3$ is 4.60 cal mol^{-1} K^{-1} (=1.99 x 10^{-4} eV/K) [Wu, 1992]. The value of $\Delta S_f/k_B$ is 2.32. There are two differences from the original Jackson derivation. The value of ΔS_f at 650°C should be different from the one at the melting temperature. The Jackson α-factor derviation was formulated primarily for reaction at the melting temperature. The temperature in crystallization in this study is also much lower than the melting temperature of $LaAlO_3$. The value of ΔS_f at 650°C could not be found in the literature. It can be estimated by assuming that ΔH_f is relatively constant with respect to temperature. The value of ΔH_f at the melting point is 11.88 cal mol^{-1} K^{-1}. The value of $\Delta S_f/k_B$ is 5.99, which is too high to for the Jackson α-factor explanation.

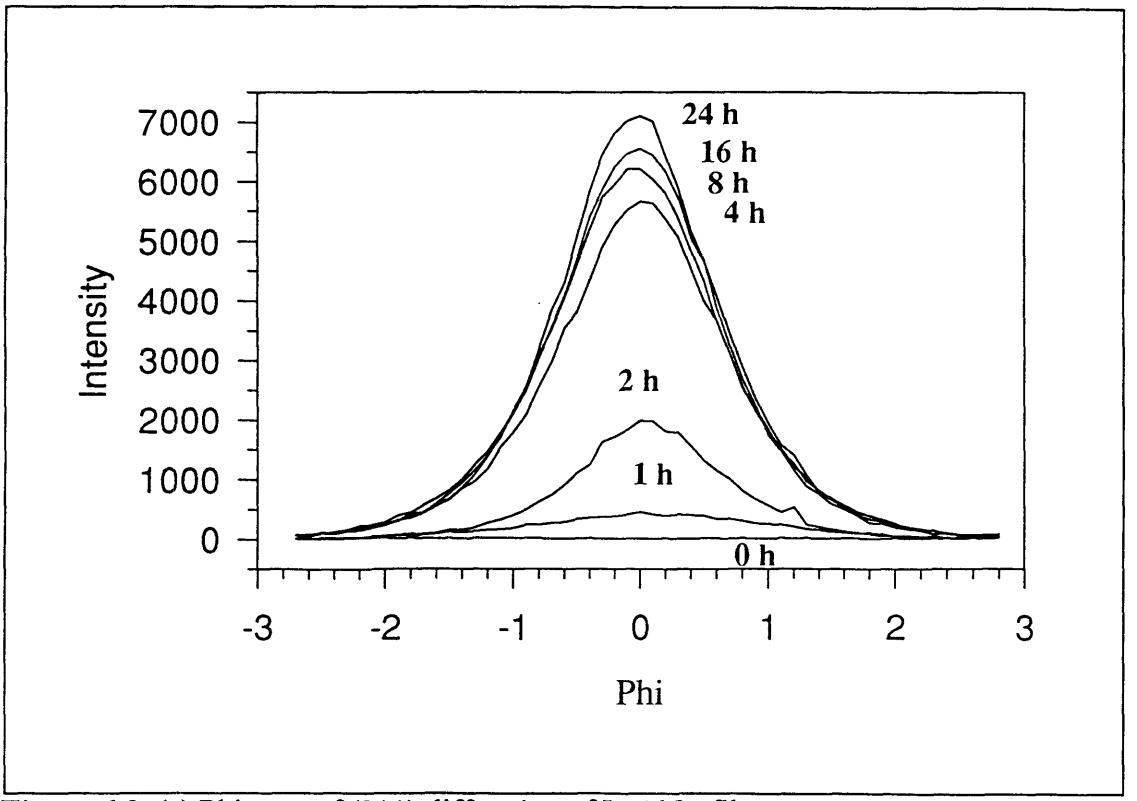

Figure 6.3 (a) Phi scan of (211) diffraction of $LaAlO_3$ films.

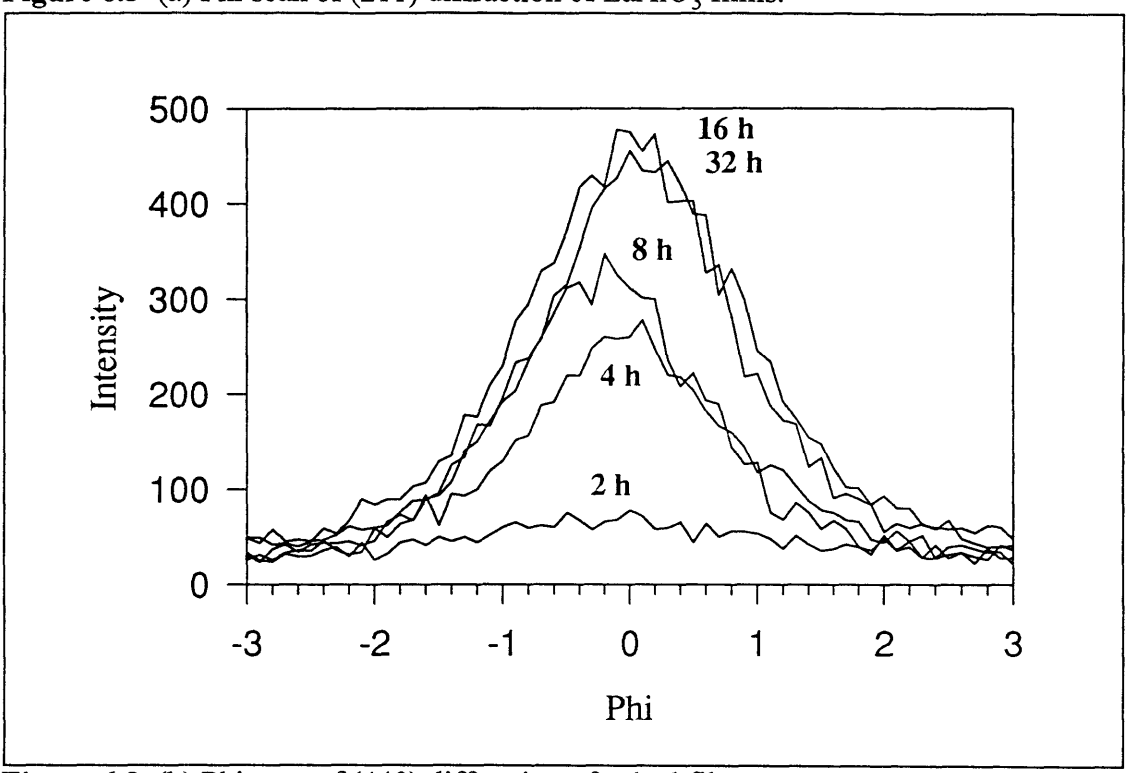

Figure 6.3 (b) Phi scan of (440) diffraction of spinel films.

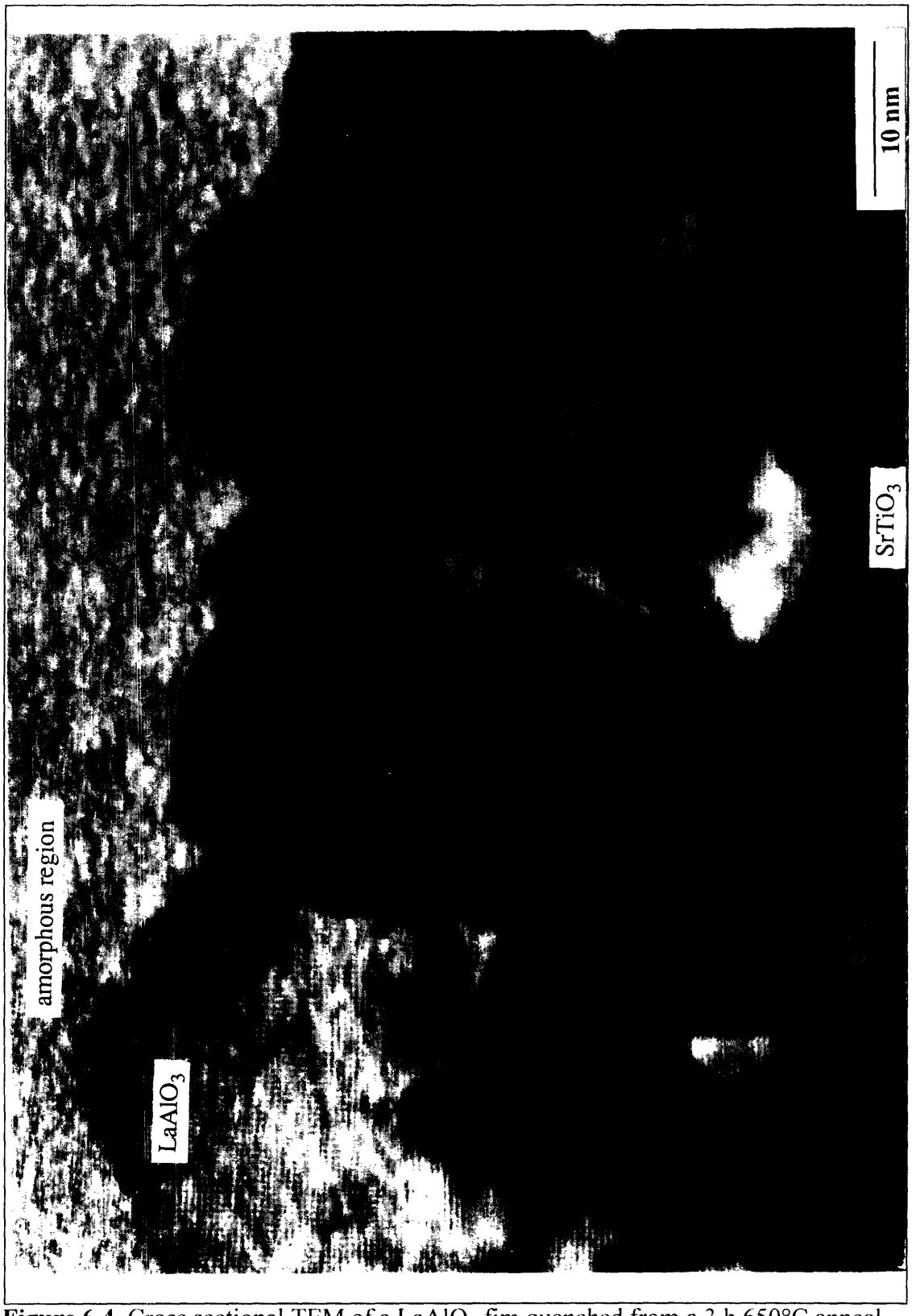

Figure 6.4 Cross sectional TEM of a $LaAlO_3$ fim quenched from a 3 h 650°C anneal.

6.5 GROWTH KINETICS

The integrated intensities of the 2θ scan of the (211) $LaAlO_3$ and (440) spinel diffraction were used to quantify the fraction of crystallization. The assumption is that the integrated intensity of the diffracted beam is proportional to the numbers of scattering centers (and thus the amount of epitaxial material). Pores do not contribute to the diffracted beam. The contribution to the diffraction beam intensity from material further below the surface is less than the material on the surface due to absorption. The fraction of diffraction intensity G_x contributed by a surface layer of depth x can be expressed as

$$G_x = 1 - e^{-\mu x(1/\sin\gamma + 1/\sin\beta)} \tag{6.1}$$

where μ is the linear absorption coefficient; γ is the incident angle; and β is the diffracted angle. The mass absorption coefficient μ/ρ is the weighted average of the mass absorption coefficients of its constituent elements. It can be written as

$$\mu/\rho = w_1(\mu/\rho)_1 + w_2(\mu/\rho)_2 + \ldots \tag{6.2}$$

where $(\mu/\rho)_i$ and w_i are the mass absorption coefficient and weight fraction for the i th element, respectively. The linear absorption coefficient for $LaAlO_3$, calculated from tabulated values, is 1607 cm^{-1} (Cullity, 1978). The value of μx is 0.016 for films 1000 Å thick. A Taylor series can be used to approximate Equation (6.1) such that

$$G_x \approx 1 - [1 - \mu x(1/\sin\gamma + 1/\sin\beta)] \tag{6.3}$$

Thus, it is reasonable to assume the diffraction intensity is directly proportional to the amount of $LaAlO_3$ present.

The integrated intensities of the $LaAlO_3$ samples annealed for different lengths of time were plotted according to the Johnson-Mehl-Avrami transformation equation for nucleation and growth (Avrami, 1939; Johnson, 1939):

$$X = 1 - \exp(-kt^n) \tag{6.4}$$

where X is the fraction of transformed; and t is time. The diffraction data showed that n was 1.43, 1.49±0.45, and 1.49±0.01 for $LaAlO_3$ on $SrTiO_3$ at 650°C, 665°C and 680°C, respectively (Fig. 6.5). The slope for n is more reliable at 680°C than at 650°C because 650°C is close to the temperature at which crystallization may not occur. For comparison, homoepitaxy recrystallization of silicon typically had n = 1. The volume crystallized changes proportional to time until completion. Other heteroepitaxy systems such as barium ferrite on sapphire had n between 2.3 and 3.1 (Parker, 1993).

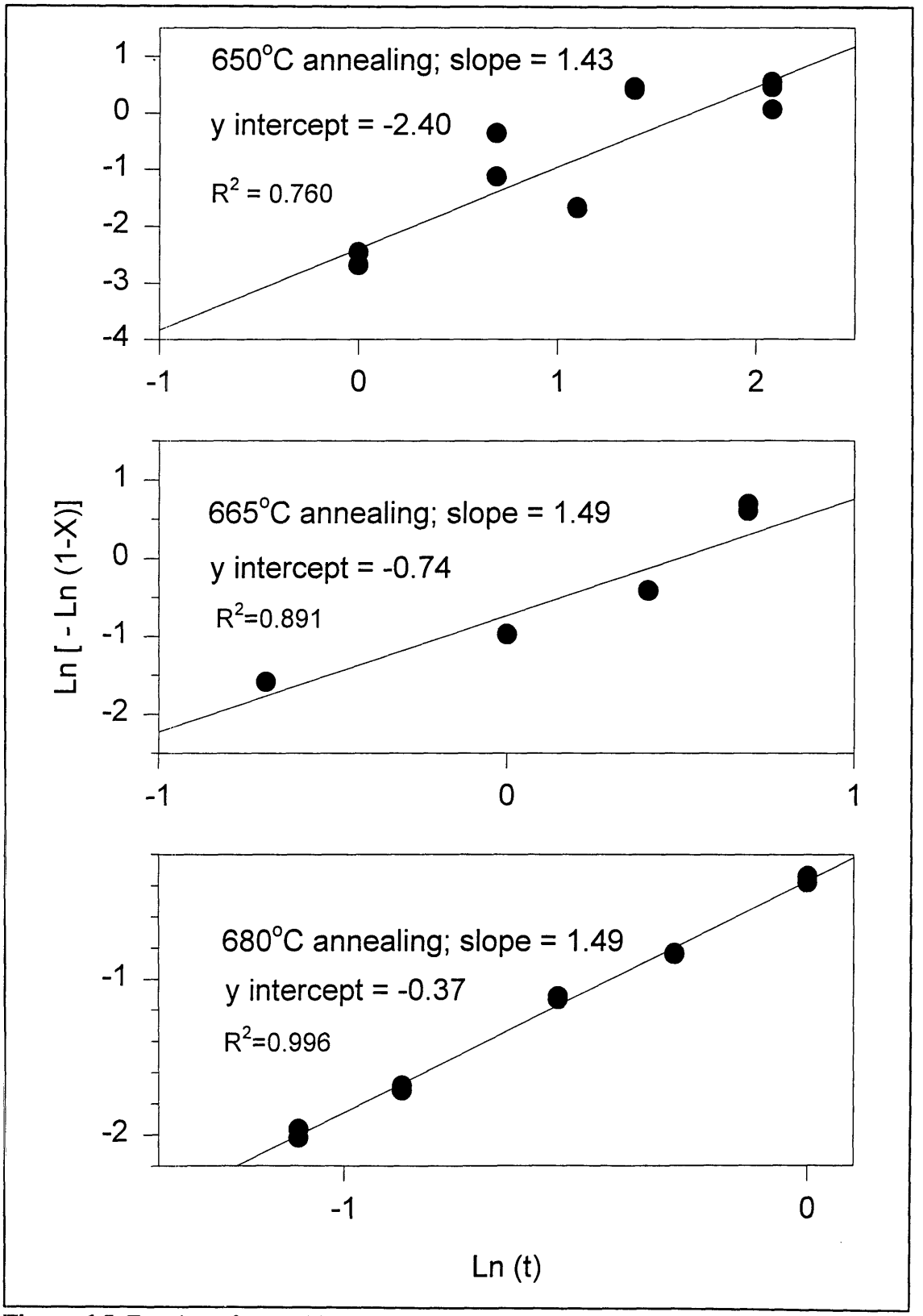

Figure 6.5 Fraction of crystallization vs. annealing time for $LaAlO_3$ on $SrTiO_3$.

The growth of the $LaAlO_3$ is believed to be interface-controlled. There is no need for long-range diffusion because the amorphous phase is well mixed. The growth interface indicated that it is non-facetted and does not have periodicity (Fig. 6.4). The non-facetted, non-dendritic interface suggests that the crystallization is interface-controlled (Cahn, 1966).

The Johnson-Mehl-Avrami exponent of 1.4-1.5 is not easy to explain. A perfect layer-by-layer growth (FM mode) for an interface-controlled transformation has n = 1, as in silicon homoepitaxial growth. In homoepitaxy the substrate is a huge nucleus. In heteroepitaxy, nuclei are formed at the early stage and cover the entire plane of the substrate interface (Fig. 6.6a). The film is modeled as growing upwardly. If the nucleation is fast and rapidly covers the surface before any growth proceeds, then it can be approached as homoepitaxy and has n = 1.

The most probable scenario in this case is that the nuclei were formed gradually. The entire substrate surface was not covered with nuclei instantaneously. Those epitaxial regions formed earlier could grow three-dimensionally. Nucleation continued until the entire substrate surface was covered with $LaAlO_3$. Nuclei formed later were impinged in the in-plane direction but could grow upward (one dimensionally). This gave a Johnson-Mehl-Avrami exponent greater than 1. This route is schematically illustrated in Fig. 6.6b. This was different from a typical continuous nucleation three dimensional interface-controlled model. Here all the nuclei were confined in the plane of substrate surface. Also, nucleation stopped once the entire substrate surface had been covered with crystallized material. This explanation is supported by the TEM micrograph of a partially converted film (Fig. 6.4). The converted region appeared as a conglomerate of spheres of crystallized $LaAlO_3$.

The more extreme case is when there were only a few nuclei formed initially. These nuclei, if scattered far apart, continued to grow until they reached the top surface of the film. They were more likely to first be impinged in the upward direction than in the in-plane direction. The situation is similar to the normal three dimensional growth. The Johnson-Mehl-Avrami exponent will be close to 3. This scenario is unlikely to occur because the TEM micrographs did not show isolated converted regions.

Other potential factors that may influence the growth rate include pores, vacancies and strain. Pores, product of crystallization volume change, may slow the growth rate as in pore drag on grain boundary movement in ceramics. However, the cross-sectional TEM micrographs did not show any voids near at the growth interface. The other diffusion-controlled species are vacancies. Vacancies are formed and they may have to diffuse out for further crystallization of $LaAlO_3$. However, it is believed that only short

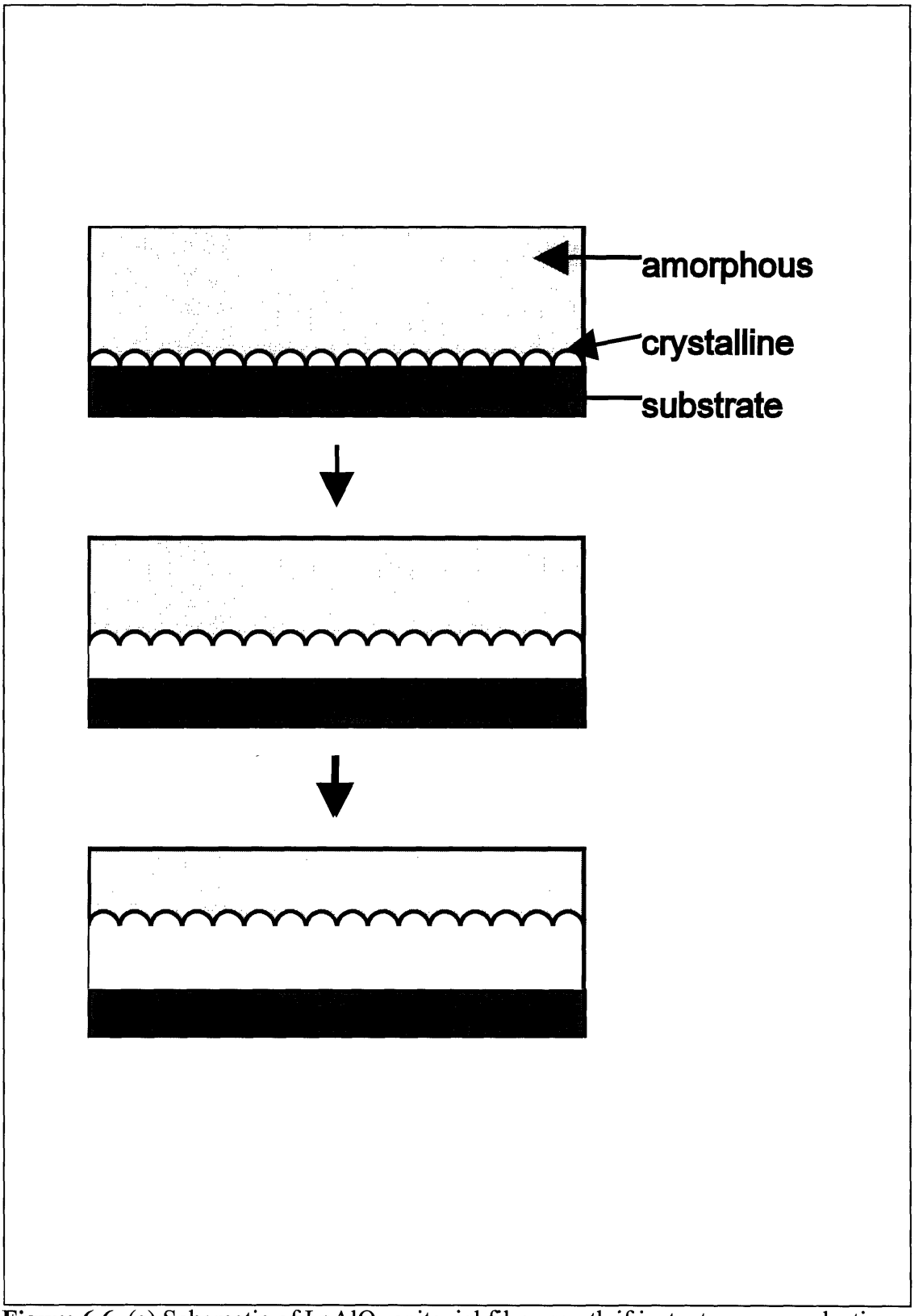

Figure 6.6 (a) Schematic of $LaAlO_3$ epitaxial film growth if instantaneous nucleation occurs.

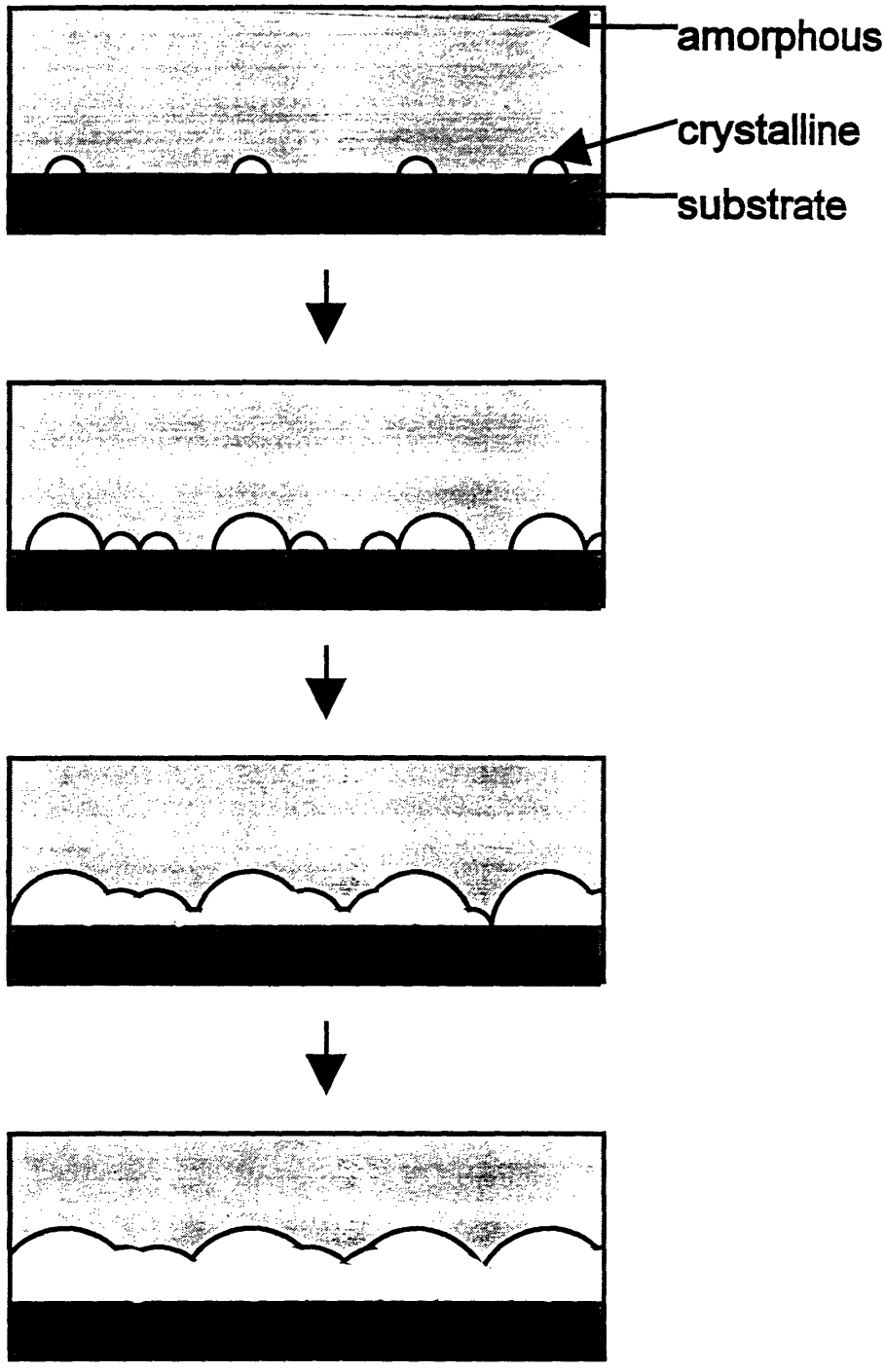

Figure 6.6 (b) Schematic of $LaAlO_3$ epitaxial film growth if nucleation occurs over time.

range diffusion was involved and the effect of vacancy diffusion was negligible. The other potential factor that may influence the growth is the strain energy due to lattice mismatch. Lattice strain has been shown to perturb the growth rate. A similar situation was observed in solid-phase epitaxy regrowth of silicon and silicon-germanium alloy from amorphous phase. The recrystallization rates of strained Si-Ge alloys were lower than those of unstrained alloys (Hong, 1992). Strained Si-Ge alloys also had higher activation energies for regrowth than pure silicon had (Paine, 1991; Lee, 1993). It was also observed that interface velocity and activation energy of regrowth were position-dependent (Lee, 1993). However, this factor was negligilbe for the films studied here. The films, including the partially-converted ones, were not strained.

A slight increase in annealing temperature increased the growth rate sharply. Complete crystallization occurred in less than one hour at temperatures as low as 700°C in contrast to hours needed to completely crystallize a 1000 Å thick film at 650°C. Kinetics study for $LaAlO_3$ films at annealing temperature higher than 680°C could not be done with any accuracy because of the fast growth rate above 650°C. The activation energy can be calculated from the k values using an Arrhenius plot by the following equation

$$k = k_0 \exp(-G/k_bT) \tag{6.5}$$

where G is the effective activation energy; k_b is the Boltzmann constant; T is the absolute temperature; and k_0 is the pre-exponential constant. Calculation based on the quenching experiment data from films annealed at 650°C, 665°C, and 680°C showed that the effective activation energy was approximately 5.1 eV. For comparison, the activation energy for heteroepitaxy of barium ferrite on sapphire was 4.0 eV (Parker, 1993). The reported activation energy for homoepitaxy of amorphous silicon was approximately 2.7 eV (Olson, 1988).

This effective activation is a combination of the nucleation activation energy and growth activation energy. It can be approximated as

$$G = aG_n + bG_g \tag{6.6}$$

$$a + b = n \tag{6.7}$$

$$N(t) = N_0 t^a \tag{6.8}$$

where G_n and G_g are the nucleation and growth activation energy, respectively; n is the Johnson-Mehl-Avrami exponent; and N(t) is the nucleation rate (Ranganathan, 1981). It can be approximated from the previous argument that the growth is mostly one-

dimensional. Thus b can be approximated as 1. This leads to an approximation of a = 0.5, which is consistent with the explanation of decreasing nucleation. The high activation energy of transformation actually is useful to control the microstructure of the film. A slight adjustment to the temperature can slow the growth rate significantly but may not change the diffusion rate of vacancies by much. This allows for diffusion of vacancies to the growth front such that denser films can be made.

Four-circle XRD data for spinel were not used in this study due to the low diffracted beam intensity from spinel. A fully crystallized spinel film (annealed for 16 h at 950°C) had an intensity only approximately 300 cps. The background noise itself was about 20 cps. Longer data collection time did not help significantly. This made data from the early stage of crystallization extremely unreliable.

There were several sources of error which could affect the accuracy of these measurements from four-circle XRD. The most prominent one was intensity of diffracted beam detected. The intensity fluctuated with time. Figure 6.7 shows an extreme case of fluctuation from two 2θ scans from the same sample. The scans were taken right after each other. The difference could be noticeable. The integrated values were approximately the same, but the whole peak seems to be shifting. This could be due to the delay in picking up the signal by the detector as the sample was rotating. Fortunately most scans did not exhibit such shift. The difference in the integrated intensities is not signifcant even for the sample with this magnitue of shift. The other source of error was from misalignment of the sample. This could be significant because the diffracted intensity was position sensitive, although the samples had been aligned carefully in all studies. The other source of errors was from the temperature control of the furnace, as it is shown that even a fluctuation of a few degrees caused a change in the crystallization rate. Again, the temperature control of the furnace is good enough to make this error negligible.

6.6 SUMMARY

The heteroepitaxial growth mechanism and kinetics are examined by using four-circle XRD and TEM. Never before has four-circle XRD been used in characterization epitaxial growth. The likely growth mechanism for nitrates-derived $LaAlO_3$ films on $SrTiO_3$ begins with nucleation of epitaxial phases on the substrate/film interface. At that time, the films are still amorphous and solid. The film grows upward and consumes the amorphous region. The growth is not exactly layer-by-layer growth as in homoepitaxy. The growth route is believed to have both nucleation and growth occur

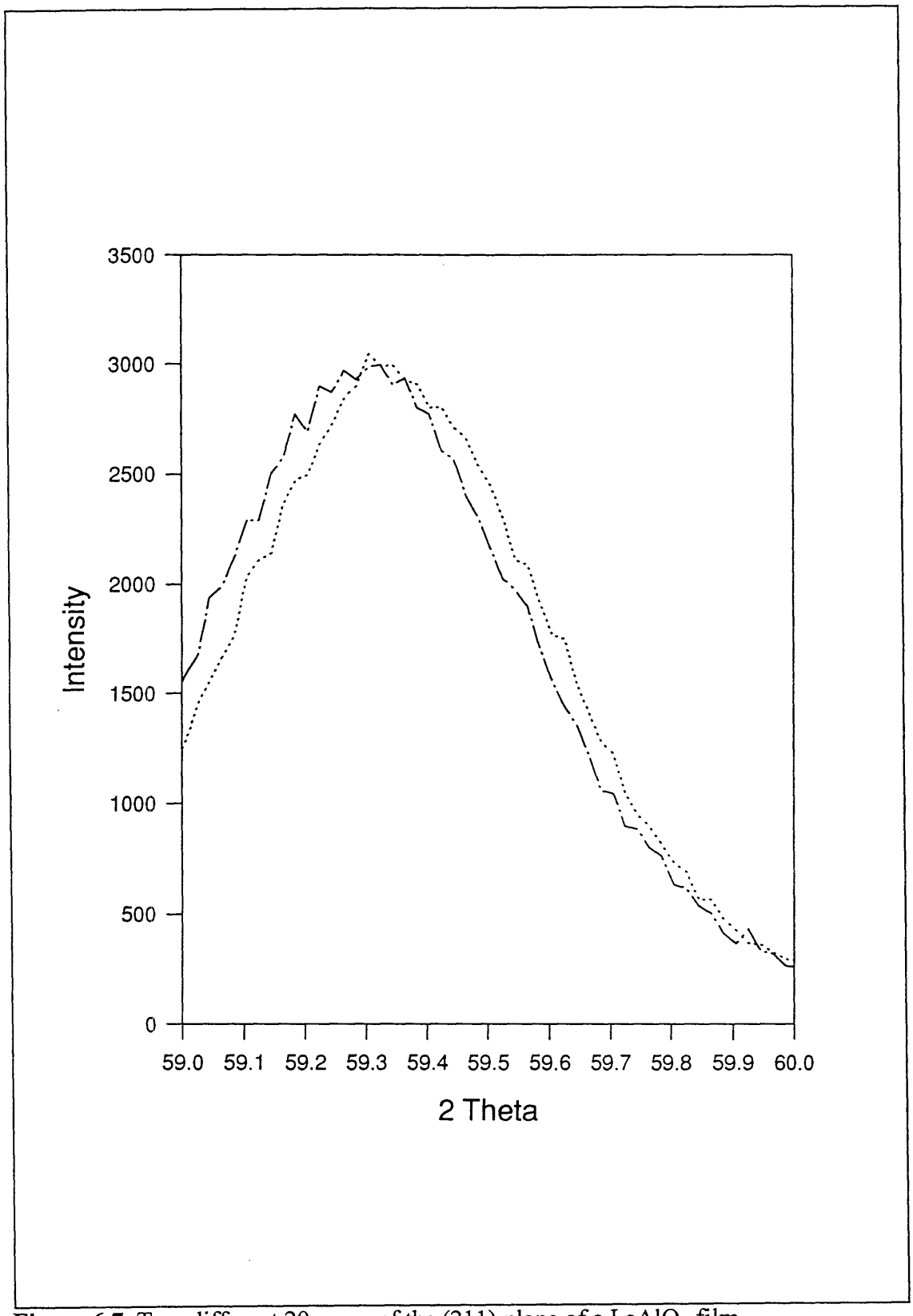

Figure 6.7 Two different 2θ scans of the (211) plane of a $LaAlO_3$ film.

initially. The nucleation continues until the entire substrate surface is covered with $LaAlO_3$. This produces a Johnson-Mehl-Avrami exponent of transformation between 1.4 to 1.5. The $LaAlO_3$ growth interface is rough. The effective activation energy is about 5.1 eV. Pores are left behind due to volume change from the crystallization. The growth of the film is relatively fast such that pores are left behind. The process is schematically illustrated in Figure 6.8.

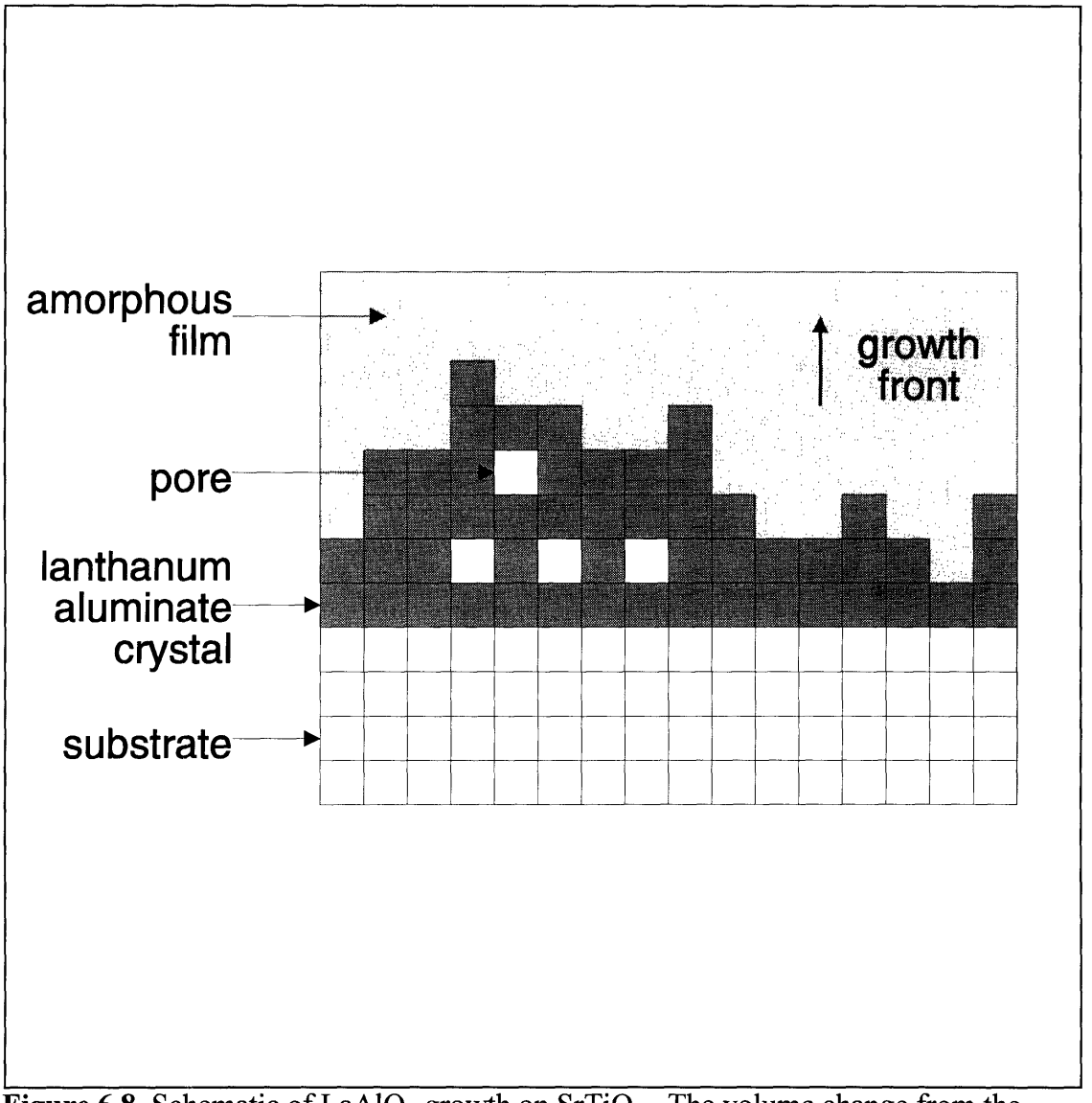

Figure 6.8 Schematic of $LaAlO_3$ growth on $SrTiO_3$. The volume change from the amorphous phase to $LaAlO_3$ is known exactly. Estimated change is approximately -13 to -27%. The fast growing crystal front sweeps through the film and leaves the pores behind.

CHAPTER 7
POTENTIAL APPLICATIONS OF NITRATES DERIVED FILMS IN BYC DEVICES

7.1 INTRODUCTION

One of the technological objectives of this thesis is to develop a spin-on technique to deposit epitaxial dielectric films for HTSC multichip modules. This chapter discusses the feasibility of using these films in actual BYC devices. Three sets of experiments were performed to determine if these films have potential applications. The first set of experiments was deposition of BYC films on the nitrates-derived $LaAlO_3$ films and examination of the properties of the resultant BYC films. High quality dielectric films should produce BYC films with qualities approaching those on single-crystal substrates. BYC films were not deposited on spinel films because spinel reacts with BYC at high temperature. The second set of experiments involved epitaxial planarization of trenched substrates by nitrates-derived films. The last set of experiments was a combined test in which BYC films were deposited on planarized surfaces.

7.2 EXPERIMENTAL PROCEDURE

7.2.1 Fabricating Trenched Substrates

The trenched $SrTiO_3$ and $LaAlO_3$ substrates were prepared by photolithography and subsequent ion milling. Planar $LaAlO_3$ and $SrTiO_3$ substrates were first cleaned with the same cleaning procedure used in film deposition (see Chapter 4). Shipley-1813 photoresist was spin-coated for 30 s at 4000 rpm onto the cleaned substrates. Then they were placed in oven for a 90°C soft bake for 25 min to cross-link the photoresist polymers. Later the samples were exposed to ultraviolet light for 10 s at 8 mW/cm^2 and 365 nm wavelength in a Karl Suss Model MJB3 contact mask aligner. The mask was a clear glass mask with chrome patterns made by DuPont Photomasks, Inc. The pattern of the mask consists of 3 μm wide and 3 μm spacing grating. This pattern was chosen because it is more difficult to planarize it than some patterns with only a few isolated steps or trenches. This would provide a more rigorous planarization test. Samples were placed in a beaker of Shipley CD-30 developing solution for 20 s after exposure

followed by rinsing in deionized water and drying in filtered nitrogen. This procedure was followed by another 25 min bake at 90°C.

Ion etching of the trenches was performed by the researchers at the IBM T.J. Watson Research Center at Yorktown Heights, NY. The substrates were mounted with thermal-grease on a mounting block in the ion etching chamber. Etching was performed with a Kaufmann-type ion source with argon ions at an energy of 500 eV. The ion etching was performed in cycles of a 5 min milling followed by a 5 min cooling time to avoid overheating to the photoresist. The total net ion etching time was 30 min. The substrates were cleaned in an ultrasonic bath of xylene for 5 min upon completion of the etching to remove the residual thermal grease. The steps were 3 μm wide and 3 μm apart, with depth of the step height approximately 1000-1400Å. The trenched substrates were ultrasonicated in acetone and methanol in the same method as described for the planar substrates before deposition of films.

7.2.2 Deposition of Nitrate-Derived Films on Trenched Substrates

A multiple-coating method was used to make nitrates-derived films thick enough for planarization. This was necessary to avoid cracking or using extremely long heat treatment. The normal first layer was deposited and pyrolyzed. The film surface was re-cleaned by using methanol and Kimwipes in a laminar flow hood and inspected to remove any dust particles after the previous layer of film was pyrolyzed. The samples were then spin-coated as in the previous cycle. SEM and profilometry were done on the trenched surface to measure the depth of the trenches.

7.2.3 BYC Film Deposition

BYC films that were deposited on the $LaAlO_3$ epitaxial films were made from metalorganic deposition (MOD) of metal trifluoroacetate (TFA) precursors developed in this laboratory (McIntyre, 1993; Smith, 1995). Stoichiometric amounts of yttrium, barium, and copper acetates were mixed and dissolved in deionized water. The solution was dried to a sticky, blue residue. The residue was then diluted in methanol and filtered with a 0.22 μm ceramic tip filter to produce the precursor solution. The precursor solution was spin-coated on (100) single-crystal $LaAlO_3$ substrates or on nitrates-derived $LaAlO_3$ films (on either $SrTiO_3$ or $LaAlO_3$ substrates). The spin coating condition was 120 s at 4000 rpm with a 0.4 s acceleration time to reach the final spinning speed. The spin-coating was performed in a laminar flow hood to prevent any

dust particles from falling on the films. Spin-coating was performed only when the relative humidity of the atmosphere was below 35%, as to avoid dewetting of the TFA precursor due to its hygroscopic nature. The samples were quickly transferred to a CM 2200 horizontal furnace for a low temperature firing after spin-coating. The moist atmosphere used in pyrolysis was produced by bubbling the gas through two water reservoirs maintained at room temperature. The relative humidity of the moist gas was close to 100%. The heating schedule is shown in Fig. 7.1. This process pyrolyzed the metal TFA first into a mixture of oxyfluorides (Ng, 1992).

A high-temperature heat treatment was used to convert the oxyfluorides to BYC. Moisture was introduced in the pyrolysis atmosphere to decompose BaF_2 into BaO and form the BYC film. The atmosphere was a mixture of nitrogen and oxygen to maintain a specific oxygen partial pressure. A fast ramp rate of 25°C/min and a humid atmosphere from the onset was needed to prevent the coarsening of barium fluoride particles (Ng, 1992). The heating schedule is shown in Fig. 7.2.

7.2.4 Characterization of Films

The transport electrical properties were measured by a standard four-point probe technique. Four silver pads were evaporated on the BYC films to provide better contact with the lead wires. An aluminum foil mask was used to protect the rest of the film (except for the four parallel pads) from silver. A 30 min anneal at 450°C in an oxygen atmosphere was used to improve the silver pads adhesion to the BYC. Then the sample was glued to a chip carrier. Aluminum lead wires (0.025 mm diameter) were ultrasonically wire-bonded to connect the silver pads to the gold pads of the chip carrier. Copper wires connected the chip carrier to a thermometer probe. The probe was inserted slowly into a liquid helium dewar to reduce the temperature. A testing current of 10 μA alternating every 5 s was used to eliminate the effect of thermal-induced voltage. The critical temperature was determined when the voltage across the middle two pads was reduced to less than 10^{-7} V.

At least one control sample using single-crystal $LaAlO_3$ substrate was also made with every run to compare the performance/microstructure of BYC films on nitrates-derived $LaAlO_3$ films with those on single-crystal substrates. Samples that were tested for electrical properties were scribed to define a narrow region when the films were still in oxyfluoride form (Fig. 7.3). There are two purposes for this scribing. First the edges of MOD films are typically much thicker than the center due to the edge effect from spin-coating. A narrow region in the center of the film can ensure a more uniform

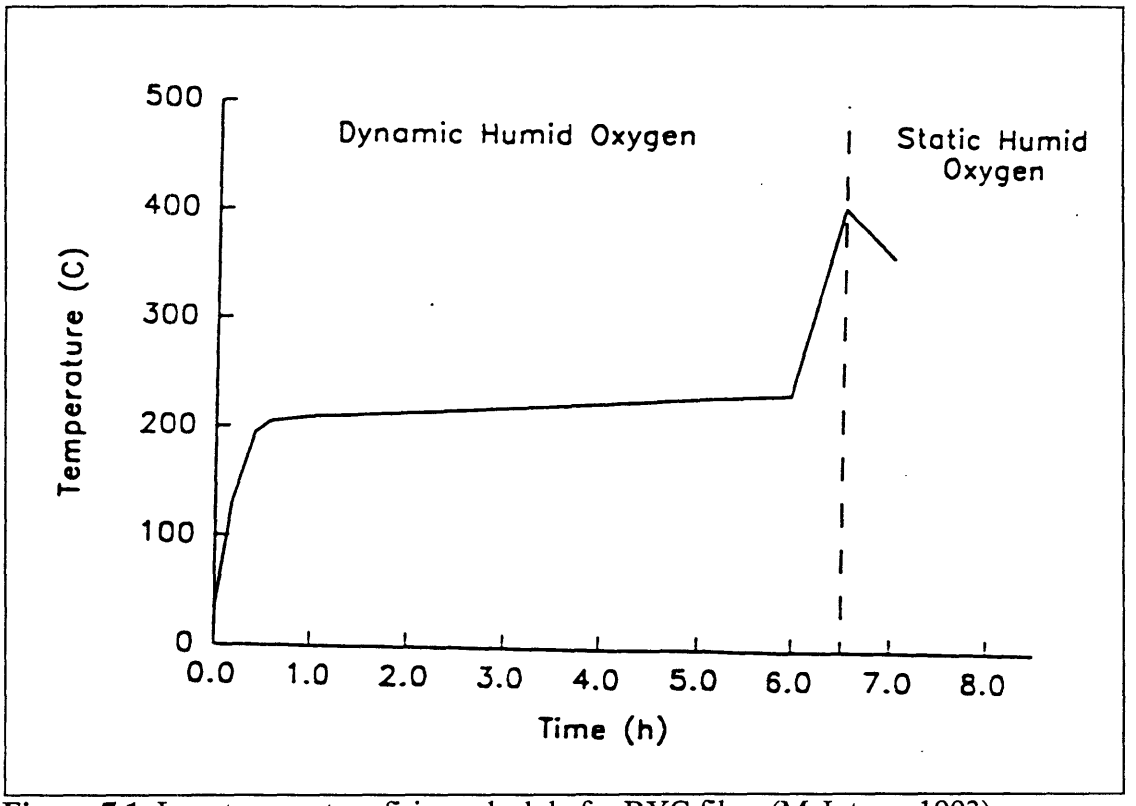

Figure 7.1 Low temperature firing schedule for BYC films (McIntyre, 1993).

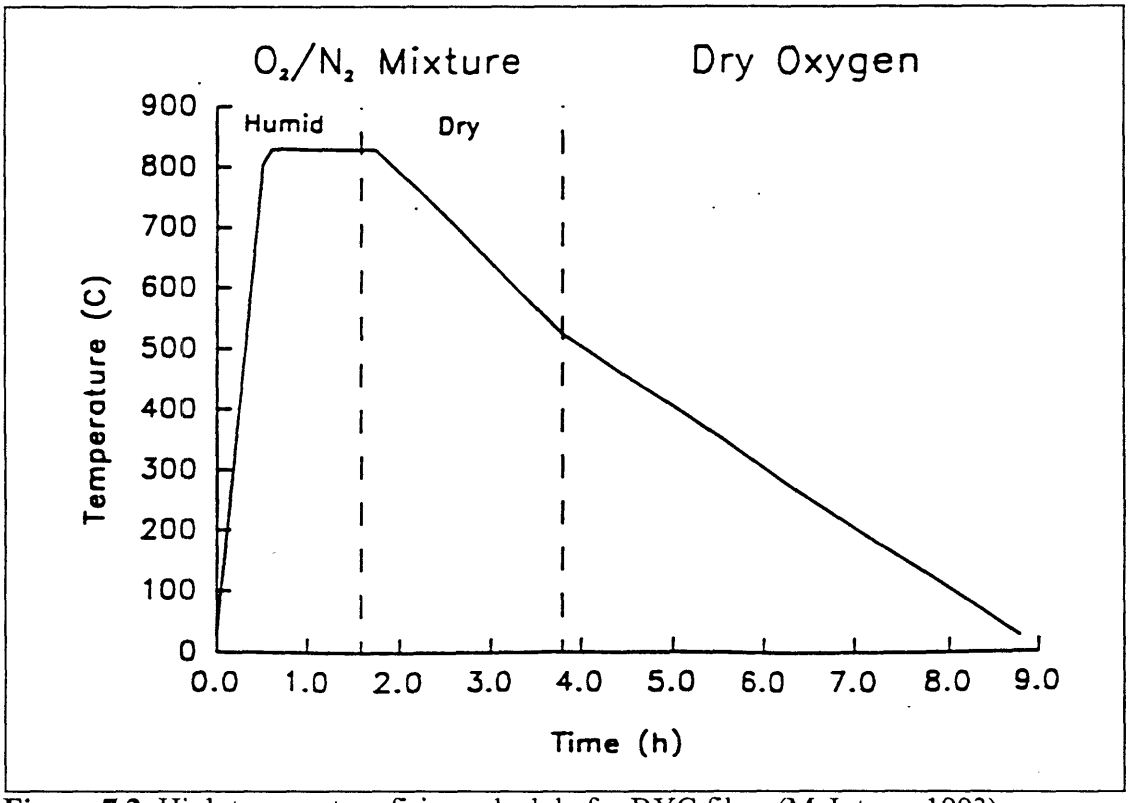

Figure 7.2 High temperature firing schedule for BYC films (McIntyre, 1993).

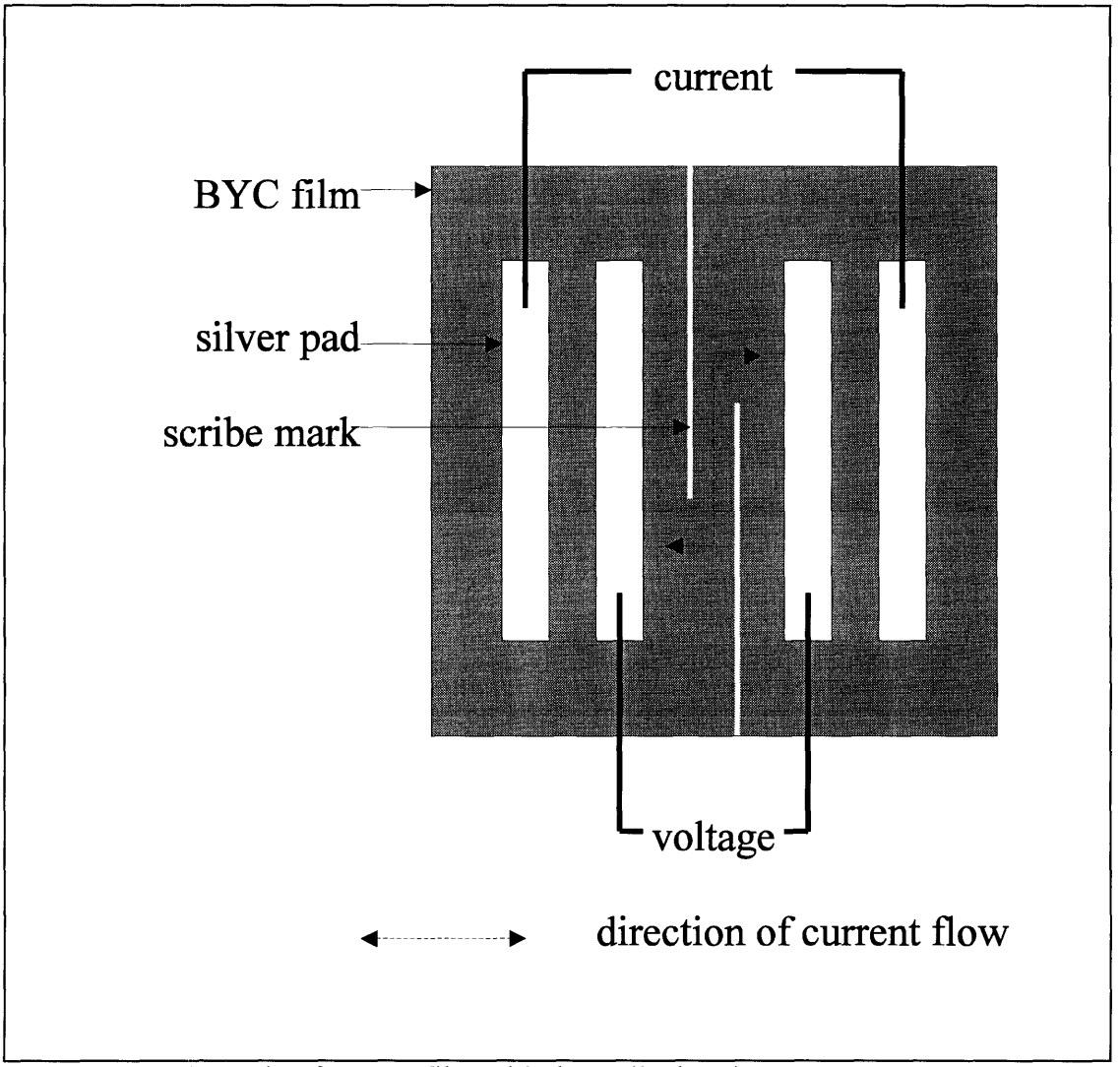

Figure 7.3 Schematic of a BYC film with the scribed region.

thickness of the current path. Secondly the scribe region has a narrow width which reduces the amount of test current needed to drive the region from superconducting state to normal state. Smaller test current can reduce the problem of local heating at the silver pads or the aluminum contact wires. A typical scribed path is 150-300 μm wide and 1000-3000 μm long.

The critical current densities were measured in a similar method. The probe was inside a liquid helium dewar also. The position of the probe was controlled to maintain a constant temperature of 77.3 K during testing. The critical current density was calculated by using the average thickness of the scribed region (observed under cross-sectional SEM) and assumed full density of BYC. Current was increased until a voltage increase of more than 10^{-6} V was detected.

7.3 PLANARIZATION

Planarization on stepped surfaces had been done in fabrication of electronic devices by RF sputtering of aluminum and silica. Their capability to planarize surfaces had been demonstrated (C.Y. Ting, 1978; C.H. Ting, 1982; and Bader, 1985). Spin-on techniques such as phosphosilicate glass have also been used in planarization (Ghandhi, 1983). These planarized layers, however, were not epitaxial. The dielectric layers for BYC devices must both planarize and remain epitaxial. There had also been work in epitaxial planarization of semiconductors (Tate, 1988; Turco, 1990; and Galeuchet, 1991). Most of the semiconductor epitaxial planarization involves two mechanisms. The first one is the difference in the growth rate in different crystallographic orientation of different facets. The second one is the geometric factor that governs the effective incident flux of materials deposited. These techniques work in III-V semiconductors. Epitaxial planarization of oxide layers for BYC devices has only been investigated recently by using ion beam assisted deposition of CeO_2 films (Chang, 1994b). The spin-on technique has the potential to produce epitaxial planarized layers of oxides.

The results for epitaxial planarization were very similar in both $LaAlO_3$ and spinel films. There were several problems encountered during planarization of trenched substrates. One initial problem was cracking. The steps served as nucleation sites for cracks. Cracks propagated along the trenches (Fig. 7.4). Slower heating rate and thinner individual layers in each firing cycle were used to prevent cracking in the films. The wetting of the precursor may also be a problem. Pores with size similar to the step height were observed near edge of steps (Fig. 7.5). This may pose a problem in the physical integrity of the film even though the voids may not affect the general

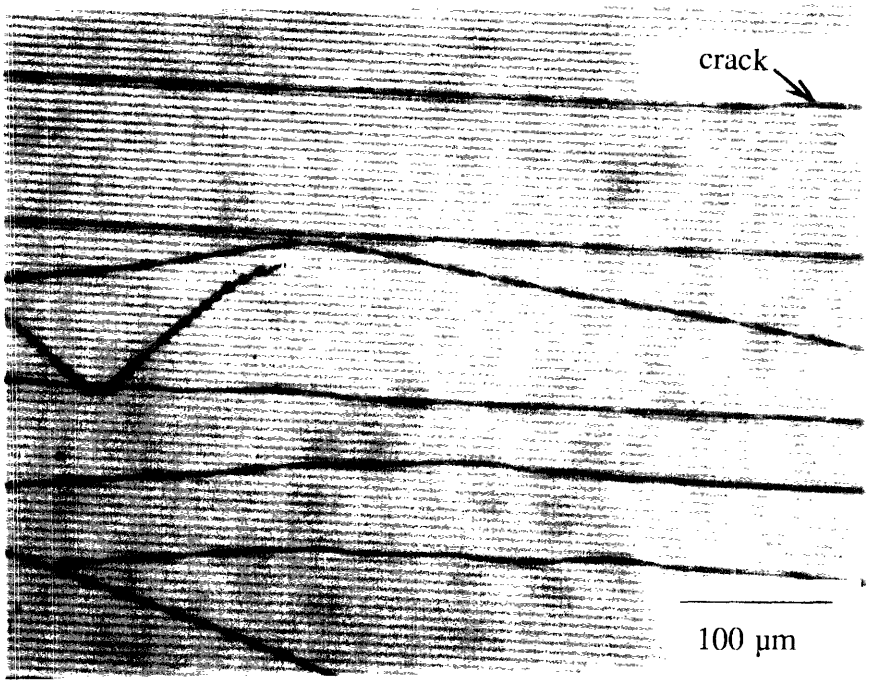

Figure 7.4 Optical micrograph showing cracking of a $LaAlO_3$ film on a stepped $SrTiO_3$ substrate.

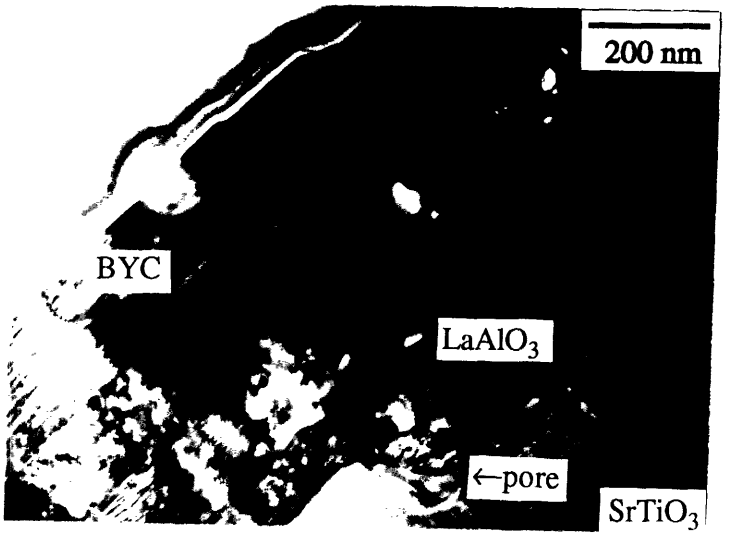

Figure 7.5 Cross sectional SEM of a $LaAlO_3$ film on a stepped substrate, showing a void near the step.

crystallinity of the film. The other problem was the incomplete planarization of the trenches (Fig. 7.6). The nitrates-derived films smoothed off and reduced the depth of the trenches. It had, however, some element of conformal coverage. This indicated that many layers were needed for complete planarization. One thick layer, however, could fully planarize certain nonplanar surfaces where steps and trenches were far apart (Fig. 7.7). All the films were epitaxial even on stepped substrates, as confirmed by XRD spectra of $LaAlO_3$ on trenched $SrTiO_3$ (Fig. 7.8).

7.4 BYC FILMS ON LANTHANUM ALUMINATE FILMS

The performance of the BYC films depends on the quality of the underlying substrates or dielectric films. The electrical properties of the BYC films can indirectly indicate qualities of the underlying the $LaAlO_3$ films (Warner, 1990). A typical TFA-derived BYC film on a single-crystal $LaAlO_3$ substrate has T_c above 92 K (McIntyre, 1993). The extrapolation of the slope of the temperature vs. resistivity curve intercepts the resistivity-axis at a point of negative resistivity (below the origin). The room temperature resistivity is approximately 300 $\mu\Omega$-cm (Fig. 7.9a). The critical current density at 77 K is above 5×10^6 A/cm^2.

Most of the TFA-derived BYC films on nitrates-derived $LaAlO_3$ films had T_c above 92 K also. The extrapolation of slope of the temperature vs. resistivity curve, however, did not intercept the resistivity-axis below the origin as in the TFA-derived films, but close to or above the origin (Fig. 7.9b). Currently there is no consensus on the relation between quality of BYC films and y-intercept of the extrapolation of the temperature vs. resistivity plot. The common thinking is that if the slope intercepts the y-axis above origin, the electrical properties are not as good (Allen, 1989).

The BYC films that were deposited on nitrates-derived $LaAlO_3$ films on either single- crystal $LaAlO_3$ or $SrTiO_3$ substrates had features different from those deposited directly on single-crystal $LaAlO_3$. The surface morphologies of these films as observed by SEM showed that that were many more elongated grains that protruded out of the surface and were mutually perpendicular to each other (Fig. 7.10). Those were a-axis BYC grains. (The a- and b- axis grains are grouped together in this thesis because of their similar parameters.) It was also observed from XRD spectra that there were high densities of a-axis grains. XRD of the BYC film showed that the (005) reflection had a FWHM of 0.224° θ. The BYC films grown on chemically derived $LaAlO_3$ films had higher density of a-axis grains compared to those grown on single-crystal $LaAlO_3$ substrates. The density of a-axis grains in BYC films deposited on single-crystal

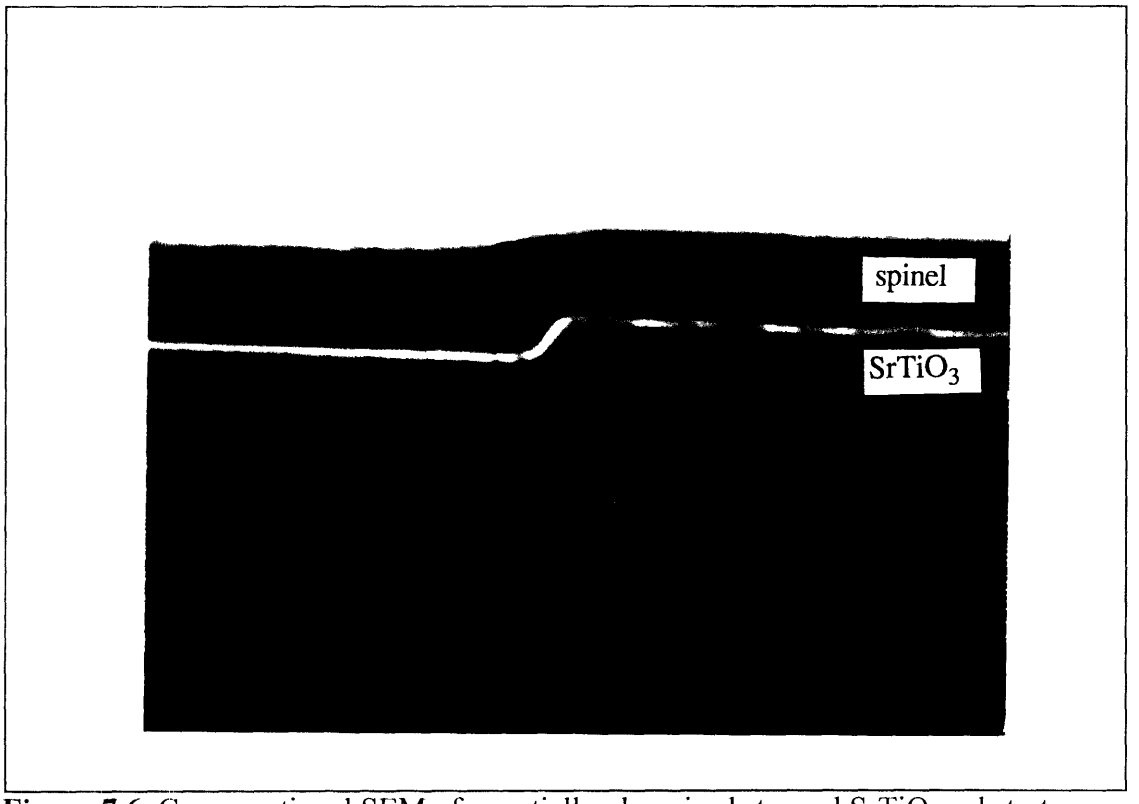

Figure 7.6 Cross sectional SEM of a partially planarized stepped $SrTiO_3$ substrate.

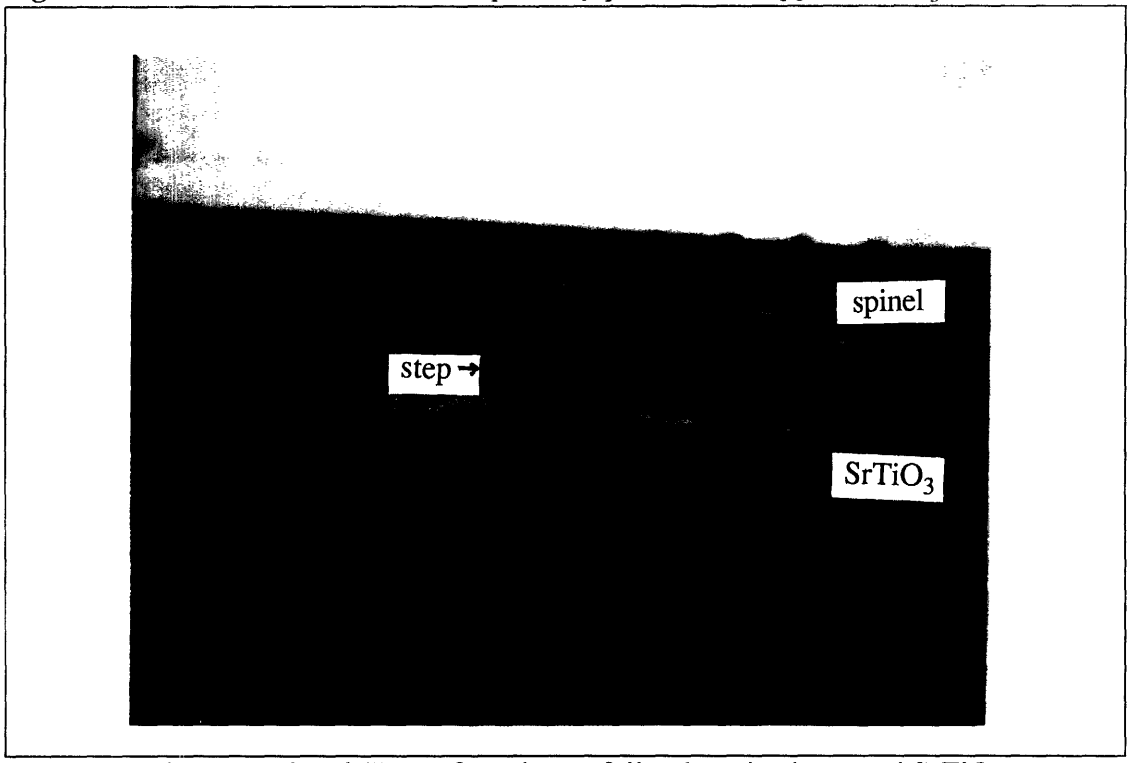

Figure 7.7 Cross sectional SEM of an almost fully planarized stepped $SrTiO_3$ substrate.

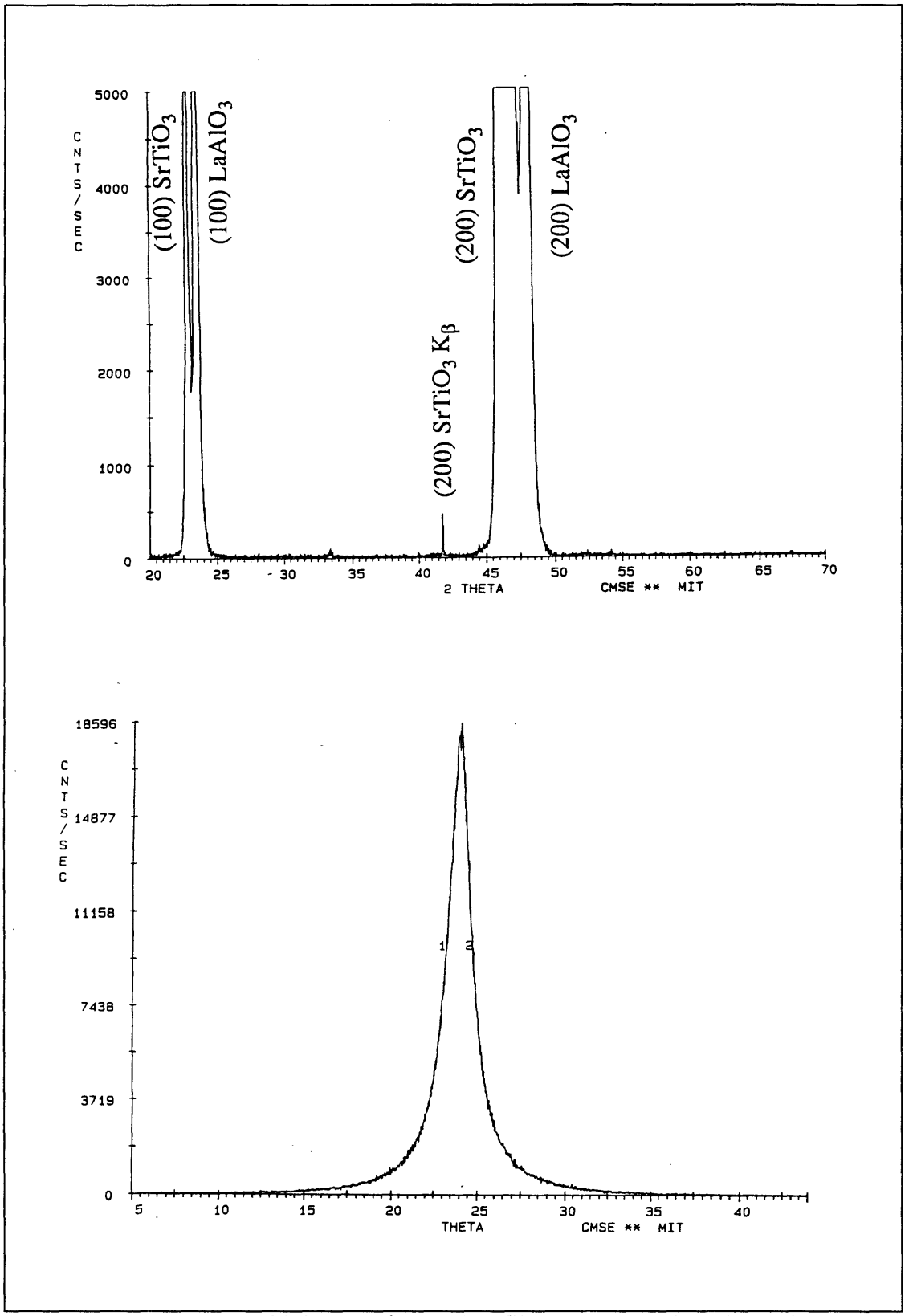

Figure 7.8 XRD: top (a) θ/2θ scan of a $LaAlO_3$ film on a stepped $SrTiO_3$ substrate, and bottom (b) (200) rocking curve of the same film.

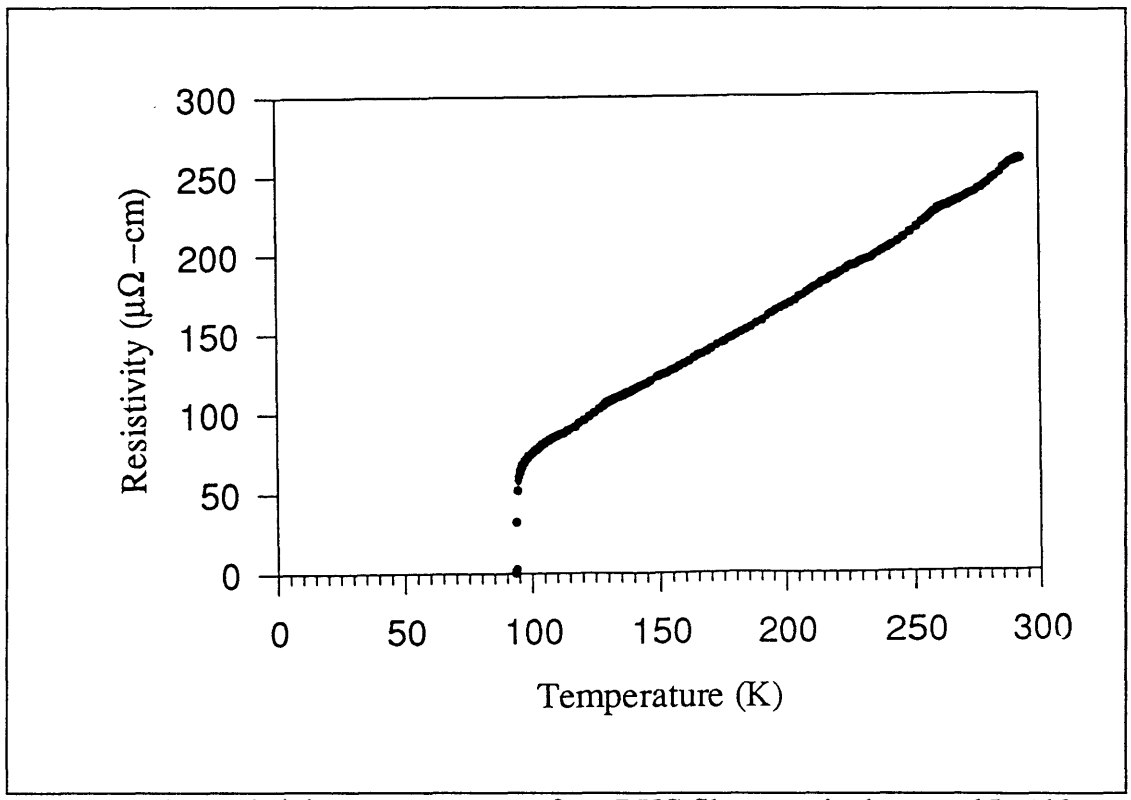

Figure 7.9 (a) Resistivity vs. temperature for a BYC film on a single crystal $LaAlO_3$ substrate.

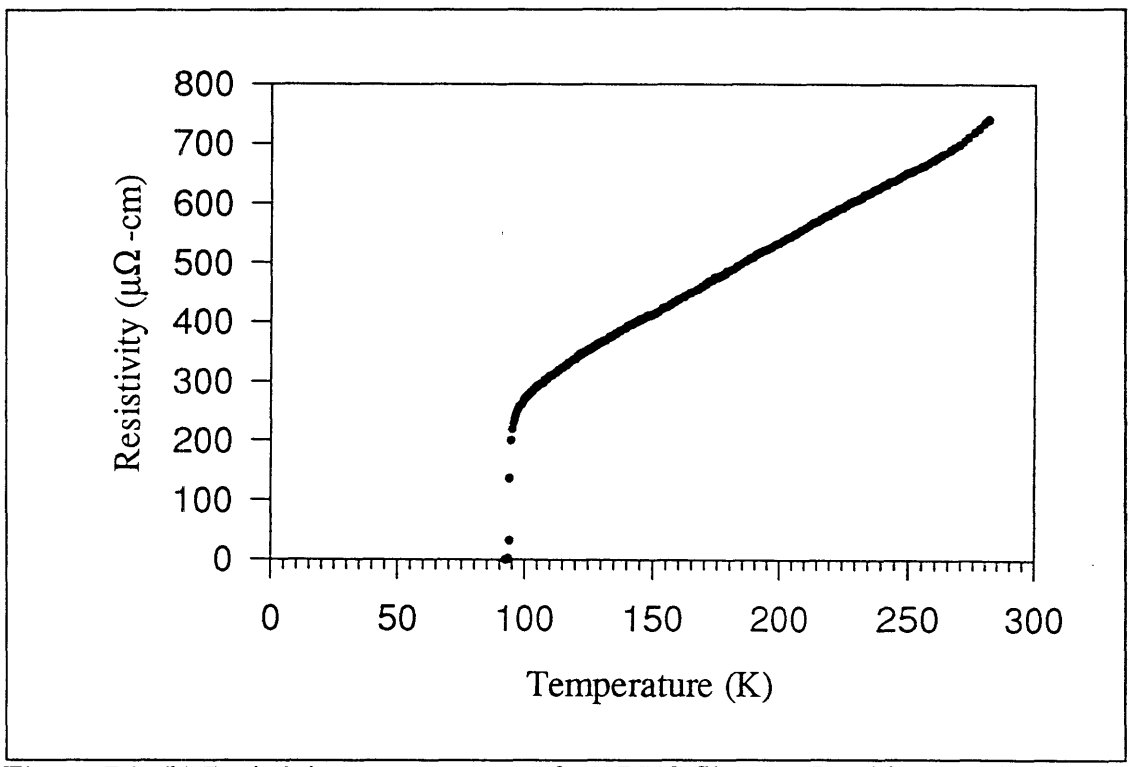

Figure 7.9 (b) Resistivity vs. temperature for a BYC film on a $LaAlO_3$ on a single crystal $SrTiO_3$ substrate.

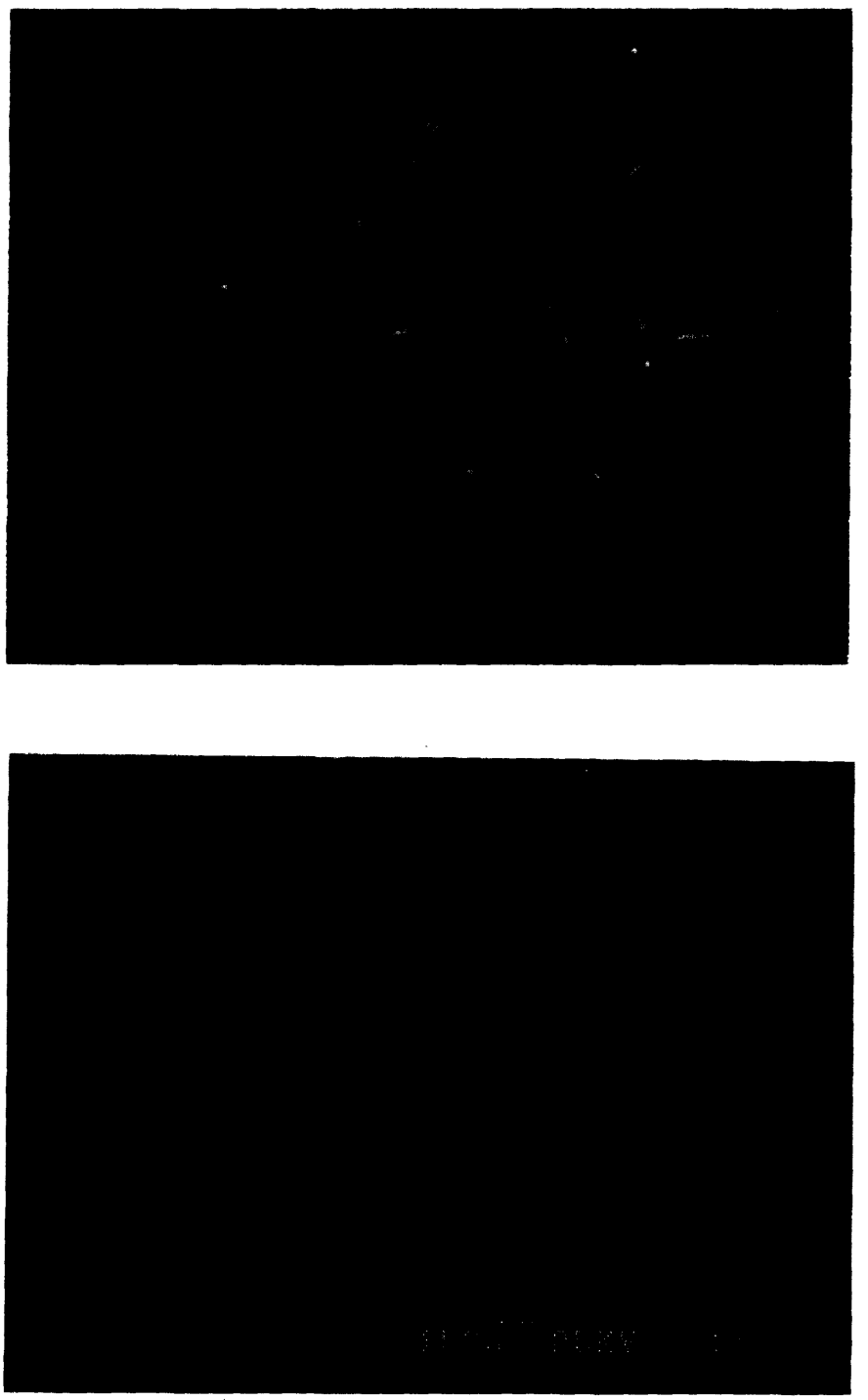

Figure 7.10 (a) SEM of a BYC film on a single crystal $LaAlO_3$ substrate (top: 5000 X magnification, bottom: 20000 X magnification).

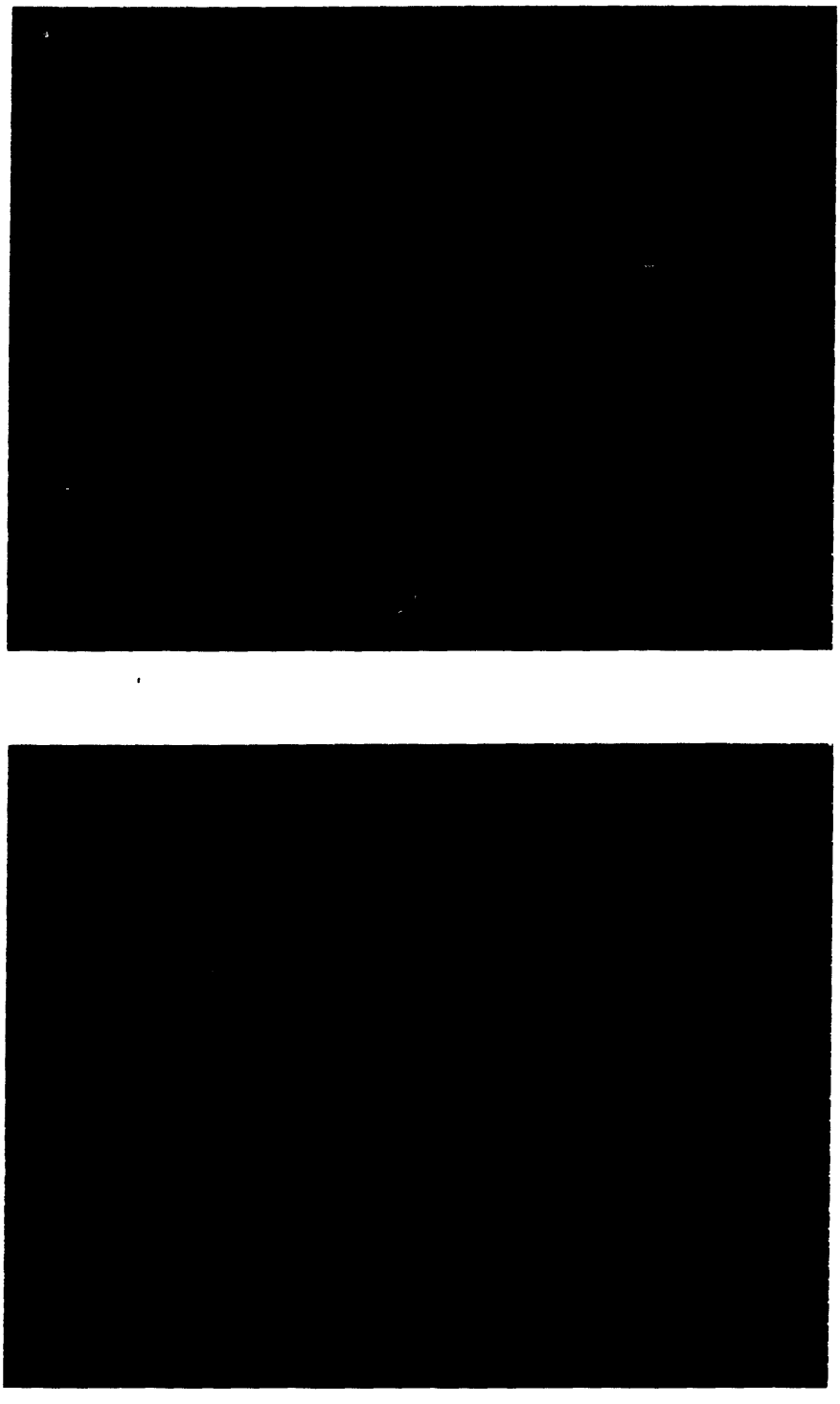

Figure 7.10 (b) SEM of a BYC film on a $LaAlO_3$ film on a single crystal $SrTiO_3$ substrate (top: 5000 X magnification, bottom: 20000 X magnification).

$LaAlO_3$ substrates was approximately 2 per 375 μm^2, as counted from the SEM micrograph. The density of a-axis grains was approximately 130 per 375 μm^2 for BYC films on nitrates-derived $LaAlO_3$ films. The increased density of a-axis grains can be attributed to the increased number of steps from the surface roughness. The nucleation of BYC grains on the substrate surface involved a three-fold degeneracy in nucleation of a-, b-, and c-axis grains (Chan, 1989). The BYC grains grew the fastest in the a- and b-directions. In a thin film the fast growing axes of grains with their a- or b-axis normal to the substrate would stop growing once they had reached the top surface of the film. The grains with their c-axis normal to the substrate surface, however, had more room to grow in their fastest growing directions. The end results would be the dominance of the c-axis grains (Fig. 7.11). There would be more nucleation and thus more a-axis grains if there were more nucleation sites. The number of sites BYC grains nucleated under certain processing conditions could be deduced from the a-axis grain density. It was assumed that there were two a-axis grains and one c-axis grain for every three nucleation sites. A quick survey from the SEM micrographs in Fig. 7.10 gave a rough estimation of the number of nucleation sites available in the processing conditions used in BYC deposition. There were three nucleation sites per 375 μm^2 of area on a $LaAlO_3$ single-crystal substrate. There were approximately 195 nucleation sites per 375 μm^2 of area on a nitrates-derived $LaAlO_3$ film. The a-axis grains caused a decrease in critical current density. The general observation was that higher density of a-axis grains lowered the J_c. It should be considered, however, that the heat treatment used in this study was not be optimized for nitrates-derived $LaAlO_3$ surfaces. A lower temperature treatment may be able to reduce the overall nucleation density (and thus the number of a-axis grains).

The BYC films had higher critical current densities when they were deposited on $LaAlO_3$ films that were heated for shorter time. The best BYC films were deposited on $LaAlO_3$ that had a ramp time of 3 h 25 min and held for 2 h at 750°C. The J_c's were above 2 x 10^6 A/cm^2 at 77.3 K. An additional 2 h at 800°C annealing for $LaAlO_3$ films prior to BYC deposition actually caused the BYC films to have lower J_c. The worst BYC films were those that were deposited on $LaAlO_3$ films with the longest annealing time. One explanation is that longer heat treatment roughened the surface and increased the BYC nucleation. The explanation is that the ramp time was related to surface roughness (Chapter 4). Rougher $LaAlO_3$ films produced more a-axis grains. They led to more high angle grain boundaries that degraded the transport J_c.

It is interesting to notice that the substrate material, whether it was $SrTiO_3$ or $LaAlO_3$, did not have a major impact on the electrical properties of the BYC films on

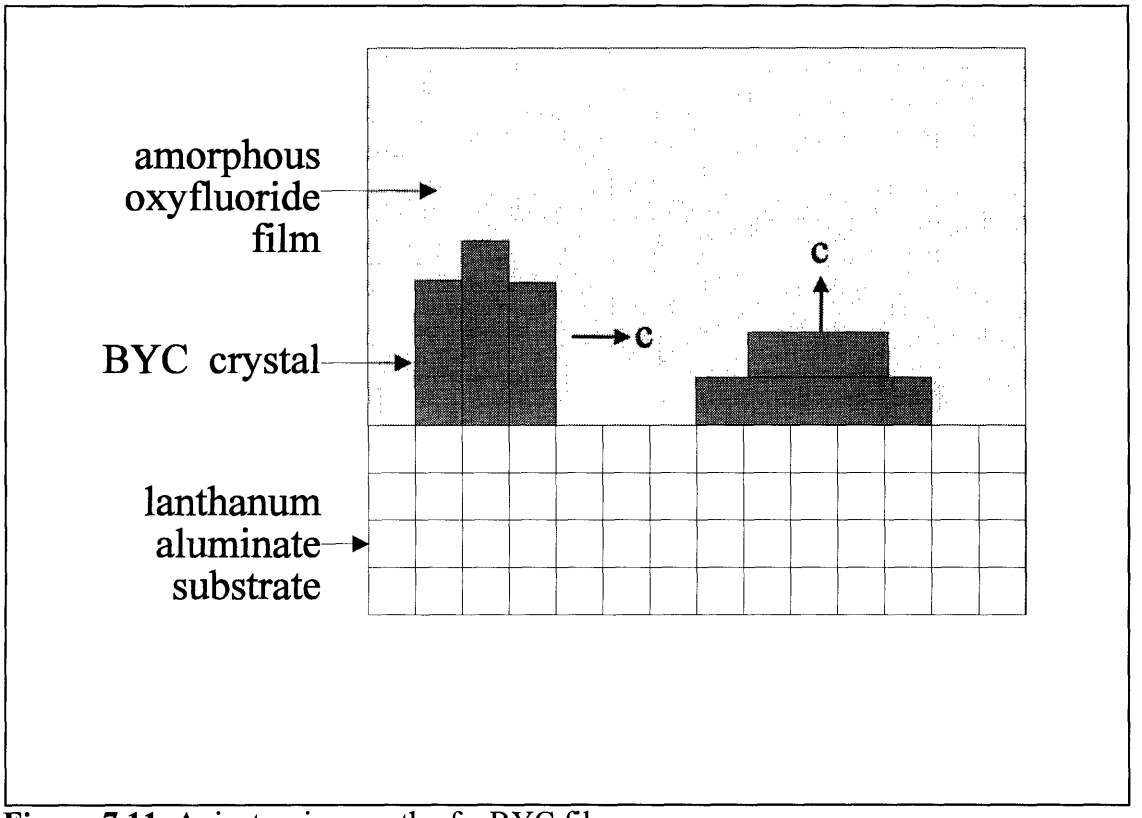

Figure 7.11 Anisotropic growth of a BYC film.

nitrates-derived $LaAlO_3$ epitaxial layer. This indicated that the quality of lanthanum aluminate films from heteroepitaxy could be as good as those from homoepitaxy. BYC could be deposited on $LaAlO_3$ films as thick as 0.7 μm.

TEM micrographs of BYC‖$LaAlO_3$‖$LaAlO_3$ showed that there were pores inside the $LaAlO_3$ layer (Fig. 7.12). These materials inside the pores, judged from the lattice parameters, were BYC. The most likely explanation for the infiltration of BYC is that a liquid phase was formed during high temperature firing of the oxyfluoride films (McIntyre, 1993). This liquid phase filled up the pores. It is unlikely that when the liquid TFA precursors were spin-coated on the surface, some of the liquid infiltrated inside the $LaAlO_3$ films. The precursor would have undergone volume change and would not fill up the entire pore if it was from percolation of liquid precursors during spin-coating.

The presence of pores raises up a possibility that BYC may not have really grown on the epitaxial $LaAlO_3$ but instead on the underlying single-crystal as the percolated liquid phase nucleated on the single crystal substrate. This argument was refuted by the properties of BYC films deposited on $LaAlO_3$ films made from three different heating treatments. The $LaAlO_3$ films were heated to 750°C and held for 0 h, 1 h and 2 h, respectively. XRD patterns of all three films showed epitaxial $LaAlO_3$ phase. BYC film was not formed on the layer that had been raised at 750°C but quenched immediately. High quality BYC films were formed on $LaAlO_3$ films that were held for 1 or 2 h. Results in Chapter 6 suggested that the surface of the 0 h annealing films were not yet fully crystallized for BYC deposition. This suggested that the quality of the $LaAlO_3$ surface is important to obtain good MOD BYC and the BYC films were formed due to the epitaxial $LaAlO_3$ films.

Epitaxial BYC films could be deposited on these $LaAlO_3$ films with no difficulties even though the final films were porous. The porosity can reduce the overall dielectric constant of the film because the pores have dielectric constant of 1. The actual dielectric constant of the film can be lower than the bulk dielectric constants of 8.3 and 23 for $LaAlO_3$ and spinel, respectively. These chemically derived films, therefore, may be suitable in dielectric layers. The open porosity poses a potential problem in which different BYC layers may be shorted. The challenge is to form a dense skin layer that prevents the shorting but maintains the porosity for the bulk of the film.

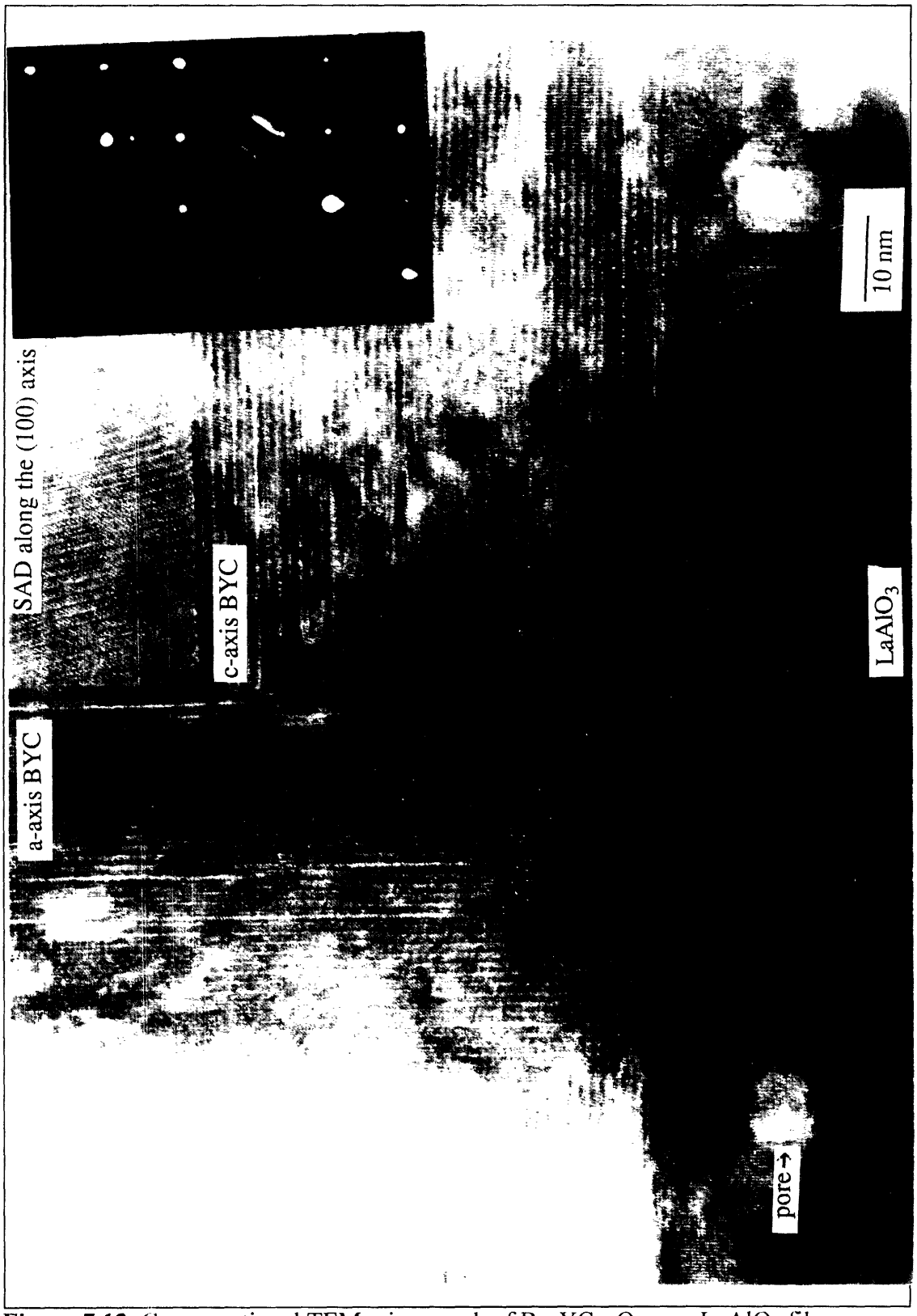

Figure 7.12 Cross-sectional TEM micrograph of $Ba_2YCu_3O_{7-x}$ on $LaAlO_3$ film on a single-crystal $SrTiO_3$ substrate.

7.5 BYC ON PLANARIZED SURFACES

This set of experiments attempted to deposit high qualities BYC films on planarized surfaces. A control sample was made with BYC film on a trenched $SrTiO_3$ single-crystal substrate. Results from electrical properties testing showed that the test current could not pass through the scribed region. This can be due to the discontinuity in the film. The SEM micrographs (Fig. 7.13) showed that along with edge of the trenches there are tracks of a-axis grains.

The final test of epitaxial planarization was to deposited BYC on planarized surfaces. A $SrTiO_3$ substrate which had been milled to have trenches of depth 1400 Å was partially planarized with a $LaAlO_3$ layer approximately 0.38 μm thick. The 1400 Å step on the substrate was smoothened to approximately 700 Å deep. The TEM micrographs showed that there were a- and c-axis BYC grains (Fig. 7.14). It was confirmed by the XRD pattern, which showed only epitaxial BYC and $LaAlO_3$ films (Fig. 7.15). The (005) BYC reflection had a FWHM of 0.245°. The transition temperature was 92 K. The current path was perpendicular to the trenches to make sure that the current passed through many crossovers. The critical current density, however, was close to zero.

The SEM micrographs showed a reduced density of a-axis grains when compared with the BYC films deposited on planar $LaAlO_3$ film (Fig. 7.16). This reduced density of a-axis could be due to fewer nuclei under the same processing condition. The BYC film also did not cover the entire surface. There were many pores visible in the micrographs. This can be attributed to the nonplanarity of the $LaAlO_3$ surface which produced incomplete wetting of the precursor liquid.

Other samples had demonstrated greater extent of planarization. The $LaAlO_3$ layers of these samples were at least a few μm thick. The electrical properties of the BYC films deposited on the thicker dielectric layers were similar to those of semiconducting materials; i.e., the resistivity decreases with temperature. XRD patterns showed that these BYC films were highly oriented. The SEM micrographs, however, showed that there were two different types of surface features. The first was the normal type of surface which showed lots of a-axis grains. The second type of feature did not have a-axis grains. Rather, there were many bumps. The regions of high a-axis grains formed parallel "tracks."

One possible explanation is that part of the $LaAlO_3$ films formed near the trenches was of poorer quality due to the edges of the trenches on which they were nucleated. The heat treatment used for BYC films was designed for lattice-matched substrates.

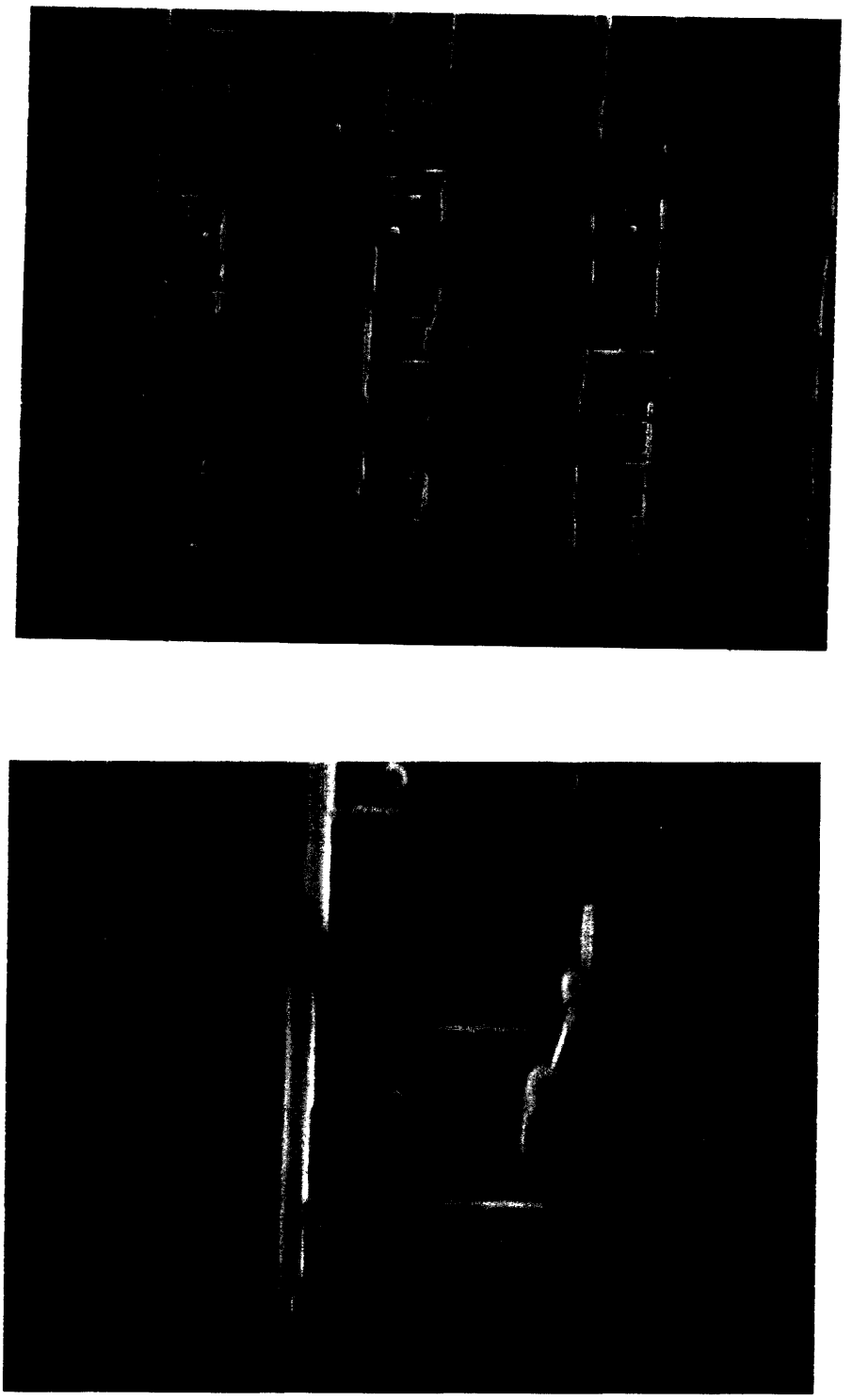

Figure 7.13 SEM micrographs of $Ba_2YCu_3O_{7-x}$ film on a trenched substrate.

Figure 7.14 Cross-sectional TEM micrograph of a BYC film on a partially planarized substrate.

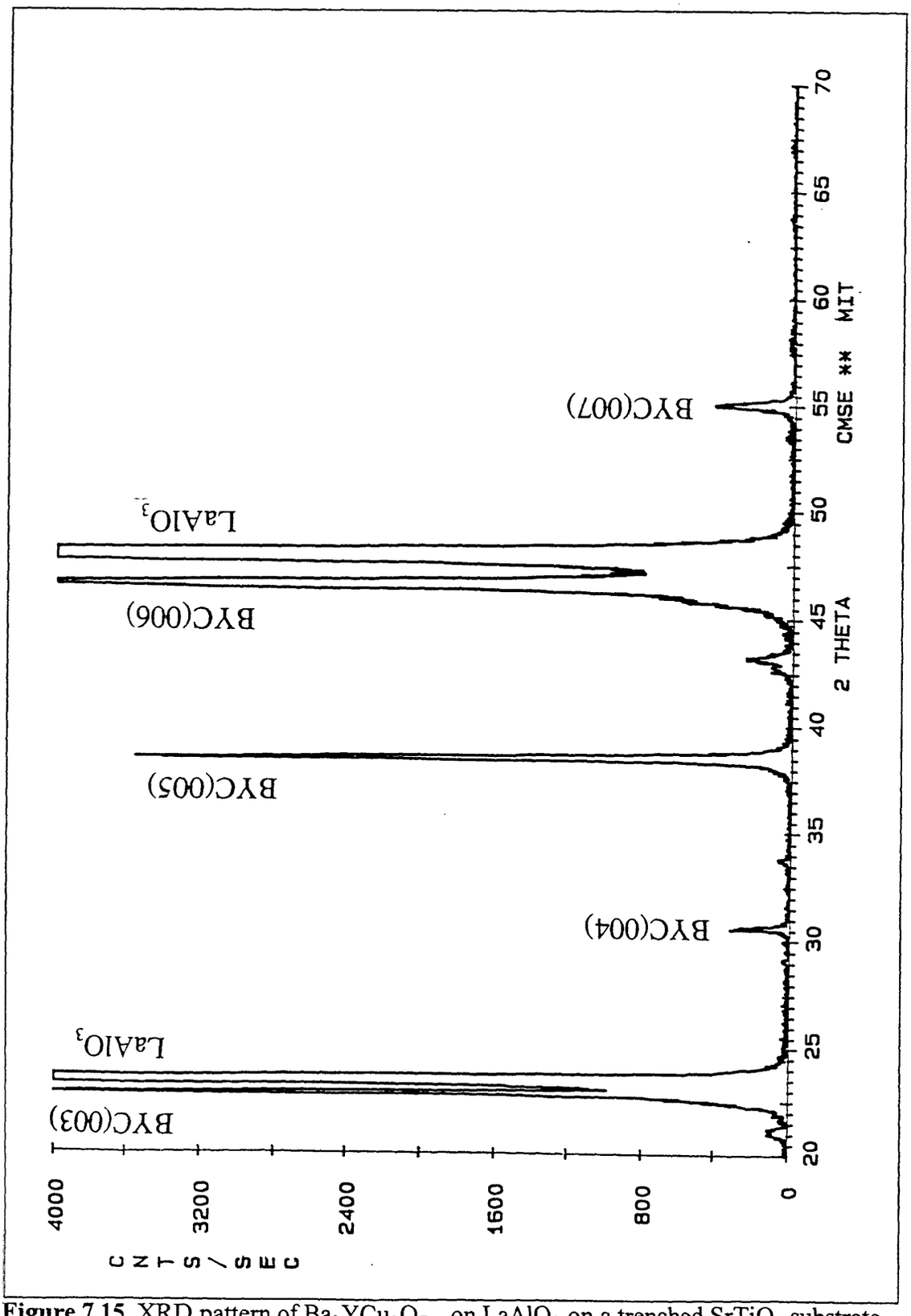

Figure 7.15 XRD pattern of $Ba_2YCu_3O_{7-x}$ on $LaAlO_3$ on a trenched $SrTiO_3$ substrate.

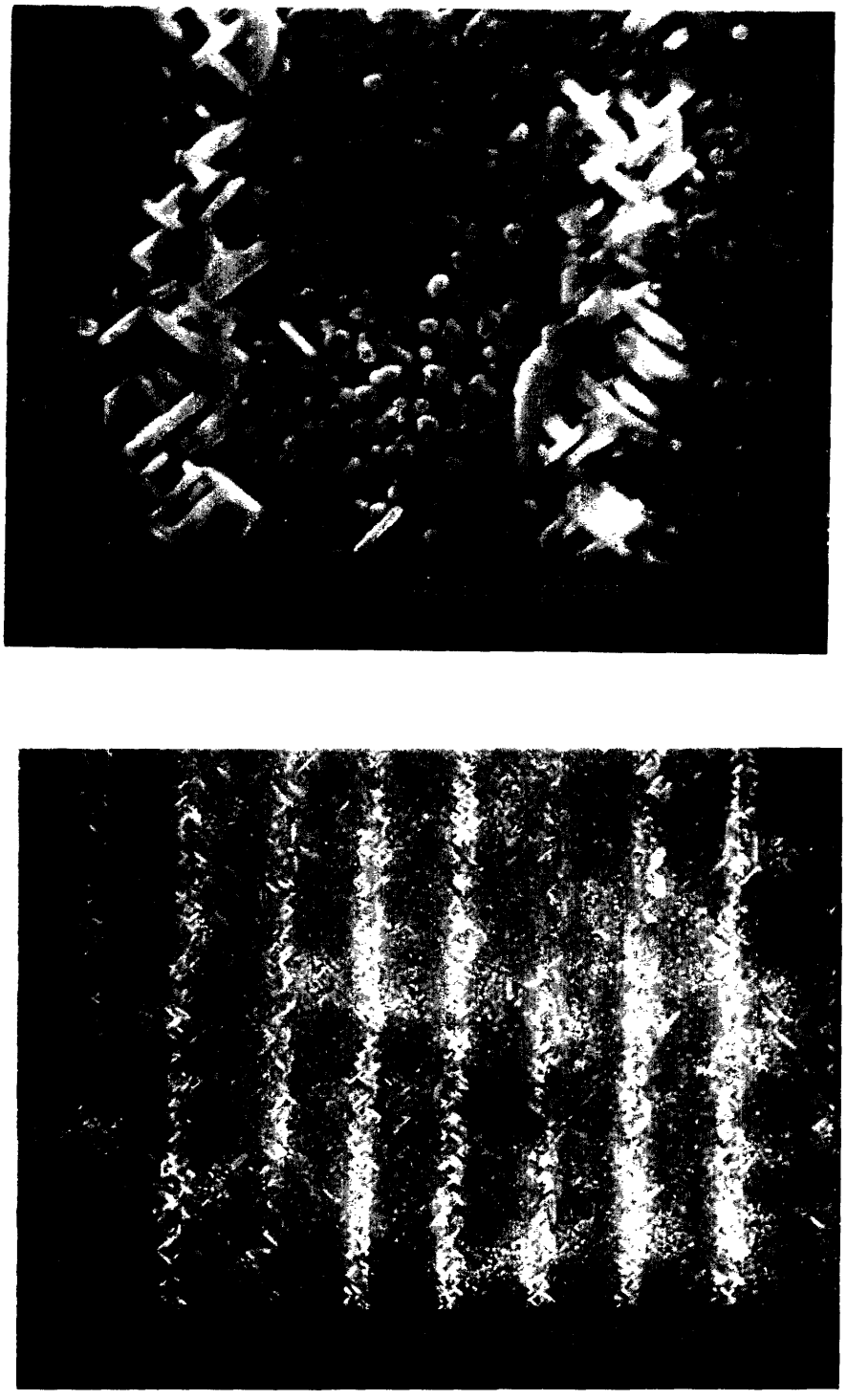

Figure 7.16 SEM micrographs of $Ba_2YCu_3O_{7-x}$ film on a partially planarized substrate.

Only the transient liquid phase was formed on non lattice-matched surface. This liquid phase solidified and did not convert into BYC. Thus, these impurities degraded the electrical properties. The other regions that showed better quality BYC film were likely to be on planarized $LaAlO_3$.

Nitrates-derived films have demonstrated the promises to produce be used in BYC MCM even though this set of experiments has not yet produced high quality BYC films on planarized surfaces. Epitaxial planarization has been demonstrated. The process has not yet been optimized for subsequent planarization

7.6 SUMMARY

Until now, all interlayers in BYC devices are produced by physical vapor deposition methods. This chapter shows that spin-on chemically derived $LaAlO_3$ films can be used as underlying layers for subsequent deposition of BYC films. The critical current densities of these BYC films at 77 K are above 2 x 10^6 A/cm^2. The electrical properties of these BYC films are good enough for practical applications. The BYC films on $LaAlO_3$ layer have more a-axis grains and lower J_c than would be on planar substrate due to the surface roughness.

Partial epitaxial planarization is demonstrated on regularly trenched substrates. Planarization has been more successful on substrates with lower density of trenches or steps. Unlike other available technique, epitaxial planarization by the spin-on method does not depend on the anisotropy of the crystal growth. This leads to broader application than other availabe techniques.

CHAPTER 8
OVERALL CONCLUSIONS AND FUTURE WORK

8.1 CONCLUSIONS

This work is the first attempt to deposit epitaxial thin films for dielectric layers in HTSC multichip modules by spin-on techniques. Epitaxial spinel and $LaAlO_3$ films were successfully deposited by pyrolysis of mixed nitrates and double alkoxide precursors. This work examines the influence of processing conditions on the film microstructures, the mechanism of the epitaxial growth, and the applications of these films in epitaxial planarization and as dielectric layers. This work demonstrates the viability of spin-on approach to deposited multi-cationic epitaxial oxide films.

The decomposition processes of the mixed nitrates and magnesium isopropoxide were examined. Experimental results mainly confirmed the information available in literature. The decomposition temperature of lanthanum nitrate, however, was found to be lower than reported in literature. It was also observed in this work that the liquefication temperatures of mixed nitrates were lower than the individual nitrates. The individual nitrates maintained their identities and decomposed separately even when they were dissolved and mixed together to form the precursors.

The heating schedules were tailored according to the decomposition chemistry information to achieve the best quality films. Particularly interesting is the novel approach of using a humid atmosphere to eliminate the cracking problem encountered in nitrates derived spinel films. The humid atmosphere decreased the aluminum nitrate decomposition rate to allow the precursor film to accommodate the huge volume change. This is a faster process than simply decreasing the overall heating rate commonly used in MOD films. The surfaces of both spinel and $LaAlO_3$ films were smooth and featureless. The best films had an average surface roughness of < 1 nm for a 25 μm^2 area, compared to < 0.1 nm for commercially available single crystal substrates.

Just as important as the surface features are the crystallographic properties of these films. Both magnesium aluminum isopropoxide and the mixed nitrates produced epitaxial spinel films with similar qualities. $LaAlO_3$ films, likewise, can be deposited from mixed nitrates precursor. Those observations dismiss a common, but never adequately tested, perception that multi-cation oxide films cannot be made from mixed

nitrates because of cationic segregation during pyrolysis. This finding eliminates one of the perceived advantages of using precursors with complicated molecular structure such as double metal alkoxide in which the metal cations are linked together to preserve the stoichiometry. Nitrates precursors have the advantages of simplicity and avoidance of carbon contamination. This will open the door for different multi-cation oxide films from mixed nitrates method.

All of these chemically derived films were epitaxial. Only the desired phase and orientation were formed. The SAD of the films showed that they were similar to single-crystal. There were pores with size range from 5 to 30 nm inside the films. Some of the pores were open to the surface. The pores were somewhat faceted. They were most likely to be formed during crystallization. The low vacancy diffusivities prevented the pores from annihilation.

The precursor films first decomposed into solid amorphous mixture. Lattice-matched substrates reduced the crystallization temperature of spinel and lanthanum aluminate by more than 100 K. The epitaxial films heterogeneously nucleated at the substrate/film interfaces and grew upward to consume the amorphous solid regions. Homogeneous nucleation at higher temperatures led to randomly oriented grains on highly mismatched substrates.

The kinetics of the solid-state thin film heteroepitaxy, especially in multi-cation oxide films, has scarcely been studied by others. It was found in this study that $LaAlO_3$ films were grown not exactly in the layer-by-layer mode as in typically homoepitaxy. The Johnson-Mehl-Avrami exponent was between 1.4 to 1.5. The most likely explanation is that nucleation on the substrate surface proceeded gradually. Regions nucleated earlier could grow three dimensionally. Regions nucleated later were impinged and can only grow upwardly. The growth interface for $LaAlO_3$ was rough due to the low entropy change of crystallization. The activation energy for $LaAlO_3$ growth on $SrTiO_3$ substrate was estimated to be approximately 5.1 eV.

Never before have chemically derived films been used in epitaxial planarization or even as interlayers for epitaxial BYC films. This work is the first to demonstrate the viability of chemically derived films in these applications. High quality MOD BYC films have been deposited on chemically derived $LaAlO_3$ films. The rougher $LaAlO_3$ film surfaces directly led to lower critical current density and higher a-axis grain density in MOD derived BYC films than would be deposited on single-crystal substrates. Nevertheless the BYC films had transition temperatures above 92 K with J_c of approximately 2×10^6 A/cm^2 at 77 K. These electrical properties were adequate for

practical use. These epitaxial films also greatly reduced the nonplanarity of trenched substrates.

In another related issue, the infiltration of BYC into the pores in lanthanum aluminate films provided another piece of indirect evidence that showed partial melting occurs in MOD-BYC films formation.

8.2 FUTURE WORK

This work has demonstrated the potential of chemically derived, especially nitrates precursors, spin-on films to be used in HTSC MCM. There is, nonetheless, more work that can be done.

The general processing conditions have been established to produce epitaxial films with satisfactory properties. The processing conditions have not be optimized. It is established in this work that pyrolysis atmosphere and heating rate can greatly influence the surface features of the films. More studies can be done on the effect of atmosphere or heating rate.

It is important that the porosity can be controlled for industrial applications. It is possible to make a sandwich of dense/porous/dense films that can be an excellent dielectric layer if there is a way to produce dense films for spinel and $LaAlO_3$. The dense parts of the layer prevent any potential shorting of the BYC and provide nice surface for deposition. The middle porous layer reduces the overall dielectric constant of the whole structure. The challenge is to find a processing route that can produce such structure. The surface roughness and planarization are other areas that need to be addressed for industrial application. The deposition of BYC films on them requires improvement in those areas.

One digression from this study is to examine the possibility of making porous spinel films for humidity sensor. Spinel has been investigated for applications in humidity sensors (Shimizu, 1985; Gusmano, 1992). The electrical conductivity of spinel is related to the humidity by two mechanisms: ionic and electrolytic from condensed water (Anderson, 1968; McCafferty, 1971). The ionic conduction mechanism is caused by: water chemisorbs on the oxide surface and form hydroxyl groups. They hop among the hydroxyl groups when they dissociate into H^+. There is an additional conduction mechanism if the material is porous. Water can condense in the pores and provide electrolytic conduction. These porous spinel films can also be used in humidity sensor if the porosity can be controlled.

On a more scientific side, the heterogeneous nucleation from single-crystal substrate reduced the crystallization temperature of both $LaAlO_3$ and spinel significantly. A more quantitative study can be pursued on the amount of temperature reduction as a function of lattice mismatch. This can be done by using other substrate materials such as $NdGaO_3$ to grow films on. The extensive research in substrate materials for BYC superconductor allows more substrate materials available for this study. It is also possible to first grow a seed layer of $LaAlO_3$ followed by deposition of nitrate precursors. The homogeneous nucleation can be monitored by the growth of this new layer through the use of four-circle XRD. The potential difficulty of rapid crystallization can be overcome by reducing the number of nucleation sites by damaging part of the substrate surface.

The kinetics of $LaAlO_3$ crystallization can be studied further. Crystallization rate can be measured in recrystallization of amorphous regions caused by ion bombardment. This will eliminate most of the volume-change effect. Another possible study is to examine only the $LaAlO_3$ homoepitaxy from nitrates-derived films. Here only the volume-change effect will be studied. The nucleation effect is eliminated.

This work is the first work to deposit spinel and perovskite epitaxial thin films directly by nitrate precursors. More investigation hopefully will branch out from this work to further the understanding nitrate precursors for other types of films.

APPENDIX A
LIST OF SUPPLIES

Table A.1

Material	Supplier
aluminum isopropoxide	Chattem Chemicals, Chattanooga, TN
aluminum nitrate	Mallinckrodt, Inc., Paris, KY
barium acetate	Mallinckrodt, Inc., Paris, KY
ceramic tip filter	Millipore, Bedford, MA
copper acetate	Alfa Products, Danvers, MA
Crystalbond	Aremco Products, Inc., Ossining, NY
developer for photoresist (CD-30)	Shipley, Newton, MA
isopropanol	Mallinckrodt, Inc., Paris, KY
lanthanum aluminate single crystal	Applied Technology Enterprises, Irmo, SC
lanthanum nitrate	Alfa Products, Danvers, MA
M-Bond 610	Measurements Group, Inc., Raleigh, NC
magnesium aluminate single crystal	Commercial Crystals, Naples, FL
magnesium metal	Alfa Products, Danvers, MA
magnesium nitrate	Mallinckrodt, Inc., Paris, KY
magnesium oxide single crystal	Commercial Crystals, Naples, FL
mercuric chloride	Fluka-Garantie, Switzerland
methanol	Mallinckrodt, Inc., Paris, KY
photoresist (1813)	Shipley, Newton, MA
silicon wafer	Virgina Semiconductor, Inc., Frederickburg, VA
strontium titanate powder	Transelco, Penn Yan, NY
strontium titanate single crystal	Commercial Crystals, Naples, FL
trifluoroacetic acid	Aldrich, Milwaukee, WI
yttrium acetate	Alfa Products, Danvers, MA
zirconia single crystal	Ceres Corp., North Billerica, MA

APPENDIX B
EQUIPMENT MANUFACTURERS

Table B.1

Equipment	Supplier
Aligner: Suss MJB 3	Karl Suss America Inc., Waterbury, CT
Atomic Force Microscope	Digital Instruments, Inc., Santa Barbara, CA
Diffractometer: Rigaku RU-200/300	Rigaku USA Inc., Danvers, MA
Dimpler: VCR D500i	VCR Group, Inc., South San Francisco, CA
FTIR: Nicolet	IBM, Armonk, NY
Photomask	Dupont Photomasks, Inc., Round Rock, TX
Profilometer: Dektak 8000	Sloan Technology Corp., Santa Barbara, CA
SEM: S-530	Hitachi Instruments, Inc., Danbury, CT
Spectrophotometer: DU 640	Beckman, Fullerton, CA
Spin coater	Headway Research Inc., Garland, TX
TEM: JEOL 200 CX	JEOL USA Inc., Peabody, MA
TGA: TAS 7	Perkin-Elmer, Hartford, CT
TGA/DTA	Netzche, Exton PA
TG/DTA 220/320	Seiko Instruments, USA Inc., Torrence, CA
Tripod polisher	South Bay Technology, San Clemente, CA
Tube furnace: CM 2200	Lindberg/Blue M, Watertown, WI
Wire saw	South Bay Technology, San Clemente, CA

APPENDIX C
INDEX OF REFRACTION AND DENSITY

The refractive indices of the individual and multilayer thin films can be calculated from the transmittance of light measured by spectrophotometry. The optics of multilayer film has been thoroughly examined. The followings are the theories and calculations for the uv-vis spectrophotometry experiments.

Normal incident is reflected, transmitted or absorbed, as illustrated in the following equation.

$$I = T + R + A = 1 \tag{C.1}$$

where I is the incident energy; T is the transmittance; R is the reflectance; and A is the absorption. Normally the index is a complex number formulated as

$$n_i = n_i + ik_i \tag{C.2}$$

where n is the real number part of the refractive index; and k is the extinction coefficient. The most common method to calculate the effect of any one layer is derived from the Maxwell's equations (Weinstein, 1954). The influence of each layer can be formulated as a 2 x 2 matrix.

$$M_j = \begin{bmatrix} \cos\delta_j & \frac{i}{n_j}\sin\delta_j \\ i n_j \sin\delta_j & \cos\delta_j \end{bmatrix} \tag{C.3}$$

$$\delta_j = (2\pi n_j t_j)/\lambda \tag{C.4}$$

where t_j is the thickness of the j th film; and λ is the wavelength. The total effect of the multilayer is represented by a product matrix M

$$M = M_1M_2M_3... = \begin{bmatrix} m_{11} & i\,m_{12} \\ i\,m_{21} & m_{22} \end{bmatrix} \tag{C.5}$$

The transmittance T is

$$T = (n_s/n_o)\,|t|^2 \tag{C.6}$$

$$t = \frac{2n_o}{(X + W) + i(V + Y)} \tag{C.7}$$

$$X = n_o m_{11} + n_o k_s m_{12} \tag{C.8}$$

$$Y = n_o n_s m_{12} \tag{C.9}$$

$$W = n_s m_{22} \tag{C.10}$$

$$V = m_{21} - k_s m_{22} \tag{C.11}$$

The case of two layers is illustrated in Fig. C.1. The refractive indices for air, the first layer, the second layer, and the substrate are n_0, n_1, n_2, and n_s respectively. The extinction coefficient for spinel was assumed to be zero because spinel has very low extinction coefficient (Tropf, 1991). The refractive index of air was assumed to be 1 and the extinction coefficient was also zero. The refractive index for $SrTiO_3$ used was obtained from literature (Gervais, 1991).

This calculated transmittance did not take absorption into account. One method to obtain the absorption value was by measuring the transmittance of a blank substrate. The reflectance can be calculated from the familiar equation

$$R = \frac{(n_o - n_s)^2 + k_s^2}{(n_o + n_s)^2 + k_s^2} \tag{C.12}$$

The fraction of absorption due to the substrate will be

$$A_{frac} = 1 - \frac{T_{meas}}{1 - R} \tag{C.13}$$

The calculated transmittance for the two-layer system first needed to be adjusted by a factor of 1- A_{frac}. This method of adjustment gave a higher transmittance than the actual transmittance of the substrate. The other method was simply to multiply the substrate transmittance with the calculated transmittance to give a better fit.

The n_1, n_2, t_1, and t_2 were varied to make the adjusted transmittance for λ from 400 nm to 1050 nm matches with the measured spectra. The first criterion for the best match was the position of the maxima and minina of the spectra (including the constructive/destructive interference). The second criterion was the sum of the squares of the difference between the simulated and the actual spectra. The packing density p was calculated from a formula derived from the Lorentz-Lorenz equation which treated the pores and the solid as a mixture (Harris, 1979).

$$n^2 = \frac{(1 - p)(n_s^2 + 2)(n_v^2) + p(n_v^2 + 2)n_s^2}{(1 - p)(n_s^2 + 2) + p(n_v^2 + 2)} \tag{C.14}$$

where n_s and n_v are the indices for the solid and the void, respectively. The voids were assumed to filled with only air, and thus n_v is equal to 1.

One source of error was to the thicknesses assumed. Both films were assumed to have the same thickness. Any variation of thickness of either film could change the calculated spectra. The other source of error was from the substrate. The absorption of the substrate changed from sample to sample and changed after each firing.

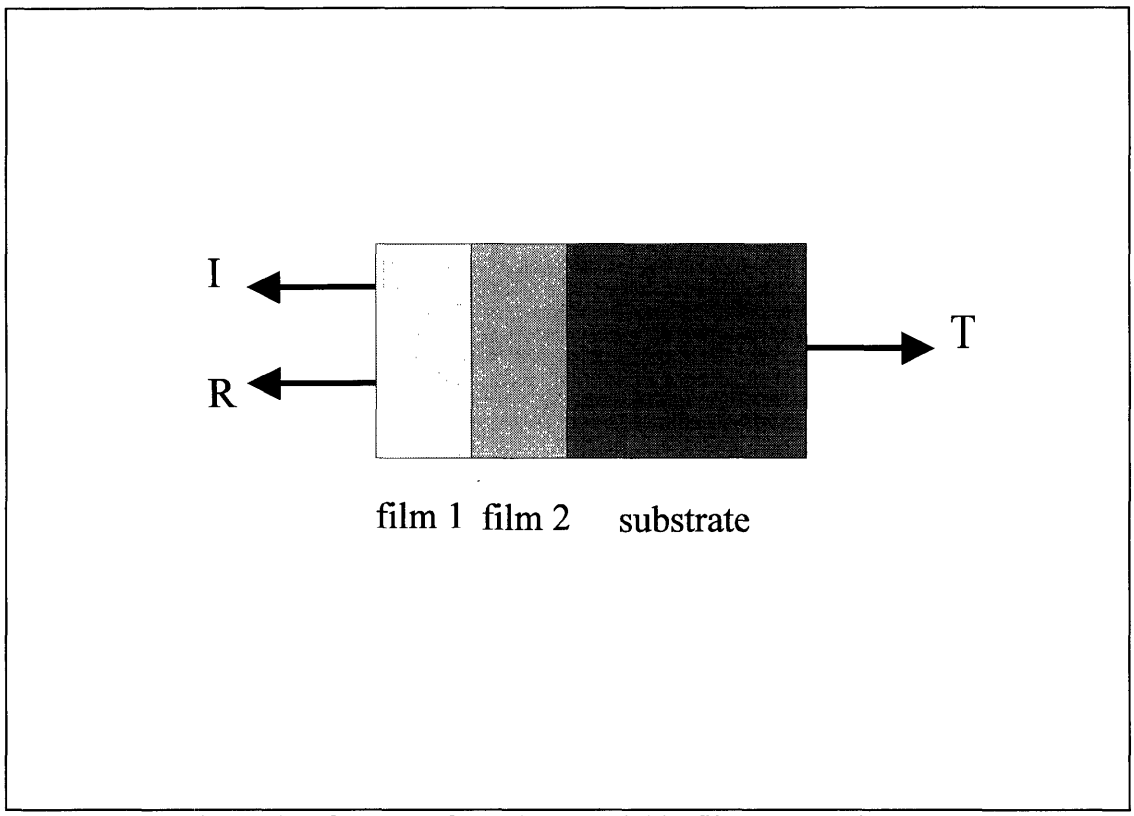

Figure C.1 Schematic of optics of two layers of thin films on a substrate.

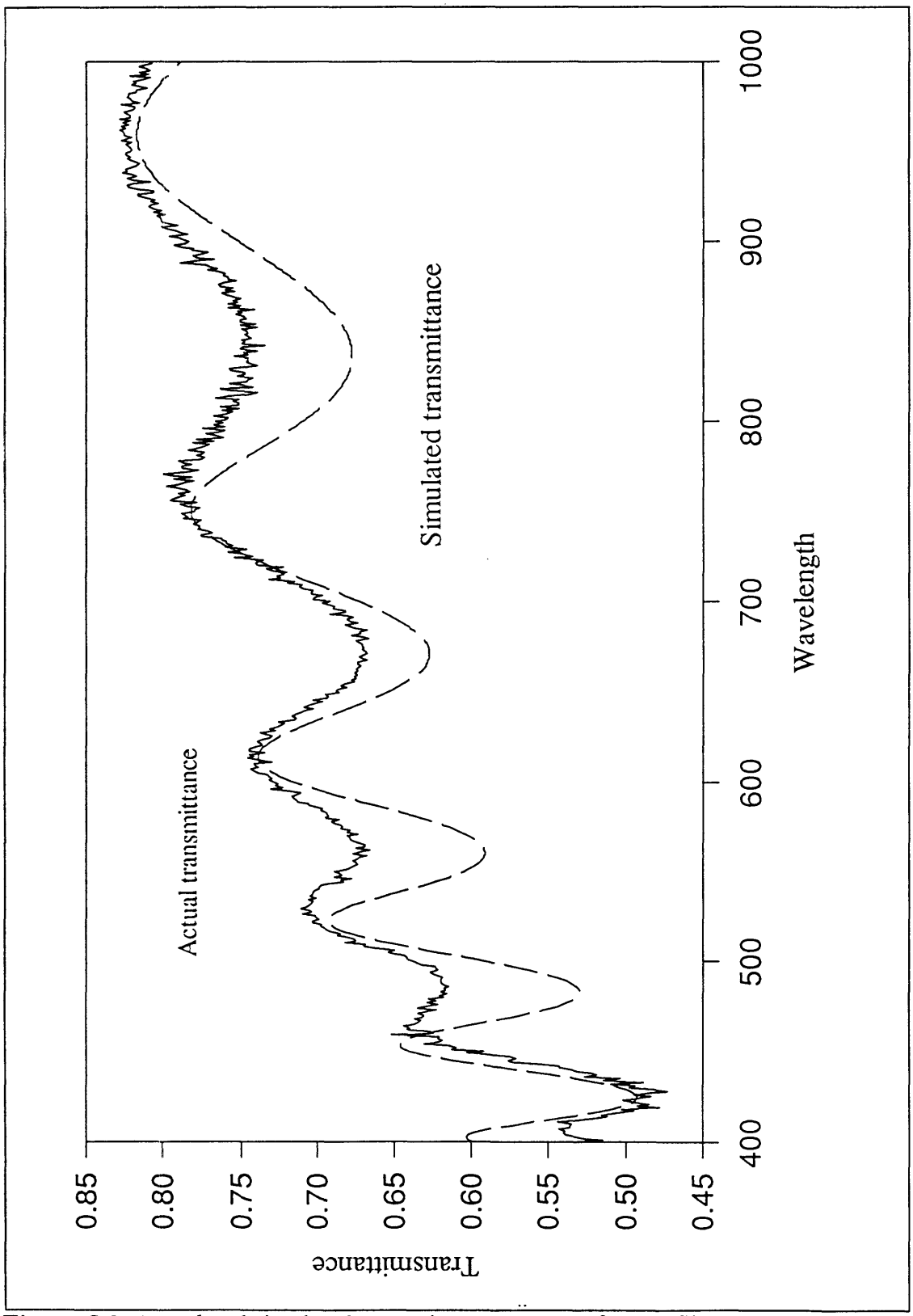

Figure C.2 Actual and simulated transmittance spectra of a two-films system.

BIBLIOGRAPHY

A Allen, P.B.; Fisk, Z.; and Migliori, A. (1989)
"Normal State Transport and Elastic Properties of High T_c Materials and Related Compounds"
Physical Properties of High Temperature Superconductors I, World Scientific Publishing Co., Singapore, 213-264.

Anderson, J.H.; and Parks, G.A. (1968)
"The Electrical Conductivity of Silica Gel in the Presence of Adsorbed Water"
J. Phys. Chem., **72** 3662-3668.

Ando, K.; and Oishi, Y. (1974)
"Self-Diffusion Coefficients of Oxygen Ion in Single Crystals of $MgO{\cdot}n\ Al_2O_3$ Spinels"
J. Chem. Phys., **61** [2] 625-629.

Avrami, M. (1939)
"Kinetics of Phase Change. I"
J. Chem. Phys., **7** 1103-1112.

B Bader, H.P.; and Lardon, M.A. (1985)
"Planarization by Radio-Frequency Bias Sputtering of Aluminum as Studied Experimentally and by Computer Simulation"
J. Vac. Sci. Technol. A, **3** [6] 2167-2171.

Berkowski, M.; Pajaczkowska, A.; Gierlowski, P.; Lewandowski, S.J.; Sobolewski, R.; Gorshunov, B.P.; Kozlov, G.V.; Lyudmirsky, D.B.; Sirotinsky, O.I.; Saltykov, P.A.; Soltner, H.; Poppe, U.; Bucha, Ch.; and Lubig, A. (1990)
"$CaNdAlO_4$ Perovskite Substrate for Microwave and Far-Infrared Applications of Epitaxial High T_c Superconducting Thin Films"
Appl. Phys. Lett., **57** [6] 632-634.

Berkstresser, G.W.; Valentino, A.J.; and Brandle, C.D. (1991)
"Growth of Single Crystals of Lanthanum Aluminate"
J. Crystal Growth, **109** 467-471.

Blanchet, G.B.; and Fincher, C.R. Jr. (1991)
"High Temperature Deposition of HTSC Thin Films by Spray Pyrolysis"
Supercond. Sci. Tech., **4** 69-72.

Braunstein, G.; Paz-Pujalt, G.R.; Mason, M.G.; Blanton, T.N.; Barnes, C.L.; and Margevich, D. (1994a)
"The Processes of Formation and Epitaxial Alignment of $SrTiO_3$ Thin Films Prepared by Metallo-Organic Decomposition"
J. Appl. Phys., **73** [2] 961-970.

Braunstein, G.; Paz-Pujalt, G.R.; and Blanton, T.N. (1994b)
"Epitaxial Alignment and Microstructural Development in Lithium Niobate Thin Films Prepared by Metallo-Organic Decomposition"
Mater. Res. Soc. Symp. Proc., **317** 571-576.

Bruinsma, R.; and Zangwill, A. (1987)
"Morphological Transitions in Solid Epitaxial Overlayers"
Europhys. Lett., **4** [6] 729-735.

C Cahn, J.W. (1960)
"Theory of Crystal Growth and Interface Motion in Crystalline Materials"
Acta Metall., **8** 554-562.

Cahn, J.W. (1966)
"On the Morphological Stability of Growing Crystals"
Crystal Growth, Supplement to Phys. and Chem. Solids, 681-690.

Chan, S.-W.; Hwang, D.M.; and Nazar, L. (1989)
"Microstructure of $YBa_2Cu_3O_{7-x}$ Thin Films Grown on Single-Crystal $SrTiO_3$"
J. Appl. Phys., **65** [12] 4719-4722.

Chang, B.P. (1994a)
Ceramic Processing Research Laboratory, Massachusetts Institute of Technology, unpublished work.

Chang, B.P.; Sonnenberg, N.; McIntyre P.C.; and Cima, M.J., (1994b)
"Epitaxial Planarization Using Ion Beam Assisted Deposition"
Mat. Res. Soc. Symp. Proc., **341**, 151-156.

Chen, C.; Ryder, D.F. Jr.; and Spurgeon, W.A. (1989)
"Synthesis and Microstructure of Highly Oriented Lead Titanate Thin Films Prepared by a Sol-Gel Method"
J. Am. Ceram. Soc., **72** [8] 1495-1498.

CRC Handbook of Chemistry and Physics, 56th edition (1975-1976)
CRC Press, Cleveland, Ohio, B149, B191.

Cullity, B.D. (1978)
Elements of X-Ray Diffraction
Addison-Wesley Publishing Company, Reading, MA, 293.

D Dimos, D.; Chaudhari, P.; Mannhart, J.; and LeGoues, F.K. (1988)
"Orientation Dependence of Grain-Boundary Critical Currents in $YBa_2Cu_3O_{7-\delta}$ Bicrystals"
Phys. Rev. Lett., **61** [2] 219-222.

Dinger, T.R.; Worthington, T.K.; Gallagher, W.J.; and Sandstrom, R.L. (1987)
"Direct Observation of Electronic Anisotropy in Single-Crystal $Y_1Ba_2Cu_3O_{7-x}$"
Phys. Rev. Lett., **58** [25] 2687-2690.

E Ekin, J.W.; Braginski, A.I.; Panson, A.J.; Janocko, M.A.; Capone, D.W. II; Zaluzec, N.J.; Flandermeyer, B.; de Lima, O.F.; Hong, M.; Kwo, J.; and Liou, S.H. (1987)
"Evidence for Weak Link and Anisotropy Limitations on the Transport Critical Current in Bulk Polycrystalline $Y_1Ba_2Cu_3O_{7-x}$"
J. Appl. Phys., **62** [12] 4821-4828.

Endo, H.; and Cima, M.J. (1993)
"Preparation and Characterization of Epitaxial $KNbO_3$ Thin Films by a Sol-Gel Method"
Mat. Res. Soc. Symp. Proc., **310** 325-330.

F Fay, H.; and Brandle, C.D. (1966)
"Czochralski Growth and Detwinning of $LaAlO_3$"
Crystal Growth, Supplement to Phys. and Chem. Solids, 51-55.

Funaki, K.; and Shimizu, Y. (1959)
"Thermal Transformations and Rehydration of Amorphous Aluminas Produced by Thermal Decomposition of Aluminum Salts"
Kogyo Kagaku Zasshi, **62** 788-793.

G Galeuchet, Y.D.; and Roentgen, P. (1991)
"Selective Area MOVPE of GaInAs/InP Heterostructures on Masked and Nonplanar (100) and {111} Substrates"
J. Crystal Growth, **107** 147-150.

Geller, S. and Bala, V.B. (1956)
"Crystallographic Studies of Perovskite-like Compounds. II. Rare Earth Aluminates"
Acta Crystal., **9** 1019-1025.

Gervais, F. (1991)
"Strontium Titanate ($SrTiO_3$)"
Handbook of Optical Constants of Solids II
Academic Press, New York, NY.

Ghandhi, S.K. (1983)
VLSI Fabrication Principles
John Wiley & Sons, New York, NY.

Giess, E.A.; Sandstrom, R.H.; Gallagher, W.J.; Gupta, A.; Shinde, S.L.; Cook, R.F.; Cooper, E.I.; O'Sullivan, E.J.M.; Roldan, J.M.; Segmüller, A.; and Angilello, J. (1990)
"Lanthanide Gallate Perovskite-Type Substrates for High-Temperature Superconducting Cuprate Films"
IBM J. of Research and Development, **34** [6] 916-927.

Golden, S.J.; Lange, F.F.; Clarke, D.R.; Chang, L.D.; and Necker, C.T. (1992)
"Metalorganic Deposition of High Critical Current Thin Films in the Bi-Sr-Ca-Cu-O system on {100} $LaAlO_3$ Substrates"
Appl. Phys. Lett., **61** [3] 351-353.

Grimberg, I.; and Weiss, B.Z. (1993)
"The Crystallization Kinetics, Growth Mechanism, and Stability of Co-Evaporated $NiSi_{2\pm0.2}$ Thin Alloy Films"
Appl. Surface Sci., **65/66** 41-48.

Gusmano, G.; Montesperelli, G.; Traversa, E.; Bearzotti, A.; Petrocco, G.; D'Amico, A.; and Di Natale, C. (1992)
"Magnesium Aluminum Spinel Thin Film as a Humidity Sensor"
Sensors and Actuators B, **7** 460-463.

Gusmano, G.; Montesperelli, G.; and E. Traversa, (1993)
"Microstructure and Electrical Properties of $MgAl_2O_4$ Thin Films for Humidity Sensing"
J. Am. Cer. Soc., **76** [3] 743-750.

H Harris, M.; MacLeod, H.A.; Ogura, S.; Pelletier, I.; and Vidal, B. (1979)
"The Relationship Between Optical Inhomogeneity and Film Structure"
Thin Solid Films, **57** 173-178.

Hesse, D.; and Bethge, H. (1983)
"Solid State Reactions for the Epitaxial Growth of Spinel Films"
J. Crystal Growth, **65** 69-76.

Hong, Q.Z.; Zhu, J.G.; Mayer, J.W.; Xia, W.; and Lau, S.S. (1992)
"Solid Phase Epitaxy of Stressed and Stress-Relaxed Ge-Si Alloys"
J. Appl. Phys., **71** [4] 1768-1773.

Hu, M.S.; Thouless, M.D.; and Evans, A.G. (1988)
"The Decohesion of Thin Films from Brittle Substrates"
Acta Metall., **36** [5] 1301-1307.

Hwang, D.M.; Venkatesan, T.; Chang, C.C.; Nazar, L.; Wu, X.D.; Inam, A.; and Hegde, M.S. (1989)
"Microstructure of *in situ* Epitaxially Grown Superconducting Y-Ba-Cu-O Thin Films"
Appl. Phys. Lett., **54** [17] 1702-1704.

J Jackson, K.A. (1967)
"Current Concepts in Crystal Growth from the Melt"
Progress in Solid State Chemistry, **4** 53-80.

Jergel, M.; Chromik, S.; Strbik, V.; Smatko, V.; Hanic, F.; Plesch, G.; Buchta, S.; and Valtynlova, S. (1992)
"Thin YBCO Films Prepared by Low-Temperature Spray Pyrolysis"
Supercond. Sci. Tech., **5** 225-230.

Johnson, W.A.; and Mehl, R.F. (1939)
"Reaction Kinetics in Processes of Nucleation and Growth"
Trans. AIME, **135** 416-459.

K Kazakos, A.M.; Komarneni, S.; and Roy, R. (1990)
"Sol-Gel Processing of Cordierite: Effect of Seeding and Optimization of Heat Treatment"
J. Mater. Res., **5** [5] 1095-1103.

Kingsley, J.J.; and Patil, K.C. (1988)
"A Novel Combustion Process for the Synthesis of Fine Particle α-Alumina and Related Oxide Materials"
Mater. Lett., **6** [11-12] 427-432.

Koren, G.; Gupta, A.; and Basemen, R.J. (1989)
"Role of Atomic Oxygen in the Low-Temperature Growth of $YBa_2Cu_3O_{7-\delta}$ Thin Films by Laser Ablation Deposition"
Appl. Phys. Lett., **54** [19] 1920-1922.

Kroger, H.; Hilbert, C.; Ghoshal, U.; Gibson, D.; and Smith, L. (1989)
"Applications of Superconductivity to Packaging"
IEEE Circuits and Devices Magazine, **May**, 16-21.

Kromann, R.; Bilde-Søresnsen, J.B.; de Veus, R.; Andersen, N.H.; Vase, P.; and Freltoft, T. (1992)
"Relation Between Critical Current Densities and Epitaxy of $YBa_2Cu_3O_{7-x}$ Thin Films on MgO(100) and $SrTiO_3$(100)"
J. Appl. Phys., **71** [7] 3419-3426.

Kumagai, M.; and Messing, G.L. (1985)
"Controlled Transformation and Sintering of a Boehmite Sol-Gel by α-Alumina Seeding"
J. Am. Cer. Soc., **68** [9] 500-505.

Kwok, C.K.; and Desu, S.B. (1993)
"Low Temperature Perovskite Formation of Lead Zirconate Titanate Thin Films by a Seeding Process"
J. Mater. Res., **8** [2] 339-344.

L Lee, A.E.; Platt, C.E.; Burch, J.F.; Simon, R.W.; Goral, J.P.; and al-Jassim, M.M. (1990)
"Epitaxially Grown Sputtered $LaAlO_3$ Films"
Appl. Phys. Lett., **57** [19] 2019-2021.

Lee, C.; Haynes, T.E.; and Jones, K.S. (1993)
"Kinetics of Solid Phase Epitaxial Regrowth in Amorphized $Si_{0.88}Ge_{0.12}$ Measured by Time-Resolved Reflectivity"
Appl. Phys. Lett., **62** [5] 501-503.

Lux, B.C.; Clark, R.D.; Salazar, A.; Sveum, L.K.; and Krebs, M.A. (1993)
"Aerosol Generation of Lanthanum Aluminate"
J. Am. Cer. Soc., **76** [10] 2669-2672.

M Manesse, J.V.; Hamdi, A.H.; Sturner, H.W.; Zhang, Z.H.; and Padmanabhan, K.R. (1989)
"Porosity and Microstructure of Thin Films of Al_2O_3 Formed from an Alumina Sol"
J. Electrochem. Soc., **136** [2] 542-545.

Matsubara, S.; Miura, S.; Miyasaka, Y.; and Shohata, N. (1989)
"Preparation of Epitaxial ABO_3 Perovskite-Type Oxide Thin Films on a (100) $MgAl_2O_4$/Si Substrate"
J. Appl. Phys., **66** [12] 5826-5832.

Matthews, J.W. (1979)
"Misfit Dislocations"
Dislocations in Solids
North-Holland Publishing Company, Amsterdam, Netherlands.

Mattogno, G.; Righini, G.; Montesperelli, G.; and Traversa, E. (1994)
"X-ray Photoelectron Spectroscopy Investigation of $MgAl_2O_4$ Thin Films for Humidity Sensors"
J. Mater. Res., **9** (6) 1426-1433.

McArdle, J.L.; Messing, G.L.; Tietz, L.A.; and Carter, C.B. (1989)
"Solid-Phase Epitaxy of Boehmite-Derived α-Alumina on Hematite Seed Crystals"
J. Am. Cer. Soc., **72** [5] 864-867.

McCafferty E.; and Zettlemoyer, A.C. (1971)
"Adsorption of Water Vapour on α-Fe_2O_3"
Discuss. Faraday Soc., **52** 239-263.

McIntyre, P.C.; Cima, M.J.; and Ng, M.F. (1990)
"Metalorganic Deposition of High-J_c $Ba_2YCu_3O_{7-x}$ Thin Films from Trifluoroacetate Precursors onto (100) $SrTiO_3$"
J. Appl. Phys., **68** [8] 4183-4187.

McIntyre, P.C. (1993)
"Heteroepitaxial Growth of Chemically Derived $Ba_2YCu_3O_{7-x}$ Thin Films"
Sc.D. Thesis, Department of Materials Science and Engineering, Massachusetts Institute of Technology.

McMahon, T.J. (1986)
"Synthesis of Cordierite from Alkoxide Precursors"
Ceramics Processing Research Laboratory Report #65, Massachusetts Institute of Technology.

Mehrotra, R.C.; Goel, S.; Goel, A.B.; King, R.B.; and Nainan, K.C. (1978)
"Preparation and Characterization of Some Volatile Double Isopropoxides of Aluminum with Alkaline Earth Metals"
Inorg. Chim. Acta, **29** 131-136.

Messing, G.L.; Zhang, S.-C.; and Jayanthi, G.V. (1993)
"Ceramic Powder Synthesis by Spray Pyrolysis"
J. Am. Ceram. Soc., **76** [11] 2707-2724.

Miller, K.T.; Chan, C.J.; Cain, M.G.; and Lange, F.F. (1993)
"Epitaxial Zirconia Thin Films from Aqueous Precursors"
J. Mater. Res., **8** [1] 169-177.

N Nashimoto, K.; Cima, M.J.; and Rhine, W.E. (1995)
"Microstructure of Sol-Gel Derived Epitaxial $LiNbO_3$ Thin Films Observed by Transmission Electron Microscopy"
to be published in *J. Mater. Res.*

Ng, M.F. (1992)
"Barium Fluoride Coarsening in Oxyfluoride Films"
Ceramics Processing Research Laboratory Report #22, Massachusetts Institute of Technology, pp. 5.1-5.8.

O O'Bryan, H.M.; Gallagher, P.K.; Berkstresser, G.W.; and Brandle, C.D. (1990)
"Thermal Analysis of Rare Earth Gallates and Aluminates"
J. Mater. Res., **5** [1] 183-189.

Olson, G.L.; and Roth, J.A. (1988)
"Kinetics of Solid Phase Crystallization in Amorphous Silicon"
Mat. Sci. Reports, **3** 1-77.

Oza, T.M.; and Mirza, B.V. (1965)
"Thermal Decomposition of Magnesium Nitrate"
Indian J. Chem., **3** 280-281.

P Paine, D.C.; Evans, N.D.; and Stoffel, N.G. (1991)
"A Study of the Effect of Misfit-Induced Strain on the Kinetics of Solid Phase Epitaxy in the $Si_{1-x}Ge_x$ on <001> Si system"
J. Appl. Phys., **70** [8] 4278-4286.

Parker, M.A.; Hylton, T.L.; Coffey, K.R.; and Howard, J.K. (1993)
"Solid Phase Heteroepitaxy of Barium Ferrite on Sapphire"
Mat. Res. Soc. Symp. Proc., **280** 625-628.

Partlow, D.P.; and Greggi, J. (1987)
"Properties and Microstructure of Thin $LiNbO_3$ Films Prepared by a Sol-Gel Process"
J. Mater. Res., **2** [5] 595-605.

Peercy, P.S.; Bauer, E.G.; Dodson, B.W.; Ehrlich, D.J.; Feldman, L.C.; Flynn, C.P.; Geis, M.W.; Harbison, J.P.; Matyi, R.J.; Petroff, P.M.; Phillips, J.M.; Stringfellow, G.B.; and Zangwill, A. (1990)
"Fundamental Issues in Heteroepitaxy—A Department of Energy, Council on Materials Science Panel Report"
J. Mater. Res., **5** [4] 852-894.

Peng, C.H.; and Desu, S.B. (1992)
"Investigation of Structure Development in MOD $Pb(Zr_xTi_{1-x})O_3$ Films by an Optical Method"
Mat. Res. Soc. Symp. Proc., **243** 335-340.

Peshev, P.; and Slavova, V. (1994)
"Preparation of Lanthanum Aluminate Thin Films by a Sol-Gel Procedure Using Alkoxide Precursors"
Mater. Res. Bull., **29** [3] 255-261.

R Ramana, K.V.; Sharma, R.C.; and Gaur, H.C. (1985)
"Volumetric Properties of Molten Hydrated Salts. 6. Mixtures of Aluminum Nitrate Decahydrate with Hydrates of Calcium, Cadmium, Zinc, and Magnesium Nitrates"
J. Chem. Eng. Data, **30** 449-452 (1985).

Ranganathan, S.; and von Heimendahl, M. (1981)
"The Three Activation Energies with Isothermal Transformations: Applications to Metallic Glasses"
J. Mat. Sci., **16** 2401-2404.

Rillings K.W.; and Roberts, J.E. (1974)
"A Thermal Study of the Trifluoroacetates and Pentafluoropropionates of Praseodymium, Samarium and Erbium"
Thermochimica Acta, **10** 285-298.

Roy, R.; Suwa, Y.; and Konarneni, S. (1986)
"Nucleation and Epitaxial Growth in Diphasic (Crystalline + Amorphous) Gels"
Science of Ceramic Chemical Processing, 247-258.
Wiley, New York.

Russell, K.C. (1992)
"Nucleation Theory under Metastable and Dissipative Conditions"
Physica Scripta., **T44** 15-22.

Ryshkewitch, E. (1960)
Oxide Ceramics, Physical Chemistry and Technology
Academic Press, New York.

S Sader, E. (1993)
"Improvement of the Crystallinity of RF-Magnetron-Sputtered $LaAlO_3$ Layers on Silicon (100)"
Supercond. Sci. Technol., **6** [7] 547-548.

Schins, W.J.; Bezemer, J.; Holtrop, H.; and Radelaar, S. (1980)
"Recrystallization of Polycrystalline CVD Grown Silicon"
J. Electrochem. Soc., **27** 1193-1199.

Shapiro, M.J.; More, K.L.; Lackey, W.J.; Hanigofsky, J.A; Hill, D.N.; Carter, W.B.; Barefiled, E.K.; Judson, E.A.; O'Brien, D.F.; Patrick, R.; Chung, Y.S.; and Moss, T.S. (1991)
"Interaction of Chemically Vapor Deposited $YBa_2Cu_3O_x$ with Yttria-Stabilized Zirconia Substrates"
J. Am. Cer. Soc., **74** [8] 2021-2024.

Shimizu, Y.; Arai, H.; and Seiyama, T.; (1985)
"Theoretical Studies on the Impedance-Humidity Characteristics of Ceramics Humidity Sensors"
Sensors and Actuators, **7** 11-22.

Siegal, M.P.; Phillips, J.M.; van Dover, R.B.; Tiefel, T.H.; and Marshall, J.H. (1990)
"Optimization of Annealing Parameters for the Growth of Epitaxial $Ba_2YCu_3O_{7-x}$ Films on $LaAlO_3$ (001)"
J. Appl. Phys., **68** 6353-6360.

Smith, J.A. Jr., (1995)
"Principles and Development of Process Designs for Pyrolyzing $Ba_2YCu_3O_{7-x}$ Precursor Films"
Ph.D. Thesis, Department of Materials Science and Engineering, Massachusetts Institute of Technology, to be submitted.

Sugiura, M.; and Kamigaito, O. (1984)
"Characterization and Formation Process of Spinel ($MgAl_2O_4$) Prepared by Alkoxide ($MgAl_2(i\text{-}OC_3H_7)_8$) Method"
Yogyo Kyokaishi, **92** [11] 605-611.

T Tate, A.; Ohmori, Y.; and Kobayashi, M. (1988)
"MOVPE Growth of AlGaAs on Preferentially Dry Etched Substrates"
J. Crystal Growth, **89** 360-362.

Thompson, C.V. (1990)
"Grain Growth in Thin Films"
Annu. Rev. Mater. Sci., **20** 245-268.

Ting C.H.; and Neureuther, A.R. (1982)
"Applications of Profile Simulation for Thin Film Deposition and Etching Processes"
Solid State Tech., **25** [2] 115-123.

Ting, C.Y.; Vivalda, V.J.; and Schaefer, H.G. (1978)
"Study of Planarized Sputter-Deposited SiO_2"
J. Vac. Sci. Technol., **15** [3] 1105-1112.

Tropf, W.J.; and Thomas, M.E. (1991)
"Magnesium Aluminum Spinel ($MgAl_2O_4$)"
Handbook of Optical Constants of Solids II
Academic Press, New York, NY.

Tsaur B.Y.; and Hung, L.S. (1980)
"Epitaxial Alignment of Polycrystalline Si Films on (100) Si"
Appl. Phys. Lett., **37** [7] 648-651.

Turco, F.S.; Simhony, S.; Kash, K.; Hwang, D.M.; Ravi, T.S.; Kapon, E.; and Tamargo, M.C. (1992)
"Molecular Beam Epitaxial Growth of GaAs/AlAs and GaAs/AlGaAs Quantum Wells on Sub-Micron-Period Corrugated Substrates"
J. Crystal Growth, **104** 766-772.

Tuttle, B.A.; Headley, T.J.; Bunker, B.C.; Schwartz, R.W.; Zender, T.J.; Hernandez, C.L.; Goodnow, D.C.; Tissot, R.J.; Michael, J.; and Carim, A.H. (1992)
"Microstructural Evolution of Pb(Zr, Ti)O_3 Thin Films Prepared by Hybrid Metallo-Organic Decomposition"
J. Mater. Res., **7** [7] 1876-1882.

V Vaidya, K.J.; Yang, C.Y.; DeGraef, M.; and Lange, F.F. (1994)
"Heteroepitaxy of Rare-Earth Hexa-Aluminates on Sapphire"
J. Mater. Res., **9** [2] 410-419.

Vantomme, A.; Nicolet, M.-A.; and Theodore, N.D. (1994)
"Epitaxial $CoSi_2$ Films on Si(100) by Solid-Phase Reaction"
J. Appl. Phys., **75** [8] 3882-3891.

van Veen, A.; Reader, A.H.; Gravesteijn, D.J.; and van Gorkum, A.A. (1993)
"Voids in Epitaxial Silicon Films Grown Under Different Thermal Conditions: Void Detection by Thermal Helium Desorption"
Thin Solid Film, **241** 206-210.

Vilmin, G.; Komarneni, S.; and Roy, R. (1987)
"Crystallization of $ThSiO_4$ from Structurally and/or Compositionally Diphasic Gels"
J. Mater. Res., **2** [4] 489-493.

von Allmen, M.; Lau, S.S.; Mayer, J.W.; and Tseng, W.F. (1979)
"Solid-State Epitaxial Growth of Deposited Si Films"
Appl. Phys. Lett., **35** [3] 280-282.

W Wang, J.; Zhen, K.; Wei, Q.; and Bi, Y. (1992)
"Surface Properties of $LaAlO_3$ Perovskite Oxides and Their Catalytic Activities"
Wuli Huaxue Xuebao, **8** [2] 247-250.

Warner, J.D.; Bhasin, K.B.; and Miranda, F.A. (1990)
"Dependence of the Critical Temperature of Laser-Ablated $YBa_2Cu_3O_{7-\delta}$ Thin Films on $LaAlO_3$ Substrate Growth Technique"
Supercond. Sci. Technol., **3** 437-439.

Weinstein, W. (1954)
"Computations in Thin Film Optics"
Vacuum, **4** [1] 3-19.

Wendlandt, W.W. (1956)
"The Thermolysis of the Rare Earth and Other Metal Nitrates"
Analytica Chimica Acta, **15** 435-439.

Wu, P.; and Pelton, A.D. (1992)
"Coupled Thermodynamic-Phase Diagram Assessment of the Rare Earth Oxide-Aluminum Oxide Binary Systems"
J. Alloys and Compounds, **179** 259-287.

Wu, W.K.; Ashburn, J.R.; Torng, C.J.; Hor, P.H.; Meng, R.L.; Gao, L.; Huang, Z.J.; Wang, Y.Q.;and Chu, C.W. (1987)
"Superconductivity at 93 K in a New Mixed Phase Y-Ba-Cu-O Compound System at Ambient Pressure"
Phys. Rev. Lett., **58** [9] 908-910.

X Xiong, G.C.; and Wang, S.Z. (1989)
"Epitaxial Growth of Superconducting $YBa_2Cu_3O_{7-x}$ Thin Films by Reactive Magnetron Sputtering"
Appl. Phys. Lett., **55** [9] 902-904.

Y Yao, G.-D.; Hou, S.Y.; Dudley, M.; and Phillips, J.M. (1992)
"Synchrotron X-ray Topography Studies of Twin Structures in Lanthanum Aluminate Single Crystals"
J. Mater. Res., **7** [7] 1847-1855.

Z Zhang, J.; Stauf, G.T.; Gardiner, R.; van Buskirk, P.; and Steinbeck, J. (1994) "Single Molecular Precursor Metal-Organic Chemical Vapor Deposition of $MgAl_2O_4$ Thin Films"
J. Mater. Res., **9** [6] 1333-1336.